Development of a Variable Geometry Ejector for a Solar Desalination System

U.PORTO

FEUP **FACULDADE DE ENGENHARIA**
UNIVERSIDADE DO PORTO

Diogo Nunes Couto e Sá

A Thesis in the Field of Energy Management
for the Degree of Master of Science in Mechanical Engineering

Advisor: Dr. João Soares
Co-Advisor: Dr. Szabolcs Varga

June 2019

Abstract

There is a scarcity of fresh-water resources that with the growing of the world's population require sustainable solutions for the use of the planet's water resources. Solar desalination is one of the solutions. Multi-effect Desalination using a Thermo Vapor Compressor (MED-TVC) presents the least energy intensive method of desalination.

MED-TVC have ejectors as key system components, which permit to attain high performance at design conditions. However, using renewable energy sources lead to an extended range of operational conditions. Ejector's efficiency drops significantly when operating at off-design conditions. A solution is to use a variable geometry ejector, i.e. geometry adapts to operation conditions.

Research was performed to optimize the ejector entrainment ratio for various motive flow temperature conditions.

Apart from the having the movable Nozzle eXit Position (NXP) implemented on the first geometry, an ejector geometry with bigger constant area section length and other with half of the diffuser angle were created employing the movable NXP.

FLUENT, commercially available Computational Fluid Dynamics (CFD) software, was used to model every ejector geometry for each proposed motive flow temperature. A conventional finite-volume scheme, using steady-state flow and axis-symmetric conditions, was used to solve two-dimensional transport equations with the realizable k-ε turbulence model. A CFD model was successfully developed for steam ejector design and performance analysis.

The objective of the study was to investigate the optimal NXP for every simulated geometry and that way finding the optimum entrainment ratio (i.e. ejector performance). This study also assessed how changing the ejector's geometry would influence the entrainment ratio as well as the optimum position of the NXP.

The results from the study indicate that the variable geometry ejector efficiency improves compared to a conventional jet-ejector design. However, the improvement is not significant when compared to a compromise NXP position that can be found with statistical calculations. It was found that for a NXP 25 millimeters upstream of its original position, the entrainment ratio values did not differ more than 1.63% from the best entrainment ratio values for each temperature. Moreover, 120ºC motive flow was the temperature with the best entrainment ratio (170.1%).

Resumo

Existe uma crescente escassez global de água doce, o que associado ao crescimento da população mundial requere novas soluções sustentáveis para o uso do recurso aquífero do planeta. A dessalinização com recurso a energia solar é uma das soluções possíveis.

Ejetores permitem atingir uma performance elevada nas condições para que foi projetado. Contudo, as fontes renováveis de energia apresentam um caracter intermitente o que leva a uma gama de condições operacionais alargada. A eficiência dos ejetores decresce significativamente quando operam em condições fora das condições de projeto. Uma solução é o uso de um ejetor de estrutura variável, i.e. a geometria do ejetor adapta-se às condições de operação.

Foi realizado um estudo para a otimização do *entrainment ratio* de um ejetor para várias temperaturas de entrada do fluido primário. Para além de uma primeira geometria original de um ejetor, foram criadas mais duas geometrias, uma com o comprimento da secção de área constante maior e outra com metade do angulo do difusor. Em todas as geometrias foi implementado um NXP móvel.

FLUENT, um software de licença comercial para simulação de dinâmica dos fluidos computacional (CFD), foi utilizado para modelar todas as geometrias de ejetores sob todas as condições de temperatura propostas. Foi usado um esquema de volumes finitos, em estado estacionário e axi-simétrico para resolver as equações de transporte com um modelo de turbulência *realizable k-ε*. Um modelo CFD foi desenvolvido com sucesso para o design e análise da performance de ejetores.

O objetivo deste estudo foi investigar a posição ótima do NXP para cada geometria e temperatura simulada de forma a descobrir o melhor *entrainment ratio*. Outro objetivo passou por estudar de que maneira a mudança de geometria do ejetor afeta o *entrainment ratio* bem como na posição ótima do NXP.

Os resultados deste trabalho provam que ter um ejetor de geometria variável aumenta a eficiência do mesmo quando comparado com um ejetor de geometria fixa. Este aumento de eficiência, não é porém, significativo quando comparado com uma posição compromisso do NXP que pode ser calculada com meios estatísticos. Para um NXP 25 milímetros a montante da sua posição original, o valor de *entrainment ratio* não diferiu mais do que 1,63% do melhor valor para cada temperatura. Um fluxo principal de 120ºC foi o que obteve melhores resultados de *entrainment ratio* (170,1%).

Acknowledgements

I would first like to thank my family for providing me with unfailing support and continuous incitement over my student years to overcome myself and to do not leave any goal to be unfulfilled. This is the culmination of the best education I could have asked for. This accomplishment would not have been possible without them.

I would also express my deepest gratitude to my thesis coordinators, Dr. João Soares and Dr. Szabolcs Varga. The doors to their offices were always open whenever I needed. They allowed this thesis to be my own work, but steered me in the right direction at every crucial phase or whenever they saw the need to. Working with them was a great experience, without their knowledge I am sure I would not have done this work with the same confidence and most importantly I would definitely not had learn so much as I did this semester.

I would also like to thank the CIENER's investigators who helped in innumerous stages of this research project: Behzad, Hugo and Vu. Without their participation and knowledge, the number of simulations on this work would have been reduced significantly.

Finally, I must express my very profound gratitude to the amazing group of friends I have in FEUP for such fun times and continuous support throughout our university years. We were all at the same boat and are finally reaching the beach.

To you all, thank you.
Diogo.

Table of Contents

List of Figures

List of Tables

Nomenclature

Acronyms (sorted alphabetically)

AR	Area Ratio
BC	Boundary Condition
CAM	Constant Area Mixing
CFD	Computational Fluid Dynamics
CM	Cuthill–McKee
COP	Coefficient of performance
CPM	Constant Pressure Mixing
DNS	Direct Numerical Simulation
EDR	Electrodialysis Reversal Desalination
ER	Entrainment Ratio
GWI	Global Water Intelligence
IPCC	Intergovernmental Panel on Climate Change
LES	Large Eddy Simulation
MED	Multi effect evaporation desalination
MED-TVC	Multi-effect Desalination using a Thermo Vapour Compressor
MENA	Middle East and North Africa
MFR	Mass Flow Rate
MSF	Multistage Flash
NXP	Nozzle Exit Position
OECD	Organization for Economic Co-operation and Development
RANS	Reynolds Averaged Navier-Stokes
RCM	Reverse Cuthill–McKee
RE	Renewable Energy
RO	Reverse Osmosis
RSM	Reynolds Stress Model
TVC	Thermal Vapor-Compression
VGE	Variable Geometry Ejector

Greek letters (sorted alphabetically)

∇	Divergence
δ	Kronecker delta
ε	Rate of dissipation of turbulence energy
μ	Dynamic viscosity
ρ	Fluid Density
τ	Viscous stress
Ω	Specific dissipation rate

Parameters (sorted alphabetically)

D	Diameter
div	Divergence
F	Mass force per volume unit
h	Total energy
k	Turbulent kinetic energy
L	
P	Pressure
R	Reynolds stress tensor
Re	Reynolds Number
S	Strain rate tensor
t	Time
v	Flow velocity vector
x	Flow Position vector

Subscripts (sorted alphabetically)

i	x
j	y
t	Time

Superscripts

$(\grave{\ })$	Fluctuation value
$\overline{(\ )}$	Time-averaged value

1. Introduction

1.1 - World Paradigm

Water plays a vital role in every ecosystem of planet Earth being a fundamental necessity for human lives and livelihoods. Water is needed to drink, to grow food on, to keep environments clean and even to keep populations warm or cold, civilizations that harnessed water thrived and those who didn't fell.

There is no doubt that water is a key resource of planet Earth, yet populations are not managing this resource well or even making the most of it. In a society where, since birth, people are used to naturally flows water every time a tap is opened anytime that they want, as much as they want, is easy to underestimate the effects of inadequate water management can play out over a lifetime.

At this day, half of the world's population live in areas where demand for water resources surpasses the supplies of sustainable water sources [1]. About 71% of the Earth's surface is covered in water, but if all the water could be concentrated into a big sphere, it would be around 1385 km in diameter, nine times shorter than Earth diameter. From the 1.2 trillion cubic meters of water on Earth, 97% of it is salt water and 2% is frozen in the poles or deep in the ground, unavailable to humans [2]. Also, the main aspect of the world's freshwater resources is that is very unevenly distributed.

The domestic water use (drinking, cooking, bathing and cleaning) however plays only a small part of the total of water that is consumed. The industry uses twice as much water as households specially for cooling and water is needed to produce food and crops irrigating the fields uses nearly 70% of the total withdrawn for human uses [1].

WRI's Aqueduct Water Stress Projections based on the latest data from the Intergovernmental Panel on Climate Change (IPCC) 5th Assessment Report (AR5) provide estimates of water stress, demand, supply, and seasonal variability for the years 2020, 2030, and 2040. This study shows that in 2040 most of the world will not have enough water to meet demand during all year as shown as in Figure 1.1.
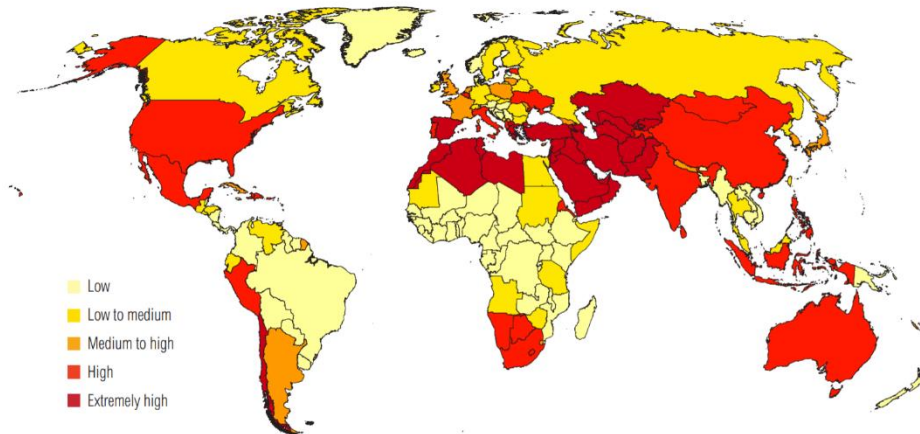
Figure 1.1 - Projected increase in global water stress by 2040 [3].

Day Zero marks the day when a certain city's taps would not flow more water because its reservoirs would become dangerously low on water. Numerous cities worldwide have experienced water supply crises in recent years. Cities like Barcelona, Melbourne, São Paulo and Beijing are among them [3].

The most extreme case, yet, was in Cape Town were due to climatic causes, high urban population growth and deficient water supply systems led to the verge of a Day Zero that was only avoided thanks to water rationing and a rainy season. Cape Town has since taken measures to avoid a Day Zero in 2019 and afterwards, the city has increased the water management programmes and created restrictions on the water consumption per person [4].

This examples and measures should be taken seriously by other cities and countries, indeed, much water could be saved with real shifts toward low water-wasting types of management.

Sustainable water management should also be considered and manage the separation of water supplies for drinking water, other purposes for domestic use and agricultural use water. In addition, rainwater harvesting, separate collection of wastewater streams, and recycling of water offer better planning options for the future.

As seen in Figure 1.2, in recent years, an important balance of water use and fresh water resources per capita has been broken. The water necessities will continue growing as the world population follows the same path.
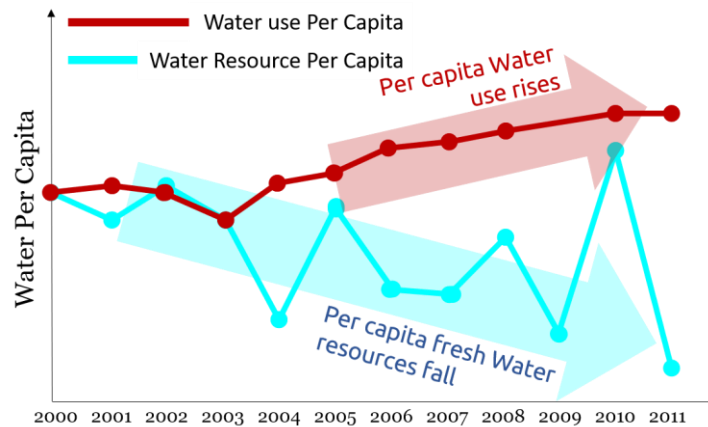
Figure 1.2 – Water use and water resources per capita trends over the years.

The only nearly inexhaustible source of water is in the oceans. Yet, high salinity water is not safe for drinking neither for agricultural purposes. Desalination tackles this drawback giving the world population infinite amounts of freshwater, however, it is an energy-intensive process, and thus it comes at a high cost [5, 6]. For example, even the most straightforward desalination technique (single stage evaporation) requires about 650 (kW.ht)/ m³. Desalination energy consumption represents about 30% to 50% of the cost of water produced [7] and is the most energy-intensive fresh water process (see Figure 1.3).
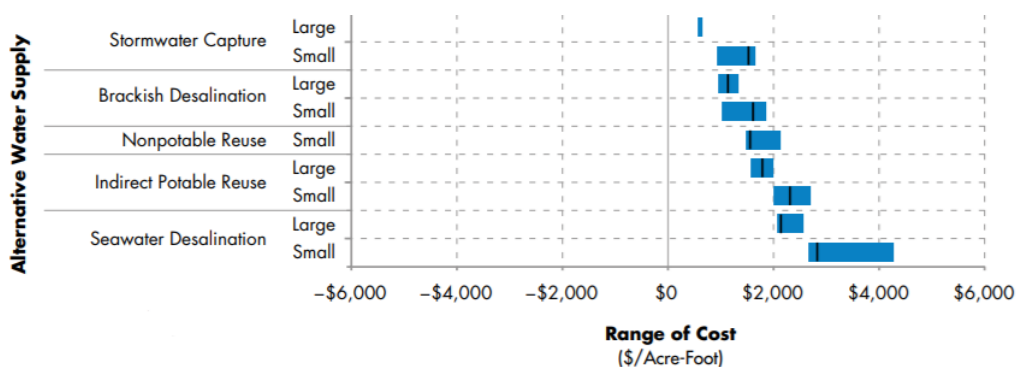
Figure 1.3 - Cost of different methods of alternative water supply [8].

In 2013 the global installed capacity of desalination freshwater was already 80 million m³ of fresh water a day [9] and in 2017 nearly 93 million m³ a day by around 18,500 desalination plants [10].

Desalination plants in the Middle East and North Africa (MENA) region produce 48% of the world's desalinated water [11]. These countries rely on desalination water almost as the only freshwater source. Saudi Arabia alone produces more than 5 million cubic meters of desalinated water per day, making it nearly 50% of the country's water supply.

MENA region have had abundance of energy resources over the years, relying mainly on oil to meet its energy necessities, however, the region has ranges between 2050 and 2800 kWh/m²/year of direct normal radiation and cloud cover is rare [12].
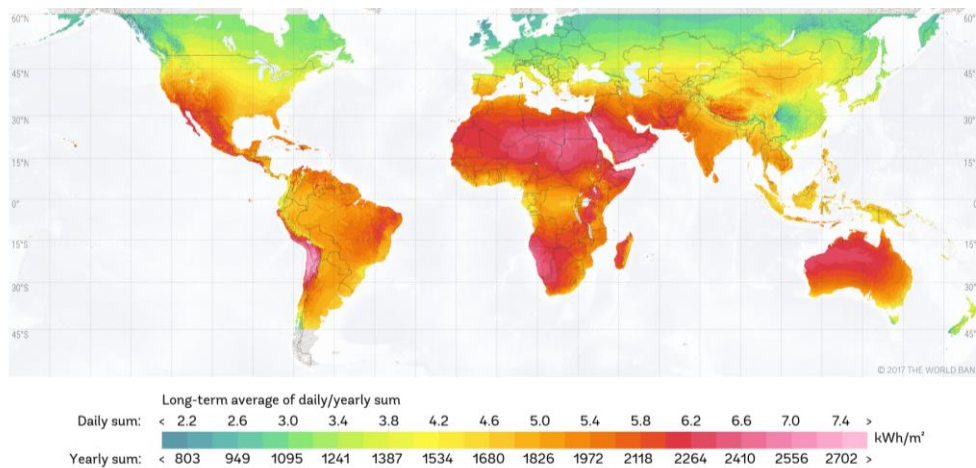
Figure 1.4 - World's annual average direct normal radiation [13].

As technology evolves and the price of crude oil keeps climbing, a shifting towards Renewable Energy (RE) sources is happening in every energy demanding process and desalination is no exception. Solar powered desalination techniques are in vogue in the industry. The technology is mature enough and provides easy installation, operation and maintenance as well as reasonable efficiency. This technology is the ideal technology for water demands less than 50 m³/day [14].

Within two decades, renewable energy sources will be the world's main energy source of power. Wind, solar and other renewables will account for about 30% of the world's electricity supplies by 2040 [15].

The purpose of introducing more and more renewable energy into the energy system was to save fuel, with time and studies, companies started to realize that a fossil fuel free reality with all the commodities that the 21st century citizen needs was

possible. As the supply of oil and coal decreases, their prices will increase so as the costs of products and services that depend on them. The solution to prevent an energy crisis would be to increasingly replace and eliminate non-renewable energy source devices and activities for renewable ones.

The CO_2 emissions on the last years showed differences on approach on energy policies. On the one hand, the Organization for Economic Co-operation and Development (OECD) countries (all developed countries) had a decrease of 1.4% on CO_2 emissions and on the other hand the non-OECD countries (such as China, Russia and India) had a 2.7% increase of CO_2 emissions.

For years it was thought that decarbonization and changing the energy sources from oil and gas to renewables was a drawback in economic growth. New studies suggests that not only this is wrong, the shifting to renewable energy sources meant a significant driver in economic growth. In countries like China, Canada, France, Germany, Italy, Kenya, Portugal, Spain and the United Kingdom the renewable energy consumption had a significant positive effect on economic growth in the long-run [16].

It is expected that in current times, 76 million tons of CO_2 is immitted annually due to desalination processes (see Figure 1.5). This number is estimated to rise up to 218 million tons of CO_2 per year by 2040 [17]. With an obvious growth on the number of desalination facilities, solar powered desalination can help minimize the ecological footprint left by them. Therefore, the world concerns regarding fossil fuels dependence and greenhouse-gas emissions lead to shifting towards renewable energy sources and desalination is no exception.
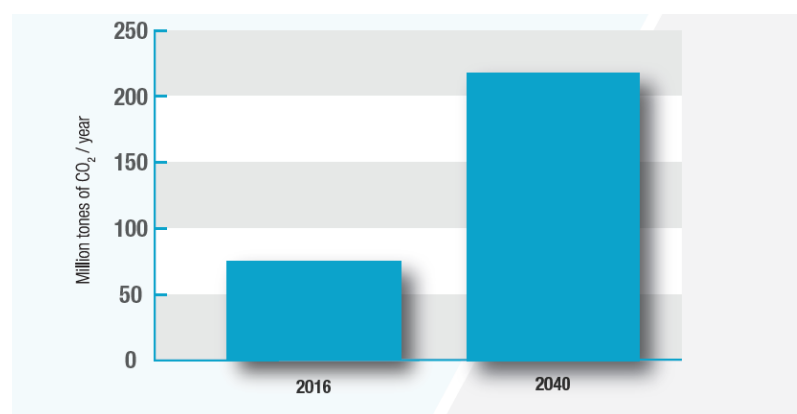
Figure 1.5 – Desalination CO_2 emissions in 2016 and 2040 (predicted).

Seawater desalination installations and market are growing fast (see Figure 1.6). The Global Water Intelligence (GWI) reports that in 2012 [5], the installed global desalination capacity was increasing by 55% a year.

In 2013 the global installed capacity of desalination freshwater was already 80 million m^3 of fresh water a day [9] and in 2017 nearly 93 million m^3 a day by around 18500 desalination plants [10]. The desalination capacity for the next few years is expected to grow 7 to 9% per year worldwide having Asia, the US and Latin America as the main drivers of this growth [9]. The water desalination market is following the same path. It was valued at 13 billion Euros in 2017 and it is expected to grow 7.8% until 2025 [18].
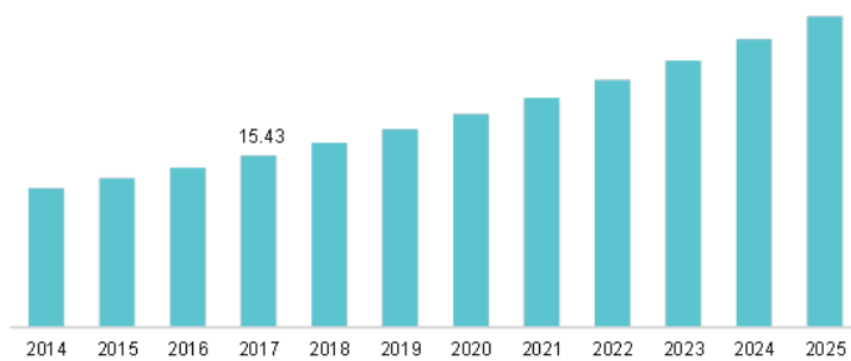
Figure 1.6 - Global Water Desalination Market Size, 2014-2025 (USB Billion) [18].

1.2 - Future Prospects and Objectives in Solar Desalination

There are incredible prospects in developing desalination and RE technologies with an ambitious vision for the future [19]. The long-term use of desalination plants as well as new desalination technologies have resulted in affordable water supply and better energy efficiency [20].

RE desalination costs are still higher than the fossil fuel-powered desalination plants but new studies suggest that the prices are decreasing due to the better process design and better understanding of the technology [21]. The solar energy has the potential to become highly competitive price-wise as it did with other technologies. The use of solar energy for desalination has incredible odds to succeed as a technically practical solution to deal with the water and energy stressing issues.

ProDes took the first step to create an organization to promote renewable energy for water production through desalination with an overall budget of 1,023,594€ in which EU contributed with 75%. Up-to-date there were not any coordination of research nor industrial product development on the European level. It was a project that brought together 14 European organizations to boost the use of RE Desalination with training, workshops, publications and new projects. The creation of "RE Desalination Road Map" defined targets and strategies to enhance the use of RE Desalination technologies where technological, economic and social barriers were tackled.

There is still a strong interest for RE-desalination and taking the ProDes project as an inspiration, other RE-desalination objective-based projects are getting set into practice. Saudi Vision 2030 is a massive project to reduce Saudi Arabia's dependence on oil, diversify the economy and to modernize the country with the help of foreign investment in every sector.

The energy and water resources are one of the most addressed issues. It was acknowledge the renewable energy potential in the MENA region is huge. MENA region has high annual average wind speed and between 22 and 26% of the world's total direct sun normal irradiation strikes the region [22].

RE-desalination can benefit the region ensuring a sustainable water supply, energy security to the sector and environmental sustainability. The MENA region countries have a pivotal role on the renewable energy desalination, the region is responsible for one third of the world's global desalination capacity.

Jordan, Morocco, Saudi Arabia, The United Arab Emirates and Tunisia have ambitious renewable energy goals in addition to good policies and managerial frameworks to help mature the technology reducing costs and increasing efficiency. In fact, the first big steps are already being made, Al Khafji desalination plant in Saudi

Arabia is the world's first solar-powered desalination plant. With an investment of 114 million euros, it can produce up to 60,000 m³ of fresh water per day supplying roughly 150,000 people with safe drinking water [23].
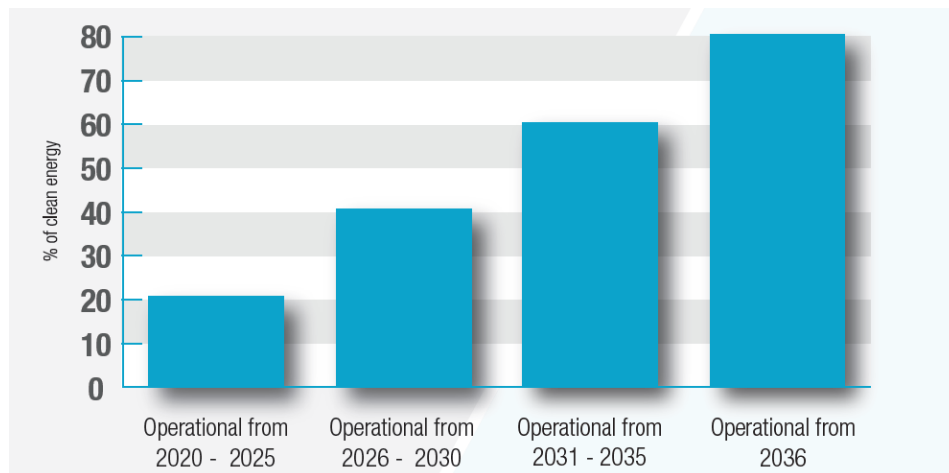
Figure 1.7 – Annual energy to come from clean sources for desalination Plants.

Another challenge is related to the development of small-scale desalination systems, which can be used in a remote location, family residences to small villages, holiday resorts, industrial sites, offshore and marine applications. Research is needed to develop compact, automated and standardized desalination units that can be easily deployable.

As seen in Figure 1.8, small scale desalination installations is still a really small, but with an enormous potential, market ready to be explored.

New studies and roadmaps are being made about the potential of low energy-input, small scale desalination solutions. University of California developed a road-map for small-scale desalination and pointed that choosing the appropriate technology for each specific community is essential for the viability of the project.

The factors are the salinity of available water source, local availability of energy resources such as high wind speeds and total solar irradiance, the capital available, the technical capacity of the population for operation and maintenance and the willingness to take risks with new technologies [24].

Moreover, the study suggested the next steps for the installation of these small-scale desalination solutions being understanding the specific constraints faced by the community involved, using the limitations that will appear can help identify the most suitable technology and pursue help by connecting with relevant technology experts.
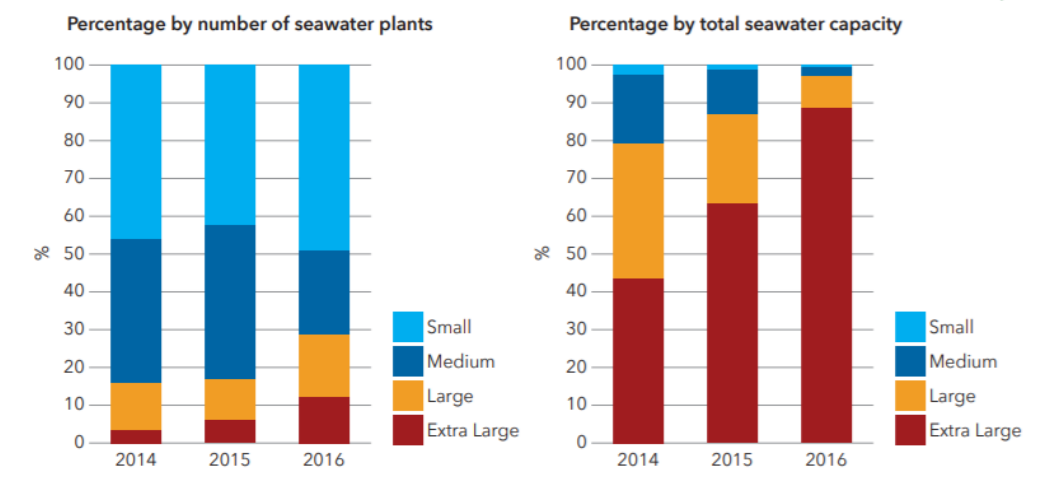
Figure 1.8 – Percentage of different desalination plants sizes.

1.3 - SmallSOLDES Project

SmallSOLDES project, aims to develop a reliable and low-maintenance compact solar-driven desalination unit, using an advanced variable geometry ejector and the corresponding control system. The unit consists in two sub-systems interconnected: (1) The solar thermal collectors that will heat the water until temperatures between 120 and 180ºC to be used in the variable geometry ejector, the first part of the (2) Thermal Vapor-Compression (TVC) system. The TVC system will also have a condenser, an evaporator, pre-treatment units, pumps and storage units for the desalination products. The SmallSOLDES project aims to be a water and desalination sustainability reference for the generations to come.

1.4 - Thesis Objectives

This work is being carried within SmallSOLDES project work plan, and the primary objective is to design a Variable Geometry Ejector (VGE) for a solar-driven desalination system. A Computational Fluid Dynamics (CFD) model will be developed to simulate VGE performance with its geometrical details. The model will be based on the compressible Navier-Stokes equation in axi-symmetric coordinates.

The ejector performance will be assessed for a range of relevant operating conditions and distinct geometries. Additionally, VGE performance will be compared to a fixed geometry ejector.

1.5 - Thesis structure

Chapter I introduced an important contextualization about water-stress, energy and sustainability issues. The theoretical background and some important concepts regarding desalination and ejectors will be introduced in Chapter II. Chapter III will introduce the analytical models needed to study the flow inside an ejector with special emphasis on CFD. This chapter will include the introduction and understanding of some turbulence models as well as the mesh refinement process. Chapter IV consists in the simulations details and results using the CFD software FLUENT. This chapter also includes the introduction of simulation, benchmark, analysis of performance characteristics and flow field details of steam ejectors, and optimization of geometric configurations. Chapter V summarizes present work, address the conclusions and suggest possible direction for future work.

2. Literature Review and Theoretical Background

Understanding the ejector geometry is key to improve renewable desalination.

2.1 - Desalination

The industrial desalination operation consists in separating nearly salt-free fresh water from the sea or brackish water (see Figure 2.1). The resulting salts are isolated in brine water.
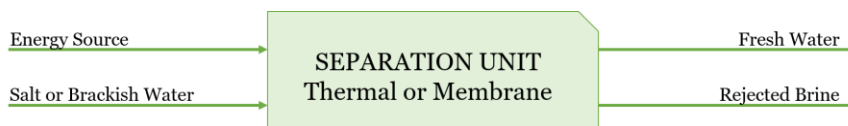
Figure 2.1 - Desalination in a nutshell.

The desalination process can be based on thermal or membrane separation methods. The most important factors affecting the technology choice are the salinity and the temperature of the source water [9].

On the membrane separation processes, Reverse Osmosis (RO) is the most used method. The method consist on moving high pressure brine from one side of membranes to another allowing fresh water to pass through and retain salts, increasing the brine concentration on one side and producing fresh water on the other.

The thermal based separation techniques includes two main categories: (i) Evaporation followed by condensation and (ii) freezing the water followed by melting

the formed water ice crystals. The evaporation followed by condensation method is the most used and it include widely used technologies such as Multistage Flash (MSF), Single effect evaporation and Multi effect evaporation desalination (MED).

Other methods, such as Electrodialysis Reversal Desalination (EDR) uses electricity applied to electrodes to pull naturally occurring dissolved salts through an ion exchange membrane to separate the water from the salts [25].

Table 2.3 summarizes all the advantages and disadvantages of the various commercial desalination methods [22, 26].

2.1.1. – Desalination Energy Consumption

Desalination can, indeed, be the solution for a growing fresh-water scarcity problem. However, the whole process is energy-intensive (see Table 2.1). Desalination consumes more energy per liter than other water supply and treatment options.

Table 2.1 - Energy required to deliver 1m³ of water for human consumption from various water sources [27].

Source	Energy Required (kWh/m³)
Lake or River	0.37
Groundwater	0.48
Wastewater treatment	$0.62 - 0.87$
Wastewater Reuse	$1 - 2.5$
Seawater Desalination	$2.5 - 8.5$

Cost-wise, the energy used in the desalination process represents 5 to 40% of the total operating costs of water and wastewater utilities, depending on the location. This costs will tend to increase, as cities expand further and their water needs increase. Consequently, energy will have direct influence on availability and affordability of water [27].

The energy required for seawater desalination depends on the water temperature and its level of salinity. Most of the energy currently being used to supply most of the energy requirements comes from fossil fuels. However, using fossil fuels represents an unsustainable energy solution that can be replaced by renewable energy sources, specially solar [27].

Due to technological improvements, energy requirements for desalination have declined over the years [28]. Table 2.3 shows the energy values of five desalination techniques that uses renewable energy sources to power the process. It shows that Multi-effect Desalination using a Thermo Vapour Compressor (MED-TVC) is the least energy intensive method of desalination.

2.1.2. – Desalination Economics

Developing trends suggests that thermal desalination and membrane desalination are the most effective methods [21]. In the first few desalination facilities, in the late 1850s, the cost was not important because it was used for military uses producing fresh water for boilers and drinking purposes in ships. When the technology became more widely available for consumers, the costs of fresh water produced became a relevant matter. In 1975 a m^3 of fresh water produced via desalination costed around 1.85€ [29], now it is estimated to cost, on average, 88 cents per m^3 produced [9].

To develop a desalination facility, operational costs, the quality of raw water, incentives or subsidies from governments must be considered to have a good financial study of the project. Different desalination methods have different percentages of cost distribution specially when the processes uses different techniques such as membrane separation and thermal separation (see Figure 2.2)

Components of Total Annual Desalination Costs
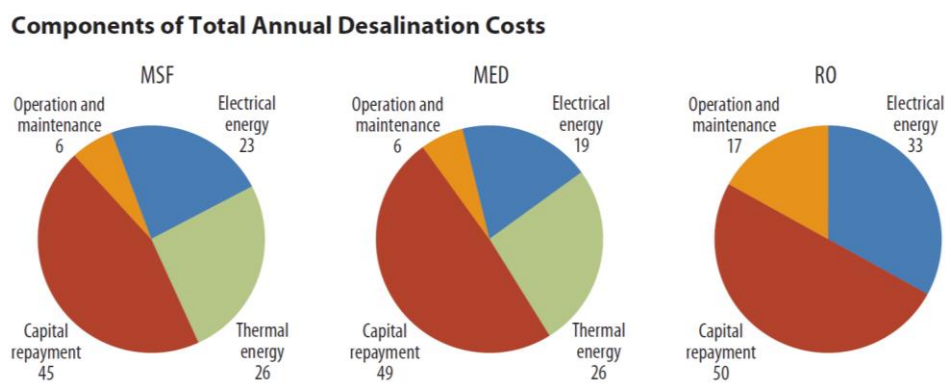
Figure 2.2 – Percentage of cost distribution for three desalination methods [30].

Table 2.2 summarizes the desalination cost of various desalination techniques. It shows that scaling the process can be key to reducing the desalination cost.

The main challenges for renewable energy driven desalination plants are the reduction/financing of initial capital investment for energy generation and the reduction of energy consumption of the desalination process, utilizing more robust energy recovery systems [27].

Table 2.2 - Membrane vs thermal desalination cost per feed water source and production capacity [7].

Feed Water	Plant Desalination (m³/day)	Desalination Cost/m³ (US$)
Seawater RO	Less than 100	1.5–18.75
	250–1000	1.25–3.93
	15,000–60,000	0.48–1.62
	100,000–320,000	0.45–0.66
Brackish water RO	Less than 20	5.63–12.9
	20–1200	0.78–1.33
	40,000–46,000	0.26–0.54
MSF (multi-stage flash)	Less than 100	2.20–8.80
	12,000–55,000	0.84–1.31
	Greater than 91,000	0.46–0.89
MED (multi-effect distillation)	23,000–528,000	0.46–1.54
VCD (vapor compression)	1000–1200	1.77–2.34

Current desalination technologies are sensitive to increase in energy prices. Renewable-energy based desalination can eliminate the cost sensibility to energy prices oscillation in the total desalination cost as well as eliminate the carbon emissions of conventional energy supply from the desalination process [28].

Moreover, with the ever decreasing costs of renewable energy production, the association of renewable energy with desalination will permit the implementation of the latter in further locations, leading to the growth of renewable energy desalination markets.

Table 2.3 - Characteristics of different desalination methods [22, 31-34].

Desalination Technology	MSF	MED (Plain)	MED-TVC	RO	EDR
Energy Source	Thermal	Thermal	Thermal	Mechanical (via Electricity)	Electricity
Typical energy consumption (kWh/ m³)	3-5	1.5-2.5	<1.0	3-5	3-5
Capacity range	Up to 90,000 m³/day	Up to 38,000 m³/day	Up to 68,000 m³/day	Up to 10,000 m³/day	Up to 34,000 m³/day
Typical Salt content in raw water (ppm)	30,000 – 100,000	30,000 – 100,000	30,000 – 100,000	1000 – 45,000	100-3000
Product water quality (ppm)	<10	<10	<10	<500	<500
Current single train capacity (m³/d)	5000 – 60,000	500 – 12,000	100 – 20,000	1 – 10,000	1 – 12,000
Advantages	Easy to manage and operate; Can work with high salinity water	Suitable to combine with RE sources that supply intermittent energy	Broad ranges of pressures; Very low electrical consumption; Can operate at low temperatures (<70ºC)	Easy adjustments to local conditions; Best cost in treating brackish groundwater; Can remove silica	Recovery rate up to 94% and can be combined with RO for higher water recovery (up to 98%); Longer-life membranes (up to 15 years)
Disadvantages	Do not operate bellow 60% capacity; High energy use	Anti-scalents required	Complex configuration	Membrane fouling; Complex configuration	Higher investment associated

2.1.3. – Thermal Desalination

Distillation is used in thermal desalination, meaning the evaporation and condensation of a fluid. The resulting condensed product is fresh water salt free.

Thermal processes proven to be reliable and having the potential for cogeneration of power and water makes it a very interesting solution capable of replacing MSF technology in future projects [5]. This technology can easily be coupled with the available renewable energy such as ocean energy, solar energy, geo thermal energy etc. and waste heat from power plants [35].

Thermal desalination technologies tend to have low energy intensity [22] and be prone to corrosion. The design of new technological tools should take these issues in consideration, optimizing energy consumption and eliminate sources of corrosion to produce higher quality fresh water [36]. A deep knowledge of thermodynamics and heat mass transfer theory is needed for a complete study and improvement in desalination processes.

Thermodynamics sets the minimum energy required to separate water from a salty solution [6].

2.1.3.1 – Multi-effect Distillation

The multi-effect distillation (MED) is the oldest process in desalination, having references and patents in the literature since 1840. Recent developments in the technology have brought MED to the point of competing technically and economically with MSF, the most widely used thermal desalination process [31]. This new trend is not random, MED systems uses nearly half of the MSF electrical energy and the same amount of thermal energy when both processes have the same gain ratio [37].

In a single effect distillation seawater can be boiled releasing steam that at the time it condenses produces pure water. The MED is based on the same principle but with multiple effects connected making the process more efficient employing falling-film evaporative condensers in a serial arrangement, producing fresh water through repetitive steps of evaporation and condensation.

A normal type of multiple effect distillation is made up of a steam supply unit, a certain number of vessels, a series of preheaters, a train of flashing boxes, a condenser and a venting system. Each vessel (effect) is operated at a lower pressure than the effect

before allowing the seawater feed to sustain multiple boiling effects without exchanging additional heat after the first effect [38].

The seawater begins the distillation process entering the first effect, after being preheated in the tubes, seawater is heated to the boiling point either sprayed or otherwise dispersed onto the surface of the evaporator tubes in a thin layer to boost fast boiling and evaporation. The tubes are heated by steam which is condensed on the opposite side of the tube. The condensate from the boiler steam is recycled to the boiler for reuse [34]. Just part of the seawater put into the tubes is evaporated. The remaining water is reused in the next effect where it is again either sprayed or otherwise dispersed onto the surface of the evaporator tubes.

All the tubes are heated by the vapors created in the previous effect. The vapor is condensed to fresh water, while giving up the heat to evaporate a percentage of the remaining seawater feed in the next effect. Additional condensation happens in each effect which guide the feed water from its source to the first effect. This process increases the water temperature before it is evaporated in the first effect [38]. Figure 2.3 breaks down the entire process.
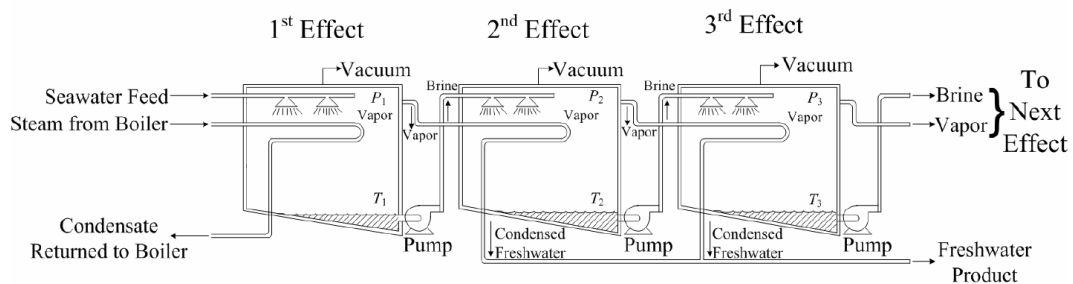
Figure 2.3 - Diagram of a multi-effect distillation plant.

The number of effects is confined by the temperature difference between the seawater inlet temperature at the first effect and the steam temperature at the last condenser [31] and the minimum temperature differential allowed on each effect [37].

There is a very low drop of temperature per effect (1.5 – 2.5 ºC), enabling the incorporation of a large number of effects resulting in a very high gain ration (product to steam flow ratio) lowering the long-term costs of the desalination process.

The performance of MED can be improved by adding thermal or mechanical vapor compression devices [32]. With the reuse of compressed vapor as heating steam, a significantly reduction on the required steam and boiler sized is obtained.

Additionally, a lower amount of energy is used to operate the system, decreasing even further the operational costs.

2.1.3.2 - Thermal Vapor Compression

Vapor-compressed distillation is mainly used for small and medium-scale water desalination units. The technology is known to be compact and efficient [39] and because of its simplicity and absence of moving parts difficulties and malfunctions are unusual even under extreme conditions.

The new component introduced to the MED system is the steam jet ejector, which acts as a thermal compressor. The steam ejector is used to enhance the efficiency of the system. High temperature and high-pressure motive steam coming from external sources such as a boiler or other power plant is introduced into the ejector.

TVC is responsible for the energy recovery in the MED unit, through transferring the energy contained in the high pressure steam to lower pressure vapor, in order to produce a mixed discharge vapor at intermediate pressure [40].

The compressed vapor is entrained into the first effect as the heat source where it condenses and releases its latent heat inside the tubes. Motive steam compresses part of the cycle last effect vapors after coming from the condenser, while the other part returns to its source [41].
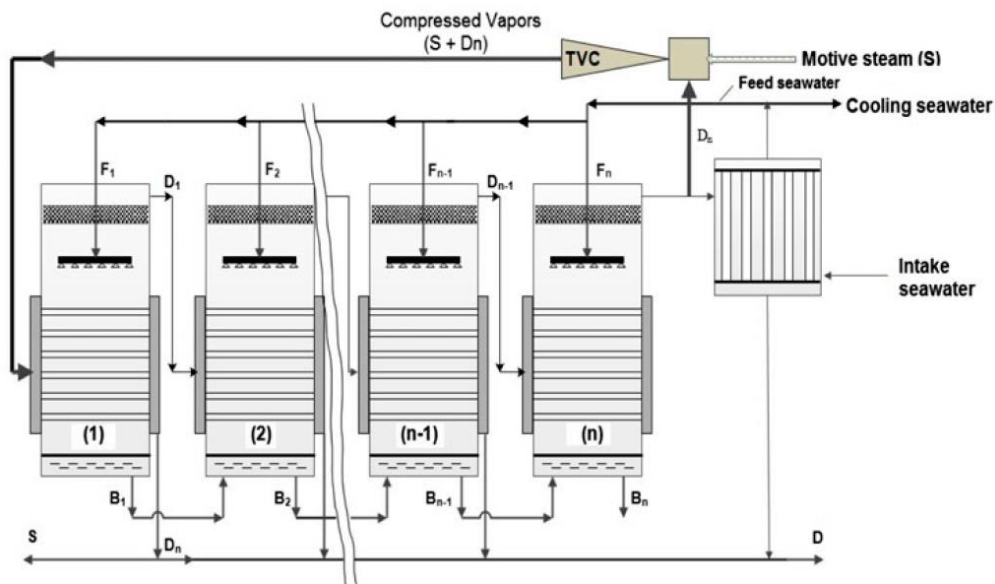
Figure 2.4 - Illustration of MED-TVC system with n effects.

MED-TVC systems have low temperature operation (45-75ºC) [42], hence a better thermal efficiency is obtained making the process one of the most economical seawater desalination processes. It has the ability to use low-cost and low-grade heat.

The new trend in technology development in MED-TVC is using low compression ratios which can reduce the amount of motive steam. This design is compact and provides an approach to increase the unit capacity [41].

Doing a Second Law analysis, the energy quality is determined by its capacity of producing useful work, also known as exergy. Hamed et al. [43] did a study evaluating the performance of TVC and comparing its exergy losses during the process with particular focus on the performance of thermo-compressor. The performance of a TVC system based on exergy analysis was compared in the research against conventional MED systems. Results showed that TVC systems have much better efficiency and lower exergy losses mainly because it reduces the energy consumption required to heat water.

Although TVC systems yield the least exergy destruction among the thermal desalination systems, the most exergy destruction in TVC occurs in the first effect and in the thermo compressor.

Most recently, Alasfour et al. [44] confirmed this fact with exergy analysis simulation models while trying to improve system efficiency. Designing the ejector in optimum conditions is of utmost importance to increase the performance of the whole desalination unit.

2.2 - Ejector

One of the components of a MED-TVC system is the steam ejector, which represents a vital part for the system efficiency. Unlike other compression devices, an ejector can handle two-phase flow, and it is more simple and reliable. An ejector can be used both as a pumping device for incompressible fluids and as a compressor, for compressible fluids. When used as a compressor, a thermal heat source is needed.

An ejector is a mechanism in which a high-velocity jet mixes with a second fluid stream (the entrained flow). The mixture is then discharged with higher pressure than the source of the second fluid. The system operate on the ejector-venturi principle, relying on the momentum of a high-speed steam jet.

A steam ejector is a static device which uses the momentum of a high-speed vapor jet to entrain and accelerate another flow. The thermal compressor is a steam ejector which utilizes the thermal energy to increase the performance by reducing the size of a conventional multi-stage evaporator [45]. The motive fluid can draw large quantities of the secondary fluid because of the lower-pressure at the nozzle exit and high momentum transfer [46]. The nozzle is expected to have a high pressure ratio due to the fact that the poor efficiency of the ejector when operating at low steam pressures [47]. Due to the area reduction and low backpressure, i.e. pressure at the diffuser exit, flow chocking happens at the minimum cross-sectional area where the Mach number is unity [48].

There are different types of ejector designs, being all structurally simple an easy to manufacture, a typical steam-jet air ejector is shown in Figure 2.5. The ejector consists in four parts: (i) primary nozzle, (ii) entrance section, (iii) mixing section and (iv) diffuser.
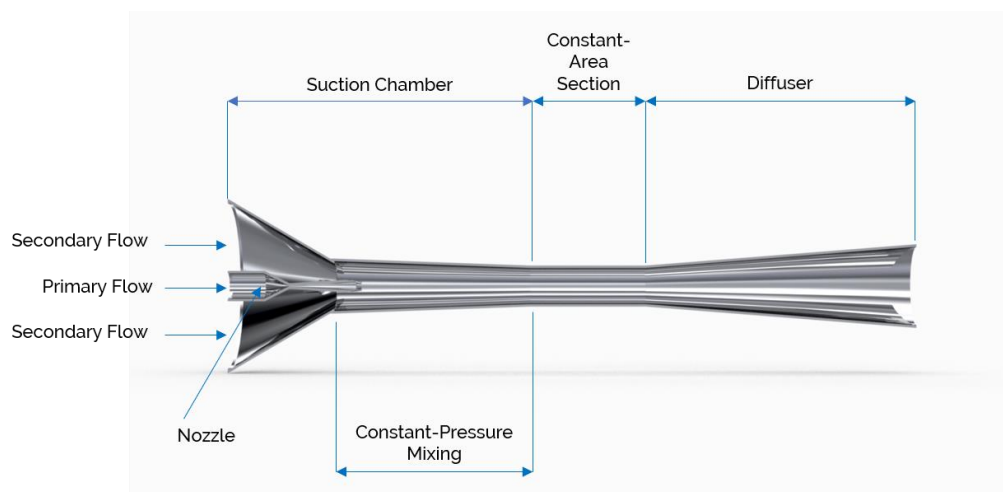
Figure 2.5 - Ejector schematic design.

There are two types of ejector based on how it's mixing is done. In a Constant Area Mixing (CAM) ejector, the primary nozzle discharge is located in the constant area section and in a Constant Pressure Mixing (CPM) ejector, the nozzle exit is placed downstream in the suction chamber.

Thus, the location of the mixture of the motive and secondary streams is different in CAM ejectors and CPM ejectors. In CPM model it is assumed that the mixing of the primary and the secondary streams occurs in a chamber with a uniform, constant pressure while in the CAM model the mixture occurs in the constant area section. The setup of both the CMA and CPM ejector are shown in Figure 2.6.

The constant-pressure mixing design is the most used design of ejectors because it can provide a more stable and it has the ability to perform at a wider range of backpressures [49].
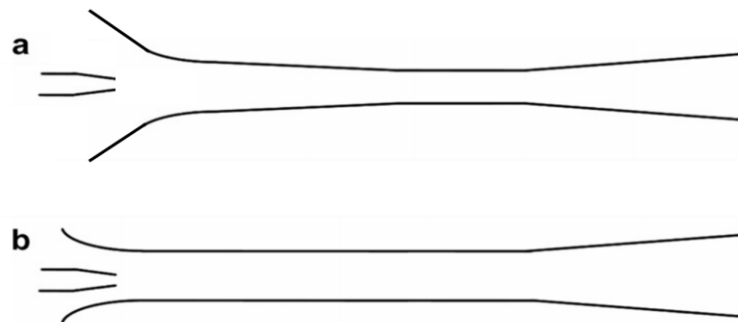
Figure 2.6 - Two typical ejector types: (a) Constant Pressure Mixing ejector and (b) Constant Area Mixing ejector.

2.2.1 – Operational Conditions

Figure 2.7 demonstrates how the velocity and the pressure change when subsonic (Ma<1) or supersonic (Ma>1) flows face a convergent or a divergent area. This concepts are crucial to understand how the flow works in an ejector.
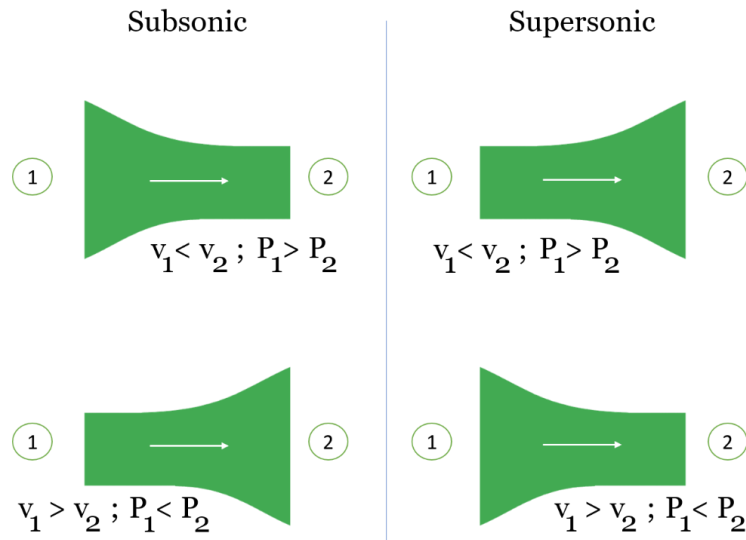
Figure 2.7 – Velocity and Pressure changes when the flow faces a convergent or divergent area in supersonic and subsonic flows.

In the ejector, motive fluid enters a converging diverging nozzle and is accelerated to supersonic conditions. As the flow leaves the nozzle exit section, the supersonic flow creates a low pressure region in the suction chamber which draws the secondary flow to accelerate into the mixing chamber because of the strong shear layer force and increasing the static pressure of the secondary flow (see Figure 2.8 - A). The shear mixing of the two streams begins as the secondary fluid reaches sonic conditions [50]. The stream velocity increases until reaching a supersonic state, where the two fluids are mixed, at the effective area section, then, sudden rise in pressure occurs and flow becomes subsonic again (see Figure 2.8 - B).

The location where the flows are completely mixed, although depending on various operating conditions, should be in the constant area section or in the beginning of the diffuser [51].

As the secondary flow is entrained in the steam, a shockwave is created which leads to subsonic conditions downstream. The mixture then travels through the ejector into a venturi-shaped diffuser. When the steam reaches the diffuser, its kinetic energy is

converted in pressure energy, which helps to discharge the mixture against a backpressure to the evaporator. About 25 to 50% of the total pressure rise occurs in the diffuser [47].

The motive and the secondary fluids flow towards the lowest-pressure spot. There, both fluids mix together violently and quickly [52]. The mixture, later, slows down and the pressure increase before the mixture comes up at the discharge. Figure 2.8 shows how velocity and pressure vary for the motive and suction fluids through the ejector.
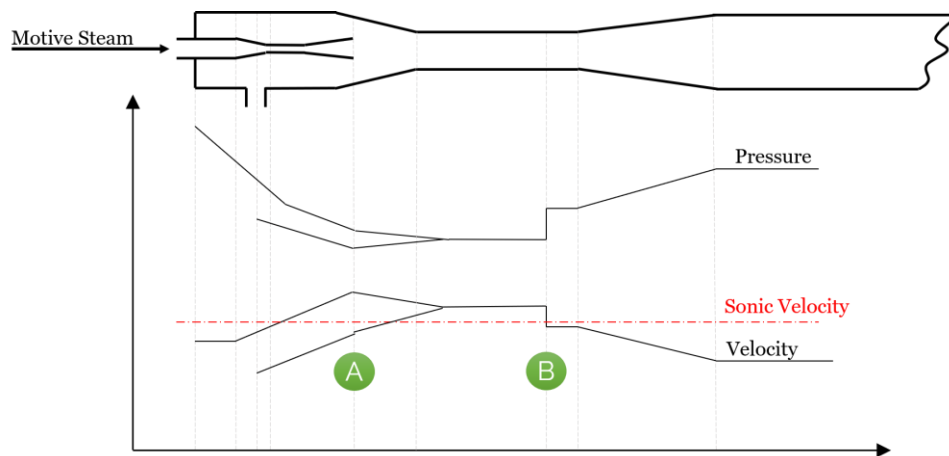
Figure 2.8 – Approximated Pressure and velocity variation inside an ejector.

An ejector that can reach supersonic states can work in three different modes regarding the chocking phenomena [51, 53, 54]. In critical mode, double-chocking occurs and the Entrainment Ratio (ER) is constant. The motive and secondary fluids are chocked simultaneously at the constant-area ejector throat under supersonic conditions. The chocking phenomena limits the maximum flow rate of the secondary fluid.

The shock wave is a phenomenon where the flow decreases its Mach speed from supersonic to subsonic conditions.

The shear layer, where is located the shock wave, is at first created by stable vortex-pairing movements helping the mixture of the two fluids. As the flow becomes developed, the large-scale vortexes become reduced in scale, the energy dissipates until a fully developed turbulent flow is reached [55]. With subsonic flow on one side of the shear mixing layer and supersonic flow on the other, the shear layer is stable and steady [48].

Critical back-pressure (see BP* in Figure 2.9.a) is a threshold value corresponding to the critical point and marking the transition between on-design (before the critical point) and off-design (beyond the critical point) conditions [56]. For back-pressure values below the critical back-pressure, the entrainment ratio remains constant. This limits as well the maximum Coefficient of performance (COP) value [46]. Once the critical back-Pressure is exceeded, the oblique shock wave moves backward towards the primary nozzle, decreasing the axial velocity of the mixed flow [40, 50].

Increasing the backpressure, subcritical mode is reached (see Sub-Critical mode in Figure 2.9.a) and single-chocking occurs. Only the primary flow is chocked, at the nozzle exit, and there is a linear entrainment ratio relation with the backpressure. A series of oblique and normal shock waves occur and moves the shock wave until reaching the primary nozzle interacting with shear layers. The shock waves have dissipative effects and produces a shift from supersonic to subsonic conditions causing major drops on the performance of the ejector. This will force the primary flow to move back to entrance of the entrained flow.
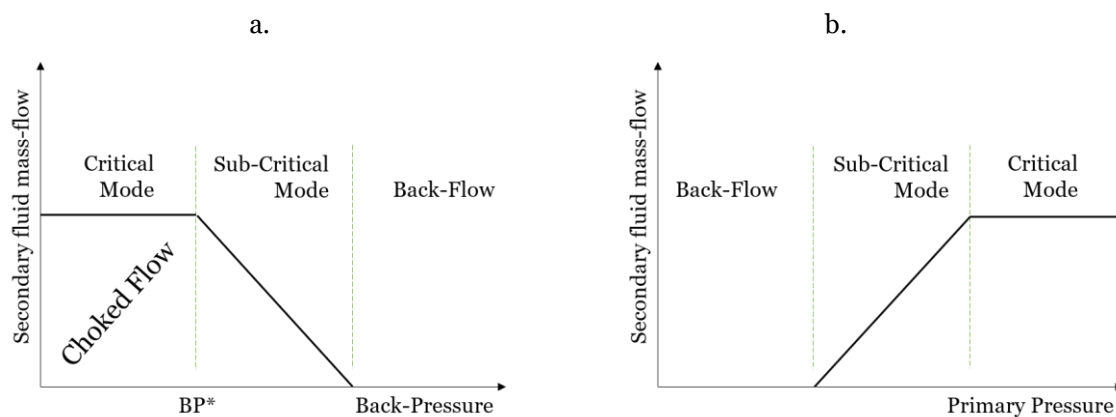
Figure 2.9 - Ejector operational mode.

In the malfunction mode (see Back-Flow in Figure 2.9.a), backflow starts to appearing through the secondary inlet. The phenomena happens when back-pressure is too high to allow entrainment, resulting in over-expanded flow through the nozzle and the development of compression shocks as the motive fluid partially flows back through the entrained fluid inlet [57].

The primary pressure should be as low as possible in order to increase the ejector efficiency and reduce energy costs but high enough to allow the secondary flow to reach sonic speed. When increased, the primary pressure moves the oblique shock wave closer
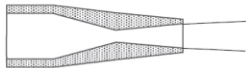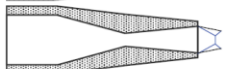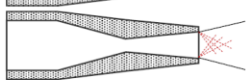
to the diffuser section, increasing the shock intensity, not having significant effect on the entrainment ratio but higher energy spent will be expected. On the other hand, decreasing it below optimum value moves the shock waves closer to the nozzle exit until, similarly to the raise of back-pressure, it causes a reversal flow (see Back-Flow in Figure 2.9.b) [40, 50].

In sum, increasing motive steam pressure above the optimum point will lead to a bigger jet core, smaller effective area, thus lower entrainment ratio. Below the optimum point, the effective area will be bigger than the critical area needed for chocking the secondary flow. In critical conditions, the effective area also reaches critical area in which the secondary flow will start to choke.

The entrainment ratio of an ejector is maximized when the primary flow is perfectly expanded at the nozzle exit and the entrained fluid reaches a chocked condition [58]. In a perfectly expanded flow the compression shocks downstream of the motive fluid come to a halt as the effective flow area of the entrained fluid grows until the static pressure of the motive and the entrained fluid are the same [59]. In normal conditions, perfectly expanded flow is difficult to obtain.

There is normally a certain value of expansion angle. The expansion angle and the supersonic level reached are dependent on the pressure differential between the pressure at the nozzle exit and in the mixing chamber. Over-expanded or under-expanded jets in the mixing section decreases the efficiency of the supersonic ejector [54].

Table 2.4 - Driving flow status at the supersonic nozzle exit [60].

Status	Description	Mach wave	Schematic figure
Ideally-expanded	$P_e/P_s \approx 1$	N/A	
Over-expanded	$P_e/P_s < 1$	Shockwave	
Under-expanded	$P_e/P_s > 1$	Expansion wave	

As shown in Table 2.4, in the case of an under-expanded flow, the primary stream will leave the primary nozzle with divergence of expansion angle. Under-expansion happens when the nozzle's exit pressure is higher than the mixing chamber pressure [61] leading the flow to reach a higher supersonic levels. The increased expansion angle causes the enlargement of the jet core, reducing the effective-area and letting less secondary fluid to be entrained [62].

On the other hand, on an over-expanded flow, the primary stream will leave the primary nozzle with a convergent angle (see Table 2.4). The static pressure at the primary nozzle is lower than the pressure in the mixing chamber, thus the oblique shocks are not as strong as the ones that are produced in an under-expanded flow. Therefore, the flow is more uniform and have less losses in the jet stream's momentum compared to an under-expanded flow [56, 60, 63].

The mixing process inside the ejector has highly irreversible oblique and normal shocks combined which produces shock diamond-shaped jet. The region where the series of shock waves occurs is called the shock train region.

Diamond-shaped shock-waves indicates partial-separation of high-speed primary flow with the surrounding secondary fluid and produces high shear flow region between both flows [61]. Its location is affected by the converging angle [50, 54, 62].

The converging angle can strongly alter the size of the nozzle and the effective area. Studies suggest that the converging angle should be between 0.5º and 10º [50, 64-67] depending on the ejector type, working fluid and operating conditions. Increasing too much the converging angle leads to higher distances between the ejector walls and the jet core, which can generate excessive pressure gradients that causes boundary layer separation near the wall and backflow [53, 54, 66]. The separation region of the boundary layer gradually increases with the vortexes.

Moreover, the active jet core blocks the way of the secondary flow, preventing it from entrained smoothly into the jet core, decreasing the ejector performance.

On the other hand, decreasing the converging angle too much, making the walls to straightened, leads to a deceleration of the entrained fluid due to a reduction of the flow between the jet core and the wall (virtual nozzle) [54, 62, 68]. As there is less secondary fluid flow, the entrained ratio will decrease.
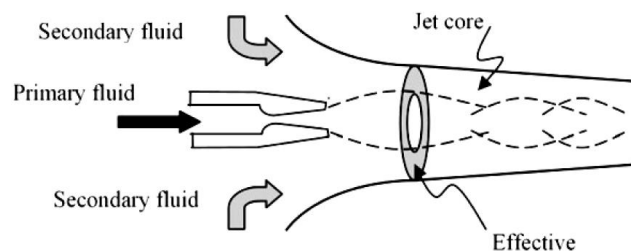
Figure 2.10 - Effective area in the ejector throat.

Considering an idealized case (see Figure 2.10), the effective area is the annulus area between the wall of the ejector mixing area and the primary fluid jet-core [62]. The primary pressure is heavily related to the size of the jet core and effective area. As the primary stream pressure increases, so does the size of the jet core, whilst the effective area decreases.

For a constant secondary pressure and fixed geometry, increasing the temperature and pressure of the motive steam will increase the critical pressure which the ejector can be operated on [50, 63].

However, the ejector entrainment ratio decreases with the increasing of the heat source temperature as shown in Figure 2.11. When the pressure is increased, a smaller effective area is available. Therefore, less amount of the secondary flow is drawn to the mixing chamber while also increasing the primary flow rate [63].

Nonetheless, when having a bigger ejector, increasing the temperature of the primary flow will increase the energy content of the flow, which will reduce the primary flow rate required for the same back-pressure, thus increasing the entrainment ratio [69].
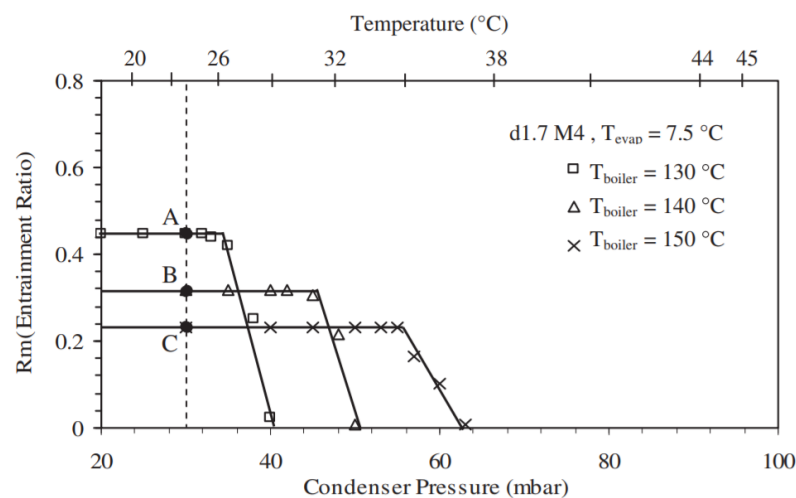
Figure 2.11 - The variation of the entrainment ratio with the primary fluid pressure obtained from CFD simulation [63].

2.2.2 – Ejector design parameters

Obtaining ejectors optimal design is not simple, mainly due to its complex nature of fluid flow mechanisms and its high dependence on working conditions. Entrainment ratio is the most important performance indicator for characterizing the ejector. It is defined as the ratio between the secondary fluid mass flow rate and the primary fluid mass flow. A more detailed explanation and understanding is given bellow in Chapter 3.

The most important geometric parameters of an ejector are the Nozzle Exit Position (NXP), suction chamber angle, area ratio (ratio between the constant area section area and the primary nozzle throat), mixing chamber length and the diffuser angle [70]. Out of these parameters, previous studies showed that NXP and the area ratio play a crucial role on the entrainment ratio [68].

2.2.2.1 – Nozzle Exit Position

The NXP can change the performance of the ejector because it affects directly both the entrainment ratio and effective area section. The influence of the optimum NXP increases with increase in active fluid pressure and was found that the performance of the ejector tend to increase with the decrease in NXP (moving the primary nozzle away from the mixing chamber), after which there is a downfall [53, 54, 68]. Thus, there is an optimum value.

The nozzle shape also affects greatly the ejector operation. The ejector works in sub-sonic regime and it can reach, at most, sonic conditions at the suction exit if the nozzle shape is convergent and it works at supersonic velocities if the nozzle is convergent-divergent shaped [46]. The nozzle diverging section is typically conical and its angle should range from 8 to 15 deg [47].

2.2.2.2 – Area Ratio

Defining the optimal value of Area Ratio (AR) is a trade-off process. In fact, the increase in the AR leads to an increase of the entrainment ratio until an optimum value, after that the entrainment ratio starts to drop. A small constant area section diameter leads to a reduction of the effective area for the secondary flow [71]. Increasing the area ratio moves the shock waves upstream, away from the constant area section. It is due to the existence of vortexes in the mixing chamber. Vortexes leads to significant energy losses and reduces mixing efficiency. By increasing the ejector throat diameter, the vortex phenomena is eliminated [53].

The increase in constant area section will increase the entrainment ratio by enhancing suction from the secondary fluid stream but will affect the compression ratio, lowering it and leading to a decrease in critical backpressure [72].

Critical backpressure decreases with the growing of the AR, thus the ejector starts to operate in subcritical mode, single chocking, with lower backpressures (see Figure 2.12).
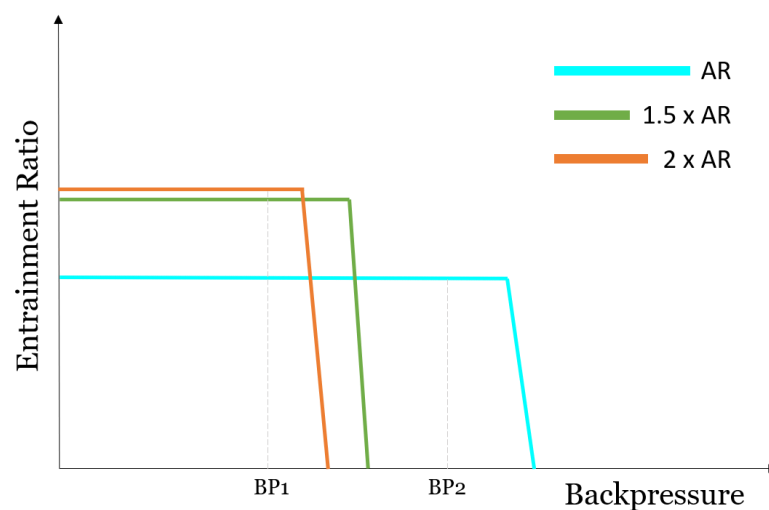
Figure 2.12 - Effect of the area ratio on the entrainment ratio and critical back-pressure.

As seen in Figure 2.12, diffusers with higher area ratio coefficient tend to have bigger ER values (BP1). However, in situations which is required an higher backpressure, a bigger area ratio can cause malfunction in the ejector (BP2).

2.2.2.3 – Constant Area Section Length

The length of the constant area section also has an influence on controlling the shock wave intensity inside the mixing chamber and the constant area section. To maximize the exit pressure, the mixing chamber has to have a length big enough to let the flow reach subsonic speed.

Thus, critical backpressure increases as the ratio between mixing section length and its diameter increases [73], which allows the ejector to operate in double chocking mode in a wider range of conditions [51].

Moreover, there is an almost linear growth in the entrainment ratio with the extension of the length until an optimum point [74], then it starts to decrease due to total pressure losses that happens at the walls because of shear stress [61] (see Figure 2.13). The outcome of incomplete mixing is inadequate pressure recovery and compression within the diffuser.
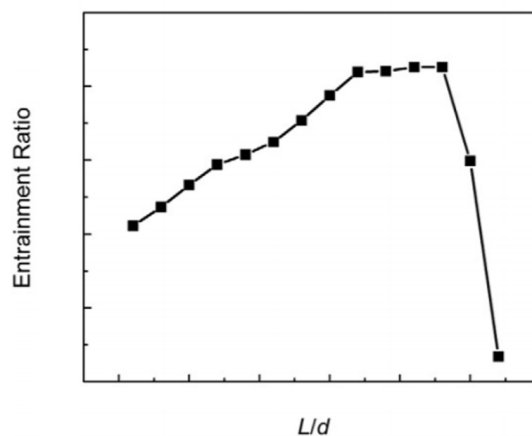
Figure 2.13 - Typical behaviour of entrainment ratio with the growth of the length of the mixing chamber.

2.2.2.4 – Diffuser Angle

The diffusers often play an essential role in many applications, therefore many researchers were concerned in diffuser design. The diffuser has a high divergence angle and therefore low efficiency.

The ejector should have an angle range of 5 to 12 deg, or its axial length should go from 4 to 12 times the throat diameter [47]. However this range is not suitable for all the fluids and operating conditions as well [64].

The performance of the diffuser depends largely upon the completeness of mixing in the constant area section [58]. Moreover, the flow reaching the diffuser should be subsonic for a complete use of the diffuser capacities [75]. Otherwise, the flow exiting the diffuser can have a lower pressure and higher velocity than when the flow entered the diffuser.

Moreover, flow separation can occur at the diffuser which can affect the ejector performance, increasing the entropy in the system.

2.2.3 – Variable Geometry Ejector

One of the main characteristic of ejectors is their high level of optimization for certain type of operating conditions. A fixed-geometry ejector can only be optimized for stable fluid properties and is uncapable of providing stable performance with an unstable heat-input [60], which is the case when the heat source comes from a renewable one, where temperature oscillations and intermittency of the source are expected.

To keep entrainment ratio as high as possible on different conditions, variable-geometry technology should be applied [76]. A variable geometry ejector enables performance regulation by adjusting its configuration. Critical backpressure acts as a limit in performance consistency. As the input temperature drops, the critical backpressure falls below the actual pressure, restraining the entrainment ratio by the backpressure and leads to deficient mixing between the two flows, ultimately leading to lower entrainment ratio [77].

On the other hand, with high temperatures, the driving flow rates increases and extra flow cannot be entrained due to the geometrical restriction in the diameter of the mixing chamber [60]. As the motive flows increase and the secondary one remains the same, the energy consumption will be enhanced and the entrainment ratio decreases.

(a) Performance characteristics of a fixed geometry ejector

(b) Performance characteristics of a variable geometry ejector
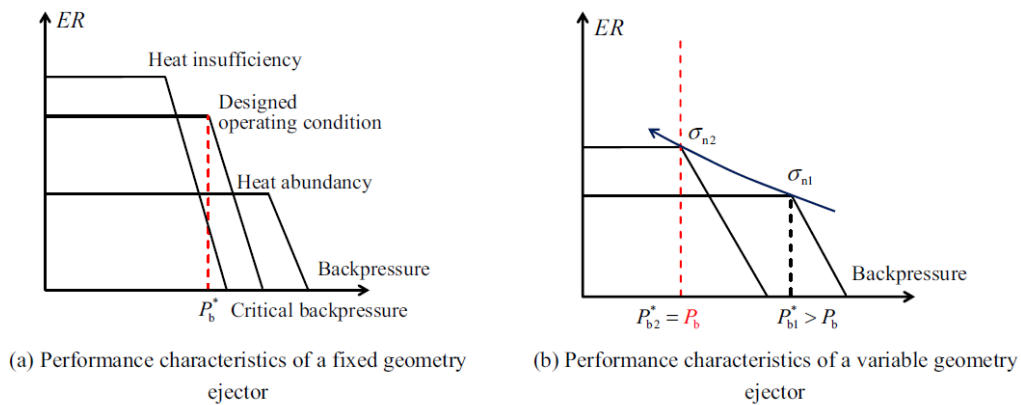
Figure 2.14 - Entrainment ratio and critical backpressure comparison between a fixed geometry and a variable geometry ejector.

As seen in Figure 2.14, diffusers with higher area ratio coefficient tend to have bigger ER values (Pb2 in (b) figure). However, in situations which is required an higher backpressure, a bigger area ratio can cause malfunction in the ejector (Pb1 in (b) figure). Changing the area ratio according to the critical backpressure value (function of the motive flow temperature) keeps the entrainment ratio as high as possible for each operating condition (see Figure 2.14 (a))

The nozzle opening can be changed by changing the spindle position (see Figure 2.15), which regulates the area ratio. The motive flow rate could be reduced or increased depending on the solar energy available. As the spindle moves forward, the primary nozzle throat area decreases leading to an increase in the area ratio [69]. Denis et al. [78] showed that VGE can achieve 8-13% higher solar fraction compared to a fixed-geometry ejector.
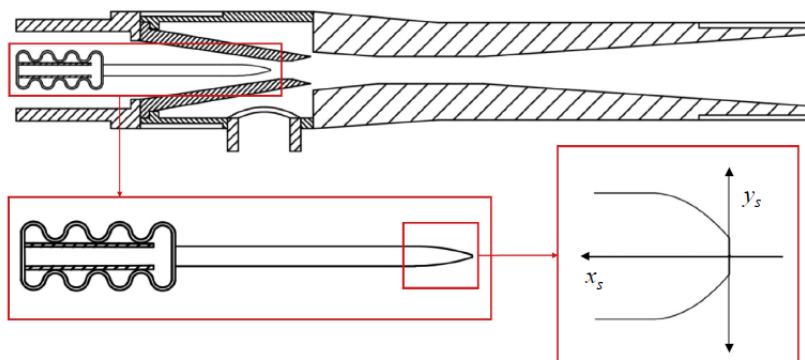
Figure 2.15 - Structure of an auto-tuning AR ejector [79].

Changing the NXP is another way to change the geometry of an ejector. The primary nozzle can be moved back and forth depending on the operating conditions, thus changing its position depending on the temperature and pressure of the motive flow. An ejector with variable NXP may always yield a relatively high entrainment ratio compared to a static one [79].

The entrainment ratio of the adjustable NXP ejector decreases with the increasing of pressure, even though the decreasing amplitude of the entrainment ratio for each temperature is still smaller with the use of a movable NXP than a regular ejector. When the pressure of the motive flow is low, the performance of a variable NXP ejector is almost the same as a non-adjustable NXP ejector because of the nozzle position, further away from the mixing chamber. The optimum NXP decreases as the primary flow pressure increases.

Between NXP-adjustable ejector and AR-adjustable ejector, adjusting the AR has a more significant increase on the entrainment ratio [79]. The larger the difference between the actual and the design back-pressure, the larger the benefits of using the VGE [77].

3. Model Development

Turbulence and how to compute random and chaotic phenomena to improve efficiency. For that matter, turbulence modeling lies somewhere between art and science.

3.1 – Evaluation Parameters

The efficiency of the desalination cycle is very sensitive to the ejector efficiency [80], which increases in efficiency are related to the kinetic energy transfer between the primary and the secondary fluid flows [47].

Expansion ratio is the relationship between the motive gas absolute pressure and the suction absolute pressure and is affected by both operational and geometrical conditions. If the expansion ratio is increased, the mass flow will increase until the maximum flow is reached [81]. Entrainment ratio indicates the entrainment efficiency of an ejector and can be related to the expansion ratio.

Thus, the ER is a good indicator of efficiency because it can be related to the suction as well as the motive pressure in compressible fluids. Hence, the ejector geometry optimization goal is to find the optimal geometry configuration which can achieve the highest entrainment ratio.

In an ejector the flow of a motive fluid creates a suction pressure in a designed chamber where the entrained fluid is present and get sucked. ER is defined as the mass flow rate of the motive flow divided by the mass flow rate of the secondary flow handled at the same suction and discharge pressure (see Equation 3.1).

$$Entrainment\ Ratio = \frac{mass\ flow\ rate\ of\ the\ motive\ stream}{mass\ flow\ rate\ of\ the\ propelled\ stream} \qquad \textbf{3.1}$$

As seen in equation 3.1, the higher the entrainment ratio is, the lower the flow rate on the primary nozzle flow, thus the lower the required generator energy input will be needed. ER is affected by both operating conditions and geometry [51].

3.2 – Modeling methods

The design of ejectors relies on the application of the equations of continuity, momentum and energy. Numerous modelling methods exist (see Figure 3.1) with distinct complexity and accuracy.
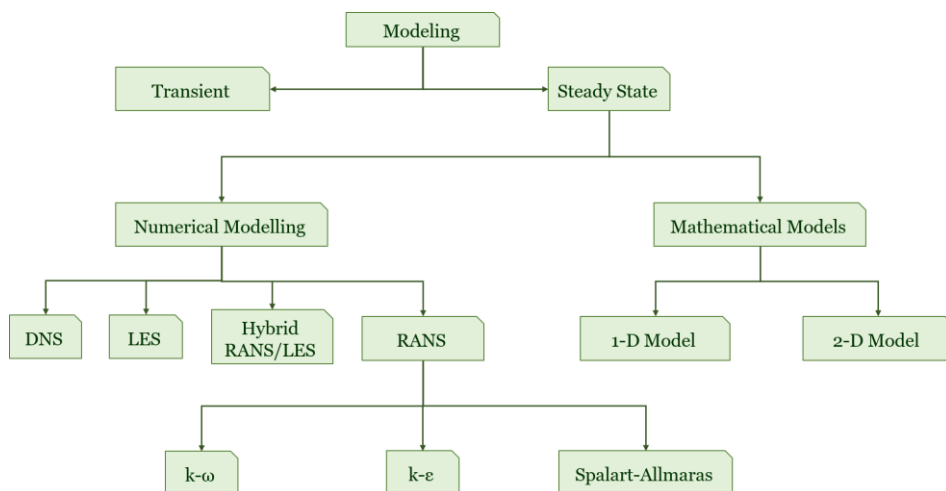
Figure 3.1 – Diagram tree of different methods to model a fluid problem

A one-dimensional analysis can be a reasonable approximation for engineering design purposes. It has been shown to give consistent and reasonably accurate results within its limitations [82].

However, there are obvious limitations that cannot be ignored when looking to the accuracy that can be achieved by modeling a real flow process using one-dimensional equations [83] such as the details of the velocity, pressure and temperature profiles of the stream in the ejector. The improvements in computational power brought the research into ejector design codes that could solve differential equations. The constant pressure and constant area models are one-dimensional approaches to designing an

ejector. A lot of assumptions are made on these approaches making the method not entirely accurate [84].

The two-dimensional method is more accurate, however it is difficult to implement in design optimization due to the complicated equations. The technique is usually ruled out as an effective method because of the number of empirical coefficients required [85].

Numerical models have proven to be the most reliable tools to simulate fluids inside ejectors because of the understanding it can provide about complex fluid flow problems, such as the entrainment and mixing processes [51]. Despite being more complex, expensive and time consuming, numerical models can accurately predict various flow phenomena that mathematical models do not take into account such as shock waves, mixing and complex flows.

The two most critical factors affecting the definition of the problem are the choice of the physical model, especially the turbulence model and the mesh quality.

3.2.1 – CFD modeling

CFD, when implemented correctly, is a low-cost and quick test method. As a designing tool, it helps the optimization of a process with high reliability and at a fraction of the cost and time of traditional design approaches that would involve the manufacture of several prototypes [86].

The numerical simulations should not be treated like a Blackbox. As seen in Figure 3.2, in a Blackbox, input is given and an output is got without knowing what is happening in between.

Figure 3.2 - Blackbox representation.

If there is no knowledge about what is happening in the simulation, the results can be wrong and not meaningful. A numerical simulation should look like Figure 3.3.
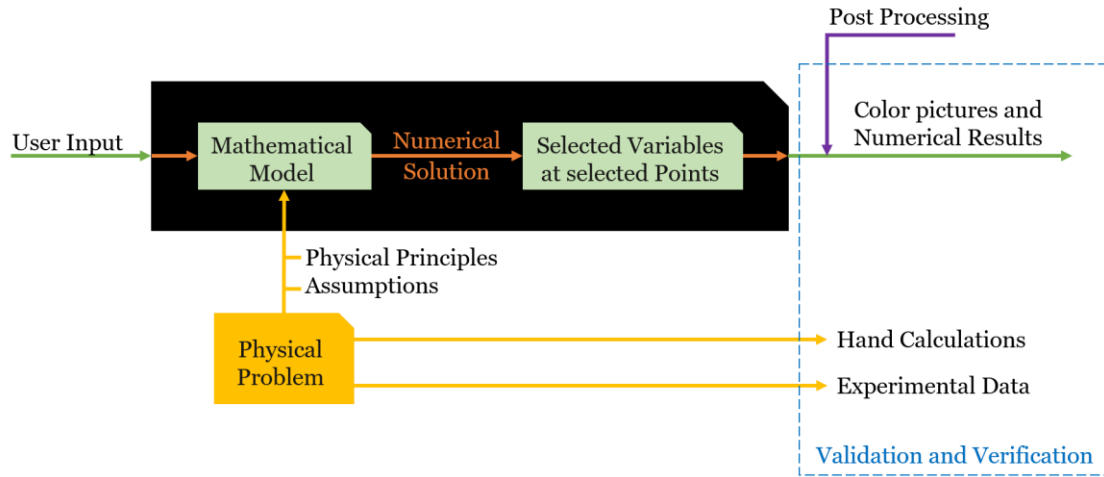
Figure 3.3 - Schematic representation of the numerical modeling process.

The CFD tool calculates the mathematical model of the physical problem based on physical principles, such as the governing equations and other assumptions embedded on it.

Most CFD models solve the compressible Navier-Stokes equations. The equations rely on the conservation of energy, momentum and continuity equations in order to find values for the three key unknown variables:

Continuity:
$$\frac{D\rho}{Dt} = \rho \, div \, \mathbf{v}$$
3.2

Momentum:
$$\rho \, \frac{\partial}{\partial t}(\rho \, v_i) + \rho \frac{\partial}{\partial x_j}(\rho \, v_i \, v_j) = -\frac{\partial p_i}{\partial x_i} + \frac{\tau_{ij}}{\partial x_j} + F_{ext}$$
3.3

Where F_{ext} represents all the external forces applied to the flow (e.g., gravitational body force), which in this study, is null.

Energy:
$$\rho \, \frac{Dh}{Dt} = \frac{DP}{Dt} + \, div(k\nabla T) + \, \tau_{ij} \frac{\partial v_i}{\partial x_j}$$
3.4

The term τ_{ij} in equations 3.3 and 3.4 represents the viscous flow tension in **ij,** general space coordinates (2D), and it can be written as

$$\tau_{ij} = 2\,\mu\,S_{ij} \qquad\qquad \textbf{3.5}$$

Where μ is the dynamic viscosity of the fluid and S_{ij} is the strain rate tensor. The strain rate tensor is defined as follows:

$$S_{ij} = \frac{1}{2}\left(\frac{\partial v_i}{\partial x_j} + \frac{\partial v_j}{\partial x_i}\right) \qquad\qquad \textbf{3.6}$$

After the CFD solves the numerical problem, it selects variables at selected points. The chosen points can be corners, sides or center of the grid, depending on the method used.

When the points selected are centers of the grid, the software uses finite-difference methods to model the flow process. Therefore, the governing equations are discretized using the finite volume approach and are solved using the coupled-implicit solver [53]. Finite-difference methods do not require the form of velocity and temperature distributions to be specified like integral equations do. However, in CFD, the time required for setting the grid parameters remains the main drawback.

There is a strong need to shorten the simulation errors and to check the result credibility. Therefore, the systematic process to check the results is called verification and validation. The verification part check if the model was solved the right way. It inspects possible errors on the numerical solution and compares it with hand calculations that were done. On the other hand, validation verify if the model is the right one for the case. It inspects if the mathematical model is a reasonable representation of the physical problem and if the assumptions are acceptable.

3.3 – Computational Mesh

The partial differential equations that govern fluid flow and heat transfer are not typically receptive to analytical analysis, except for very simple cases. Hence, in order to analyze fluid flows, flow domains are split into smaller subdomains.

The quality of the mesh is one of the most important parameters in the CFD simulations. The grid independence needs to be studied in order to minimize the impact of the grid size and the computational cost. The grid size needs to be optimized to be small enough to guarantee that the results are independent of the mesh, but large enough to run the model efficiently and at an acceptable speed [87]. When using more and smaller cells, the needed geometrical accuracy given by the model on the walls, for example, is much higher.

Care must be taken to ensure proper continuity of solution across the common interfaces between two subdomains so that the approximate solutions inside various portions can be put together to give a complete picture of fluid flow in the entire domain. The subdomains are often called elements or cells, and the collection of all elements or cells is called a mesh or grid [88].

The error and uncertainty in CFD simulations come from discretization errors, rounding errors, iteration errors or physical errors. The discretization errors have the biggest impact on the total error count. Discretization is a process that converts the physical equations to a system of algebraic ones as pictured on the transition between the physical problem and the mathematical one in Figure 3.3. The most common discretization processes are finite difference, finite element and finite volume [89]. Most commercial CFD's software are finite volume based. The finite volume method is easier to implement and is more stable compared with the other two methods [90].
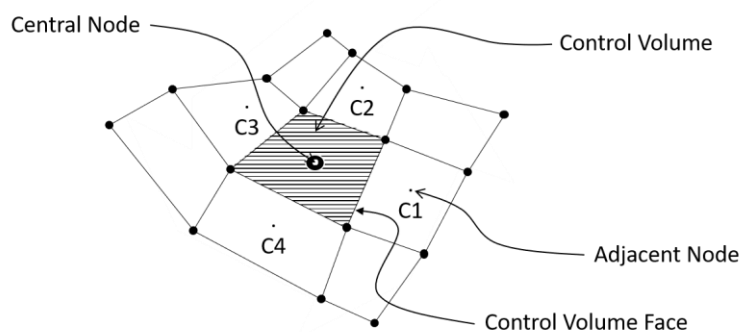
Figure 3.4 - A representation of a structured mesh arrangement [90].

Figure 3.4 illustrates the discretization of the governing equations by a finite volume technique. The control-volume technique consists on dividing the domain into discrete control volumes using a computational grid, integrate the governing equations on the individual control volume to generate algebraic equations and linearize the discretized equations and the resulting linear equation system to updated values of the variables (velocity, pressure, temperature, etc.). Discrete values of the equation are sorted at the cell center (Central Node, C_1, C_2, C_3 and C_4). The equations also require a face value. The face value is calculated using an upwind scheme. The upwind scheme means that the face value is calculated from the cell-center value of the cell upstream relative to the direction of the velocity.

Finite volume methods demand the equations to be processed in a proper order to compute the solution efficiently. Thus, for the profile method to present low computational cost it is necessary to re-order the equations. Performing a vertex reordering is equivalent to reorder a system of equations, and also equivalent to reorder the equations in partial differential equations finite-volume discretization [91]. Moreover, the computational cost of iterative solvers for the numerical solution of a sparse linear system of equations can be reduced by using a heuristic for matrix profile reductions [92].

Node reordering can be done by the Cuthill–McKee (CM) or the Reverse Cuthill–McKee (RCM) algorithms. The RCM algorithm (see Figure 3.5) provides similar results at a lower cost in terms of time than the CM algorithm. The algorithm reduces the bandwidth of a matrix by reordering nodes in a mesh (or vertices in a graph) in the degree order. This will allow the use of less memory and also the solution to converge faster. The degree order begins from the starting node (the lowest degree node) to all nodes adjacent to it in their degree order (lowest degree first) are added [93].
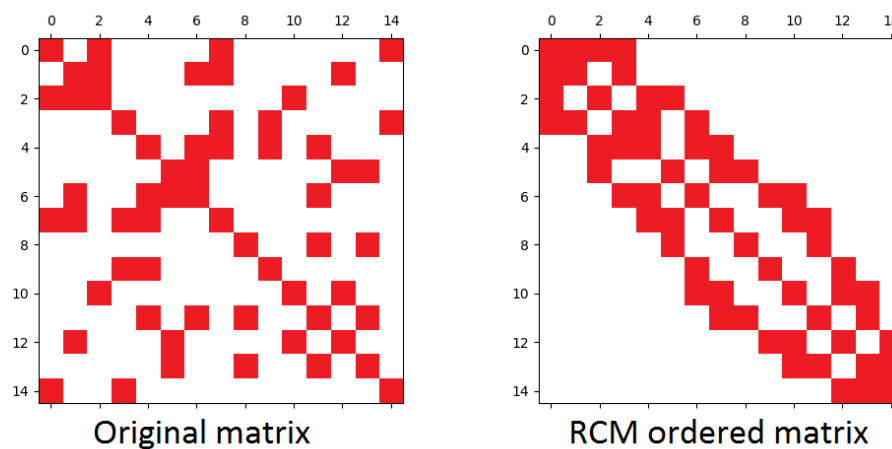
Figure 3.5 - Representation of a RCM re-order [93].

When constructing discrete numerical representations of differential operators using local discretization (as finite difference, finite volume, and finite element), one choice of estimating quantities can be based on neighbors in all directions equally (i.e. central differencing), but the estimations can also be biased in the direction from which information is propagating (i.e. up-winding). The upwind scheme mimics the basic physics of advection in that the cell face value is made dependent of the upwind nodal value, i.e. dependent on the flow direction.

There are four main upwind schemes:

First-Order Upwind Scheme:
The face quantities are considered identical to the cell quantities. Thus the face value is set equal to the cell-center value of the upstream cell [94].

Second-Order Upwind Scheme:
The face value is calculated from an equation that uses a multidimensional linear reconstruction approach [95]. The equation relates the gradient of the upstream cell with the displacement vector from the centroid of the upstream cell to its face [94].

Power Law Scheme:
The power-law discretization scheme interpolates the face value of a variable, using the exact solution to a one-dimensional convection-diffusion equation [94].

QUICK Scheme:
QUICK scheme is based on a weighted average of second-order-upwind and central interpolations of the variable [96]. The QUICK scheme will typically be more accurate on structured grids aligned with the flow direction [97].

In the momentum governing equations, the velocity and pressure parameters are coupled. There are two main types of methods for solving discretized algebraic equations of momentum when using a pressure-based solver (see Figure 3.6): Coupled Method and Segregated Method.

A coupled method is characterized by the simultaneous solution of the velocity and pressure parameters. Coupled methods have been widely employed for the computation of compressible flows, whereas segregated methods have been opted for the computation of incompressible flows. Unlike a coupled solution, a segregated method solves velocity and pressure fields separately or consecutively [98].
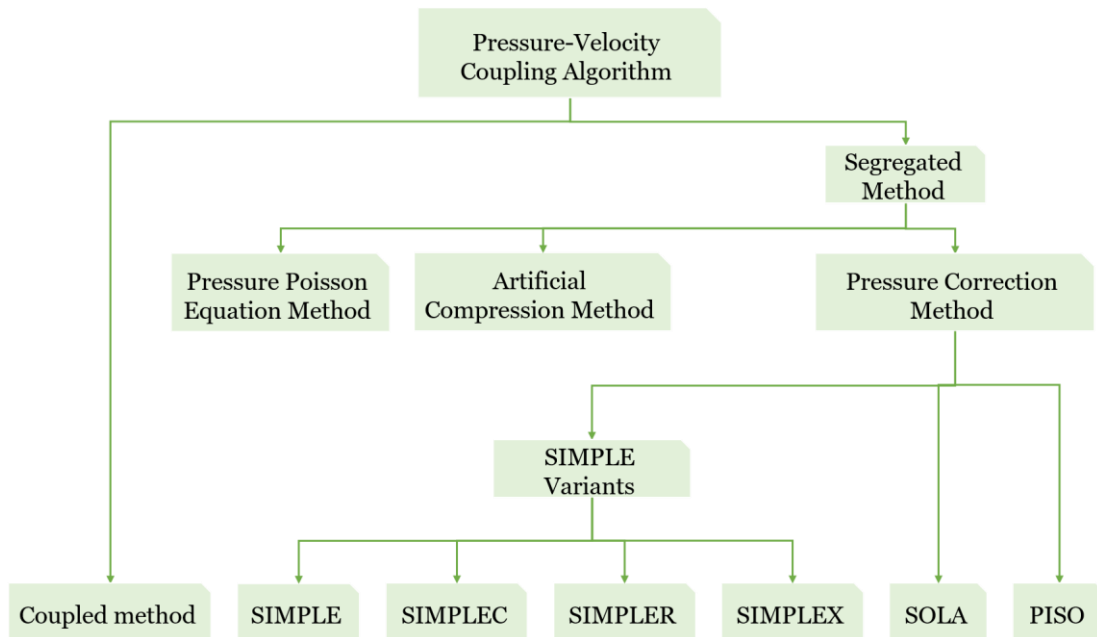
Figure 3.6 - Classification of different pressure–velocity coupling algorithms [98].

3.4 – Turbulence

Turbulence is an unsteady and irregular motion in which transported quantities of mass and momentum fluctuate in time and space [97]. Moreover, in a turbulent flow, fluid properties and velocity exhibit random variations.

Turbulence can also be understood by understanding the changes in the Reynolds number (See equation 3.7). Reynolds number represents the ratio between inertial forces and viscous ones.

$$Re = \frac{\rho \, v \, D}{\mu} \qquad\qquad \textbf{3.7}$$

At low Reynolds numbers, viscous forces control the fluid and every disturbance is rapidly reduced. With the increase of the Reynolds number, these disturbances begin to amplify and eventually lead the flow into turbulent conditions. The disturbances tend to grow, become non-linear and interact with neighboring disturbances starting a snow-ball effect with eventually, the flow reaching a chaotic state. Therefore, turbulence is a three-dimensional unsteady and random viscous phenomena that happens at high Reynolds number [99].

Turbulent flow have higher rates of mass and momentum transfer compared to laminar flows. Thus, turbulent flows are highly desirable when the objective is enhancing the mixing of the flows. However, the diffusiveness of turbulent flows thickens the shear and boundary layers.

Eddy is the swirling of a fluid, that creates a space devoid of downstream flowing fluid. There is backflow causing the fluid to rotate.

The turbulent flow contains a wide range of turbulent eddy sizes. Eddies can transfer much more energy and dissolved matter within the fluid than can molecular diffusion in the nonturbulent flow because eddies actually mix together large masses of fluid [100]. Flow composed largely of eddies is called turbulent; eddies generally become more numerous as the fluid flow velocity increases [101]. The interactions between the large-scale motions of turbulence and the small ones creates an energy cascade in the flow as seen in Figure 3.7. There is a hierarchy of eddies over a wide range of length scales, thus a transfer of energy from the large scales of motion, which contains most of the kinetic energy of the flow, to the small scale ones, which are responsible for the viscous dissipation of turbulent kinetic energy [102]. The small-scale eddies are feed off the large energy production eddies. The wave number is inversely proportional to the turbulent length scale.
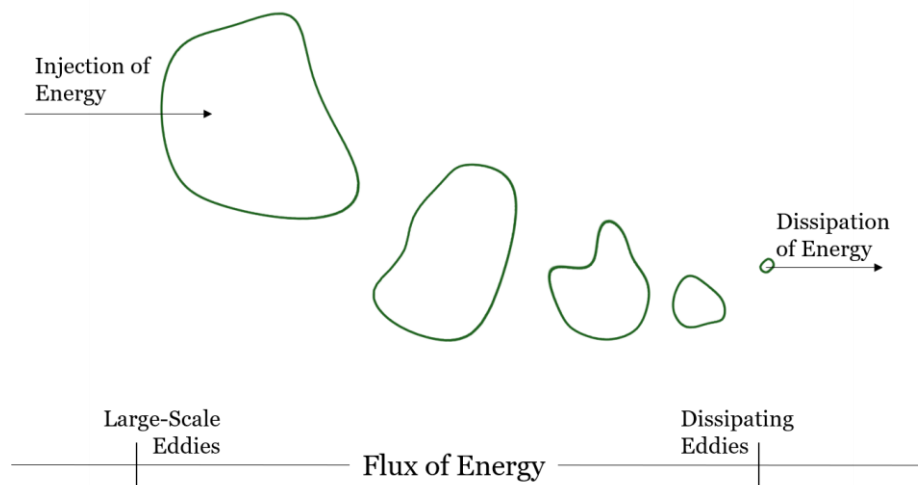
Figure 3.7 – Energy Cascade of Richardson.

Turbulence models are classified by which turbulent scales are used to solve the unsteady Navier-Stokes equations on a computational grid [103].

3.4.1 – Turbulence Simulation and Mathematical Models

Direct Numerical Simulation (DNS) of the turbulent energy cascade using the Navier-Stokes equations require the grid spacing to be smaller than the smallest turbulent length scale. Such small scales require enormous amounts of grid points, which are impractical [99].

Moreover, most of the DNS models requires uniform spacing computational grids. Uniform grids conditions combining with small cell sizes leads to very large numerical grids even with small Reynolds numbers. DNS attempts to simulate all of the scales of turbulence without modeling. A DNS solution is inherently unsteady, so it must be run for long periods to assure that the solution is statistically stationary.

Large Eddy Simulation (LES) models only the smallest turbulent scales. As the smaller turbulent scales are almost isotropic, it can be modeled with simple turbulence models. Hence a simple turbulence model is used to simulate the turbulence scales that cannot be realized on the computational grid and the Navier-Stokes equations are solved for the remaining scales. LES solutions must be run a large number of time steps to allow

the solution to reach a statistically stationary state [104]. LES models has been found quite accurate for lower Reynolds number flows [105]. The governing equations used for LES are obtained filtering the time-dependent Navier-Stokes equations in either Fourier (wave-number) space or physical space. This process makes possible to filter the eddies whose scales are smaller than the filter width (or grid spacing) used in the computations. Therefore, the resulting equations govern the dynamics of large eddies only [94].

Reynolds Averaged Navier-Stokes (RANS) uses a time averaging process to remove the necessity of simulating all the scales of the turbulence spectrum. RANS uses one length scale to characterize the entire turbulent spectrum [104]. Since RANS uses a single length scale, the model has to be able to find one length scale that is appropriate for all cases. Afterwards, the flow can be treated as a steady flow and all the unsteadiness are assumed to happen at scales below the computational grid size, thus, calculated with the turbulence model [99]. RANS model does not contemplate density changes along time. In most cases it is accurate enough, since turbulent fluctuations most often do not lead to any significant fluctuations in density [106].

In highly compressible flows and hypersonic flows is it necessary to perform the more complex averaging method, called Favre averaged Navier-Stokes.
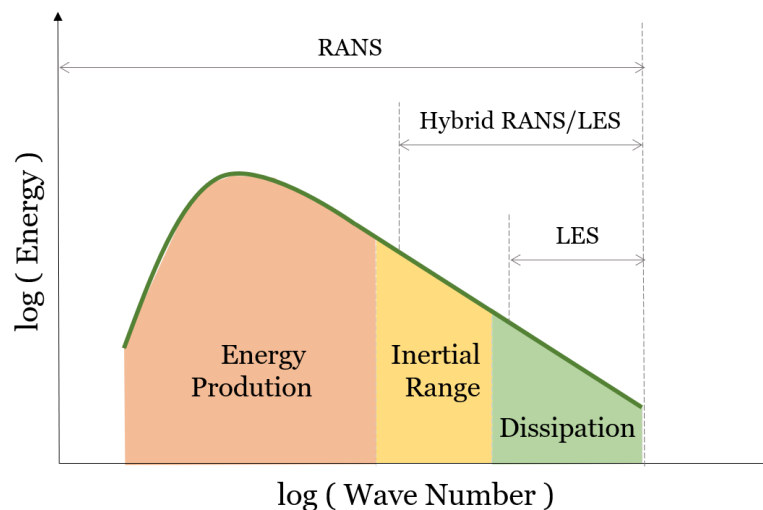
Figure 3.8 – Different turbulence models on the energy spectrum.

3.5 – Reynolds Averaged Navier-Stokes equations

The governing equations (Equations 3.2, 3.3, 3.4) presented on page 38 are impossible to solve for a turbulent flow due to the mass and momentum fluctuation in time and space [107]. Hence, Reynolds Averaged Navier-Stokes method looks at the flow as statistical variances and fluctuations of the changing variables (see Figure 3.9).

In RANS, for a statistically stationary flow, the solution variables in the exact Navier-Stokes equations can be break up into time-averaged and turbulent-fluctuation terms [108].

The velocity can be written as:

$$v_{i,t} = \bar{v}_i + v'_{i,t} \qquad \textbf{3.8}$$
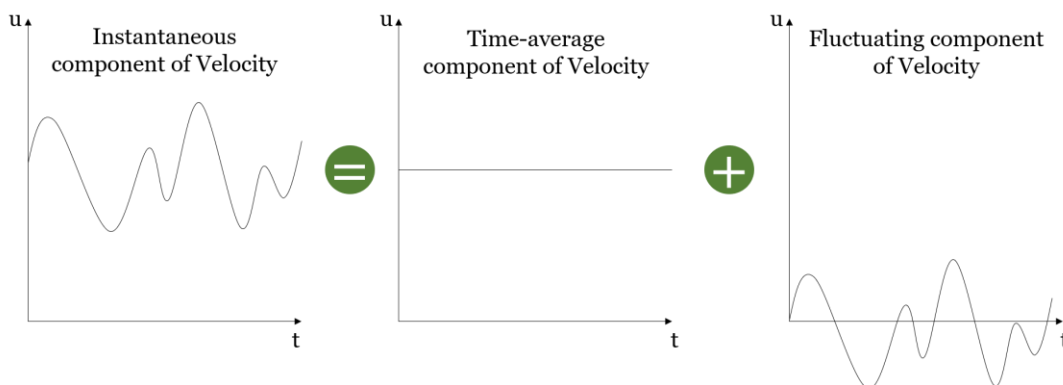
Figure 3.9 – Representation of how RANS uses time-averaging of fluctuation components of velocity.

Where $\bar{v}(x)$ and $v'(x,t)$ are the mean and fluctuating velocity, respectively. The average velocity $\bar{v}$ is defined as:

$$\bar{v} = \frac{1}{2T} \int_{-T}^{T} v \, dt \qquad \textbf{3.9}$$

The time scale of the integration T must be bigger than the turbulent time scales in order to the flow be statistically stationary. The time average of fluctuating velocity v' is defined as:

$$\overline{v'} = \frac{1}{2T} \int_{-T}^{T} v' \, dt = \frac{1}{2T} \int_{-T}^{T} (v - \bar{v}) \, dt = 0 \qquad \textbf{3.10}$$

The Reynolds averaging process, steady-state correlation terms replace the unsteady behavior of the turbulent flow, reducing the computer time requirements for obtaining satisfactory results. The Reynolds-averaged Navier-Stokes equations have the same general form as the instantaneous Navier-Stokes equations. Hence, applying the core principals of RANS to the conservation of momentum equation (Equation 3.3 page 38), the Reynolds-averaged momentum equations are as follows:

$$\rho \left(\frac{\partial v_i}{\partial t} + v_j \frac{\partial v_i}{\partial x_j} \right) = -\frac{\partial P}{\partial x_i} + \frac{\partial}{\partial x_j} \left[\mu \left(\frac{\partial v_i}{\partial x_j} + \frac{\partial v_j}{\partial x_j} \right) + R_{ij} \right] \qquad \textbf{3.11}$$

R_{ij} stands for the Reynolds stress tensor, which represents the stochastic fluctuations of the velocity. This is an additional unknown value introduced by the averaging procedure. Closure of the equation set requires correlations to be developed for the new terms that will appear. In order to secure the best results as possible, the correlation terms must be calibrated for every specific condition, even though some quantities cannot be measured. The RANS model can be closed with the development of more transport equations for the turbulent stresses and turbulent dissipation. This approach to closure is called Reynolds Stress Model (RSM). Although being very accurate in complex 3D flows, the model is very complex and computational intensive [99]. This hypothesis assumes that the Reynolds stresses can be related to the mean velocity gradients and turbulent Reynolds stresses are modeled using turbulent viscosity, μ_T :

$$R_{ij} = -\rho \, \overline{v'_i \, v'_j} = \mu_T \left(\frac{\partial \bar{v}_i}{\partial x_j} + \frac{\partial \bar{v}_j}{\partial x_i} \right) - \frac{2}{3} \, \delta_{ij} \left(\mu_T \frac{\partial \bar{v}_k}{\partial x_k} + \rho \, k \right) \qquad \textbf{3.12}$$

The Reynolds-averaged approach to turbulence modeling requires that the Reynolds stresses in equation 3.11 are correctly modeled.

The third expression in equation 3.12 reflects the Boussinesq hypothesis. The hypothesis relates the Reynolds stresses to the mean velocity gradients through the eddy viscosity. Eddy viscosity (similar to molecular viscosity) is used to model the transfer of momentum due to the turbulence. T higher level of turbulence means a greater value of eddy viscosity.

Although calculating the Reynolds stress tensor via Reynolds Stress Transport Model (the second expression of equation 3.12) gives clearly superior results in some situations, the additional computational expense is not justified [94]. The Boussinesq hypothesis has reasonably good results for simple turbulent shear flows like boundary layers, round jets and mixing layers [109]. The hypothesis is used in the Spalart-Allmaras model, the k-ε and k-ω turbulence models.

Turbulence models are needed in RANS models to calculate μ_T based on dimensional analysis.

3.6 – Turbulence Models

Navier-Stokes equations can fully describe the turbulent flow. However, computer processing power has not reached the performance needed to solve the Navier-Stokes equations for complex flows in a practical time. Turbulence requires the resolution of wide range of length and time scales.

The choice of the turbulence model to be used should be specific for each type of flow, there is no universal turbulence model that fits all the situations [107].

3.6.1 – One Equation Turbulence Models

One equation turbulence models solve one turbulent transport equation, usually the turbulent kinetic energy. The most popular one-equation models are the Baldwin-Barth model and the Spalart-Allmaras Model.

3.6.1.1 – Spalart-Allmaras Model

The Spalart-Allmaras Model is a low-cost RANS model that solves a transport equation for a modified turbulent viscosity. The model has shown to give reasonably accurate results for boundary layers subjected to adverse pressure gradients [109]. However, the model requires the calculation of the distance to the nearest wall for all field points, which leads to high computational effort, especially for unstructured grid

codes. Moreover, the model contains no corrections for compressibility and tend to overpredict the growth rate of high speed shear layers [99].

$$\mu_T = f(\tilde{v})$$

Where $\tilde{v}$ is a viscosity-like variable. This may also be referred to as the Spalart-Allmaras variable. Boundary conditions are set by defining values of $\tilde{v}$.

3.6.2 – Two Equation Turbulence Models

Two-Equation Turbulence Models solve a transport equation for turbulent kinetic energy (k) and a second transport equation. This allows the determination of both, a turbulent length and a time scale to be defined.

Two equation models differ in the treatment of the wall and the form of the turbulent dissipation equation, derived from the Navier-Stokes equations. The two most popular equations used to close the turbulence model are based on the dissipation, ε^2, and on a turbulence variable, ω, as known as turbulent specific dissipation.

There is no general consensus on the choice 2of the adequate turbulence model for supersonic ejector modeling [110]. Most researchers agree towards the use of k-ε turbulence model [51, 61, 111, 112] for better agreement with experimental data and a higher accuracy in predicting the spreading rate of both planar and round jets. Moreover, k-ε turbulence model has better shock prediction capability along with the ejector.

3.6.2.1 – *k-ω* Turbulence Models

The k-ω Turbulence Models solve the transport equations for the turbulent kinetic energy (k) and for the specific dissipation rate (ω):

$$\mu_T = f\left(\frac{\rho\,k^2}{\omega}\right)$$

The k-ω Turbulence Models enable a more accurate near wall treatment with an automatic change from a wall function to a low-Reynolds number formulation based on grid spacing. It has superior performance for wall-bounded, and low Reynolds number flows compared to k-ε Turbulence Models.

The k-ω Turbulence Models are derived for wall-bounded flows, thus the equations do not hold terms which are undefined at the wall. The model require no additional wall damping terms when used in boundary layer flows [99].

The model is accurate and robust for a wide range of boundary layer flows with pressure gradient. However, the model underpredicts the amount of separation for severe adverse pressure gradient flows, requires a high mesh resolution near the wall and has difficulty of convergence depending on the initial conditions.

3.6.2.2– k-ε Turbulence Models

The classical k-ε turbulence model uses turbulent viscosity (μ_t) as

$$\mu_t = \rho \, C_\mu \, \frac{k^2}{\varepsilon} \qquad\qquad \textbf{3.15}$$

Where C_μ is a constant. This value is found based on experiments for fundamental turbulent flows.

The turbulent kinetic energy, k, and its rate of dissipation, ε, are obtained from the Reynolds-averaged equations. Turbulent dissipation is the rate at which velocity fluctuations dissipate.

The standard, RNG and realizable k-ε turbulence models differ in:
- The method of calculating turbulent viscosity
- The turbulent Prandtl numbers governing the turbulent diffusion of k and ε
- The generation and destruction terms in the ε equations

Standard *k-ε* Model

The standard *k-ε* model makes use of transport equations for the turbulence kinetic energy (k) and its dissipation rate (*ε*). The model transport equation used to calculate the turbulence kinetic energy is derived from the exact equation, while the model transport equation used to calculate the dissipation rate is obtained using physical considerations. An additional damping term must be added for the eddy viscosity to include a proper behavior in the near wall region [99].

The eddy viscosity is calculated from a single turbulent length scale, hence the calculated turbulent diffusion occurs only at a specific scale of eddy sizes.

The standard *k-ε* model is a semi-empirical model and the derivation of its model equations relies on result-driven considerations and empiricism [94]. The model has three constants which are empirically determined from comparisons with experimental data for fundamental turbulent flows. All the empirical constants are determined for stable conditions, hence, they are not entirely valid when the production and dissipation of turbulent kinetic energy are not the same. I.e. the flow is assumed fully turbulent and it neglects the molecular viscosity.

As the strengths and weaknesses of the standard *k-ε* model become known, modifications have been introduced to improve its performance [94]. The *k-ε* turbulence models are robust, computationally affordable and reasonable accuracy for a wide range of turbulent flows but tend to over-predict turbulence generation when strong local accelerations are part of the flow [110] and performs poorly for complex flows involving severe pressure gradient, separation and strong streamline curvature.

The RNG and realizable versions of the *k-ε* model do modifications in the transport equation for ε to control the *k-ε* model over-predictions.

RNG *k-ε* Model

The RNG model is derived from the instantaneous Navier-Stokes equations, using a statistical technique called "renormalization group". The RNG and realizable versions of the k-ε model do modifications in the transport equation for ε to control the standard *k-ε* model over-predictions of the recirculation length in separating flows [113].

Some coefficients in Standard *k-ε* Model are constants whereas the RNG *k-ε* model treats all coefficients as functions of the flow parameters which accounts for low-Reynolds number effects. This change lets the model handle transitional flows at different turbulent length scales.

Moreover, the RNG model has an additional term in its *ε* equation that improves the accuracy for rapidly strained flows [94].

RNG model has as its most significant limitation the instability of convergence due to non-linearities in the model [94].

Realizable *k-ε* Model

The realizable model is an improved method for calculating the turbulent viscosity. It is more accurate than the standard version of *k-ε* model to predict the distribution of the dissipation rate of round jets as well as the prediction of the boundary layers characteristics when in large pressure gradient and recirculating flows [114].

The realizable-model proposed by Shih et al. [115] was intended to address these deficiencies of traditional-models by adopting a new eddy-viscosity formula involving a variable originally submitted by Reynolds [116] and a new model equation for dissipation (ε) based on the dynamic equation of the mean-square vorticity fluctuation [94].

The equation for the dissipation rate is derived from the exact equation for the transport of the mean-square vorticity fluctuation.

One limitation of the realizable-model is that it produces non-physical turbulent viscosities in situations when the computational domain contains both rotating and stationary fluid zones. This is due to the fact that the realizable-model includes the effects of mean rotation in the definition of the turbulent viscosity [94].

This model has been extensively validated for a wide range of flows [63, 94] including free flows such as jets and mixing layers. For all these cases, the performance of the model has been found to be substantially better than that of the standard-model.

It is noteworthy that the realizable-model can predict the spreading rate for axisymmetric jets as well as that for planar jets.

Since the model is still relatively new, it is not clear in exactly which instances the realizable k-ε model consistently outperforms the RNG model. However, initial studies have shown that the realizable model provides the best performance of all the k-ε model versions for several validations of separated flows and flows with complex secondary flow features [117].

3.7 – Ansys FLUENT/ICEM CFD

FLUENT is a highly developed commercial software for modeling fluid flows and heat transfer in complex geometries. FLUENT is able to model a wide range of incompressible and compressible, laminar and turbulent fluid flow problems with high-level accuracy.

Preprocessing is the first step in creating and study a flow model. It includes building the model with an appropriate mesh and boundary layers. ICEM is a preprocessing tool that provides advanced geometry/mesh generation functions useful for in-depth analysis of aerospace, automotive and electrical engineering applications. It is a powerful and highly manipulative software which allows the user to generate grids of high resolution [118]. As there is no singular meshing method which can be used for every problem, ICEM CFD allows different types of grid structures to be created such as Multi-block structured meshes, Unstructured meshes and Hybrid meshes [119]. ICEM was used as the preprocessor for all the simulations in this study. The ejector geometry was designed as a 2-D axis-symmetric.

After preprocessing, the CFD solver has to transform the partial differential Navier-Stokes and the governing equations into algebraic ones. Fluent uses discretization to convert the flow's continuous partial differential equations into a discrete system of algebraic equations.

3.8 – Remarks Regarding the Model

After a detailed analysis of the main parameters to study when developing a model to evaluate the performance of ejectors with different variables, it is possible to draw the following conclusions regarding the model:

1. Entrainment ratio should be the main evaluation parameter when comparing different ejector designs and conditions. The study should be made with the objective of increasing the entrainment ratio as much as possible.

2. As 1-D model calculations were made by a previous project, numerical modelling should be next step on optimizing the ejector geometry.

3. The mesh, as one of the most important factors on the CFD simulations, should be made with the utmost care and precision to ensure that the results are independent from the mesh itself. The grid cells should be as quadrangular as possible and near-wall cells must be within the y+ region.

4. A node reordering should be done with the RCM to reduce computational costs.

5. Second-Order Upwind Scheme and QUICK Scheme should be chosen as the upwind schemes since they are the most accurate schemes to use [120].

6. Coupled methods should be used as the Pressure-Velocity coupling algorithms since the steam ejector flow is compressible.

7. RANS shall be the chosen turbulence model as it is computationally less expensive and simulate all the turbulence spectrum.

8. Two equation turbulence models are preferred because include two extra transport equations to represent the turbulent properties of the flow. This allows a two equation model to account for history effects like convection and diffusion of turbulent energy, two important factors of a turbulent flow.

9. After a careful analysis of Table 3.1, where it summarizes the characteristics of each turbulence model, as well as the pros and cons of each model, the RNG k-ε model and the Realizable k-ε model are the best choices for the presented study. Both the realizable and RNG models have shown substantial improvements over the standard one. The realizable k-model requires only slightly more computational effort than the standard k-model. Aside from the time per iteration, the choice of turbulence model can affect the ability of FLUENT to obtain a converged solution. The standard k-model is known to be slightly over-diffusive in certain situations, while the RNG k-model is designed such that the turbulent viscosity is reduced in response to high rates of strain. Since diffusion has a stabilizing effect on the numerical calculations, the RNG model is more likely to be susceptible to instability in steady-state solutions [91].
When making a turbulent model, many assumptions are made to reduce the computational costs of the simulation. Overall, the Realizable k-ε model is the best turbulence model to start the simulations with. The RNG k-ε model can be used in a posterior stage, to confirm the results or to perfect them after a stable convergency.

Table 3.1 - Summary-Table of all the possible turbulence models to use on this project [94, 104, 109, 110].

Turbulence Model	Turbulence Variables	Characteristics	Pros	Cons
Standard k-ε	Kinetic energy and dissipation rate	Suitable for initial iterations, initial screening of alternative designs;	Robust; Easy to implement; Computationally cheap;	Over-predict turbulence generation at locations with strong accelerations; Lack of sensitivity to adverse pressure gradients;
RNG k-ε	Kinetic energy and dissipation rate	Suitable for complex shear flows involving rapid strain, moderate swirl vortices and locally transitional flows;	Performs well with curved streamlines;	Highly sensitive which makes the convergency difficult and slow;
Realizable k-ε	Kinetic energy and dissipation rate	More adequate to simulate jet spreading and boundary layer with adverse pressure gradient	Offers largely the same benefits as RNG with easier convergency	y+ values in the first cell near the wall must not be below 30 and should not excessively exceed values of 100 because of the near wall functions
Standard k-ω	Kinetic energy and specific dissipation rate	More adequate for boundary layer flow, sensitive to free stream conditions	Superior performance for wall-bounded boundary layer	Excessive and early prediction of separation; High mesh resolution near the wall is required
SST k-ω	Kinetic energy and specific dissipation rate	Applicable for a wider range of flows than k-ω	Highly accurate	Huge computational cost; Dependency on wall distance;

4. Methodology

The ejector geometry optimization goal is to find the optimal geometry configuration which can achieve the highest entrainment ratio. The optimal configuration is obtained by investigating the influence of geometry parameters on the ejector performance for distinct operation conditions. The investigation includes adjustment of the following geometry parameters: the NXP, the length of the constant area section and the angle of the diffuser.

4.1 – Optimization Procedure

As the present work evolves, the simulation of several models to achieve the best NXP position are done. Being the simulations extremely dependent on the mesh design, it is expected a methodic mesh design work and simulations which is followed by design and optimization procedures.

In respect of the mesh optimization procedure, its goal is to find for each temperature and NXP geometry, a mesh that doesn't interfere with the simulations results (i.e. mesh independence) and permits a fast convergence. In order to optimize the mesh creation procedure and assure consistency, a mesh design procedure was developed (See Figure 4.1):
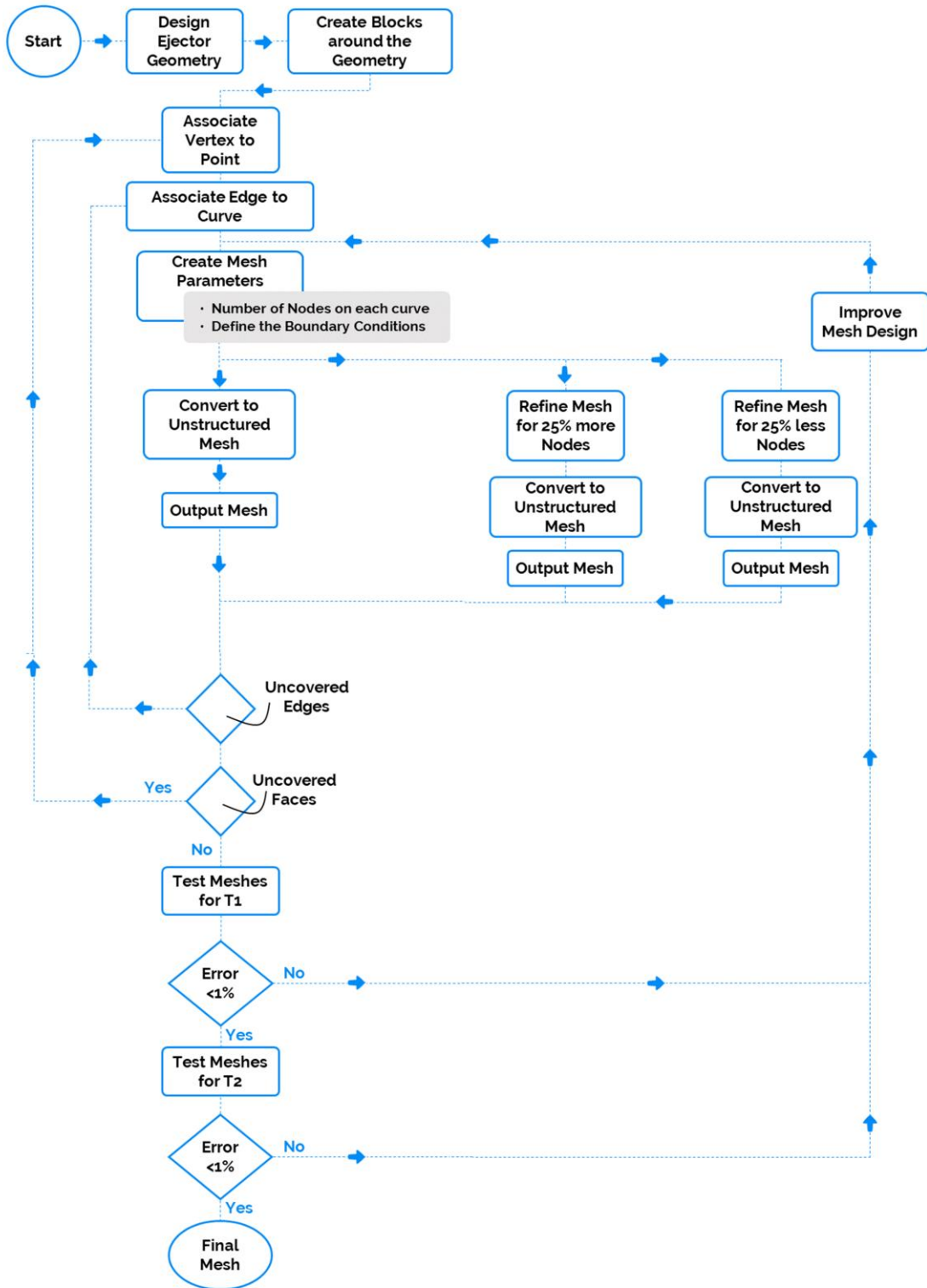
Figure 4.1 - Mesh optimization procedure

1. From a point-based geometry given by a previous stage of the SMALL-Soldes project, the general lines of the ejector are drawn.
2. The ejector is sub-divided into areas where each area is one block.
3. Each vertex of the blocks is associated with a point of the geometry.
4. Each curve of the blocks is associated with a line of the geometry.
5. Mesh parameters are created. The number of nodes on each curve are defined as well as the boundary conditions.
6. The pre-mesh is converted to an unstructured mesh.
7. A finer and a courser mesh should be created. The finer mesh should have 25% more nodes compared with the original mesh, while the courser mesh should have 25% less nodes compared with the original mesh.
8. All the three meshes need to be uncovered-faces and uncovered-edges checked, otherwise the mesh won't give consistent simulation results or won't even be able to be simulated.
9. Simulations are made for two different motive stream temperatures to check the mesh independency. If all the three meshes pass the test, a final mesh is found.

The mesh design procedure was done manually for the first few meshes to be confirmed independent from the simulation. After that, many meshes were made changing some geometry parameters using journal files and a python script (See Appendix A.2).
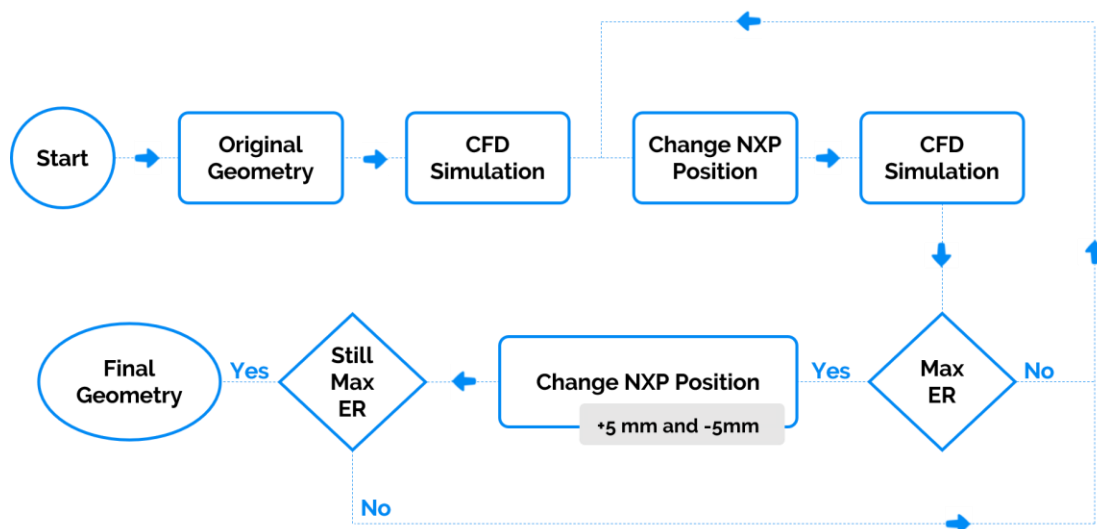
Figure 4.2 – Simulation's optimization procedure.

Figure 4.2 illustrates the simulation's optimization procedure. The procedure was followed for seven simulated temperatures on the ejector. The steam generator was calculated to run from 130ºC and 180ºC and the collector output with temperatures from 120ºC to 170ºC. Thus, 120ºC - 180ºC with a temperature step of 10ºC was the chosen working-range temperatures of the ejector. The optimization procedure is described below:

1. From a base-case design (Figure 4.3), a CFD simulation is done for a given motive flow temperature.
2. For a given flow, the NXP position is changed (upstream or downstream) 10mm in order to understand if, for the motive stream temperature to be simulated, the flow exiting the nozzle is over-expanded or under-expanded. If under-expanded, moving the NXP upstream will increase the ER, whereas moving the NXP downstream in an over-expanded flow will increase the ER.
3. After a few simulations, when reaching the maximum ER, there is a need to do a new round of simulations with the NXP 5mm upstream and 5mm downstream of the best-case ER to confirm, within 5mm error, the best NXP position for each temperature.

The simulation's optimization procedure was done manually by changing the mesh to be tested until achieving the optimum ER on all three designs. An additional forth mesh design was tested to confirm the behaviour of the tests.

4.2 – Mesh Design

One of the most important CFD simulation preprocessing is the discretization of the domain of interest, i.e. mesh generation. Thus one of the most time consuming tasks of this work. ICEM-CFD software was used to create it. There are a lot of numerical errors that are introduced in CFD due to mesh size.

Sometimes there are mesh elements where nothing particularly interesting is happening in the fluid, and not enough mesh cells where a vortex is going on. An obvious solution would be to make a super-fine mesh that can capture everything in the domain perfectly.

However, this is not computationally efficient, nor is it even possible. Furthermore, there's a relationship between the size of your mesh and how well the

solution converges (coarse mesh usually leads to better convergence, fine mesh usually leads to divergence). Iteration must be used to determine the ideal mesh.

4.2.1 – Geometry

A mesh was mapped to the model geometry using grid-generating software (ICEM-CFD) from a previously calculated 1-D mathematical model [121]. Figure 4.3 is the result of connecting the dots given by the 1-D model showing the ejector dimensions. The original geometry has the constant area-section length of seven times the constant area-section diameter.
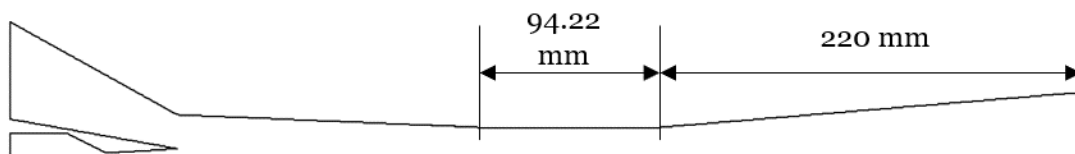
Figure 4.3 - Original mesh geometry.

Two additional geometries were created to simulate an ejector with bigger constant area-section length and an ejector with a smaller angle of the diffuser in order to tackle problems from simulations with the first geometry. More information about the causes of the problems and their solution are presented in the next sub-chapters.

Each new geometry had the exact same geometry of the original model with one modification each (bigger constant area-section length and smaller diffuser angle, respectively).

On the ejector with bigger constant area-section length, two geometries were created. The first one has a length of twelve times the constant area-section diameter (see Figure 4.4) and the second one has a length of nine times the constant area-section diameter.
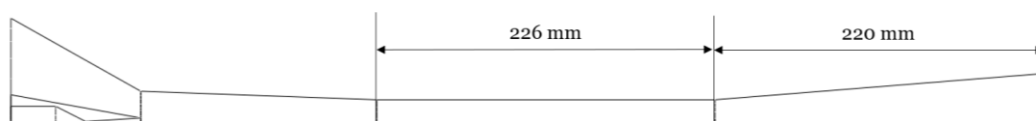
Figure 4.4 - Constant area section change geometry.

The second new geometry type created had half of the diffuser angle as the original model, thus it had more than double the diffuser length of the original model as seen in Figure 4.5.
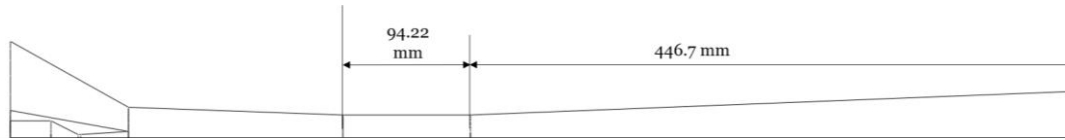
Figure 4.5 - Diffuser angle change geometry.

Each geometry type required a mesh for each NXP. In total, thirty-four different meshes, with proportional number of nodes to follow the original mesh independence study, were designed to simulate every NXP for all four different geometries.

For each geometry, NXP geometry was designed manually twice, one 10 millimeters to the left and one 10 millimeters to the right with a report file recording every movement. Other meshes were replicated using the report script and changing the position to which the NXP would be tested. The report script had the help of a python script that interpolated the wall distance to the NXP in order to create a new block on that area on ICEM-CFD. Both reports are available in Appendix A.2.

4.2.2 – Mesh Boundary Conditions

Boundary conditions of the two flows which entering the primary nozzle and the ejector were set as pressure-inlets, while the one leaving the ejector was set as pressure-outlet.

The same boundary conditions were set up for all three ejector geometries configuration. To set boundary conditions in relative pressure. Also, gravity was discarded.

Table 4.1 enumerates the several boundary conditions created for each geometry and Figure 4.6 gives an image on where these boundary conditions were applied on the geometry.

Table 4.1 - Boundary conditions in respect of Figure 4.6.

Figure 4.6 no.	Boundary	Boundary Condition
11	Motive-stream inlet	Pressure-Inlet
10	Secondary-stream inlet	Pressure-Inlet
12	Outlet	Pressure-Outlet
1, 2, 3, 4, 5, 6	Axis	Axis
6, 7, 8, 9	Wall	Wall
15, 13, 14	Interior	Interior
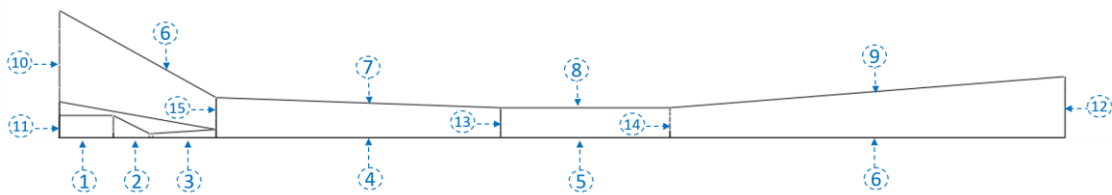
Figure 4.6 - Mesh geometry with pointed boundary conditions.

Until reaching mesh independency and having a final mesh that could run the simulations without major divergencies, 56 meshes were created.

Boundary conditions and the mesh design on the wall was found to be of utmost importance to reach mesh independency and to run the simulations smoothly without divergencies.
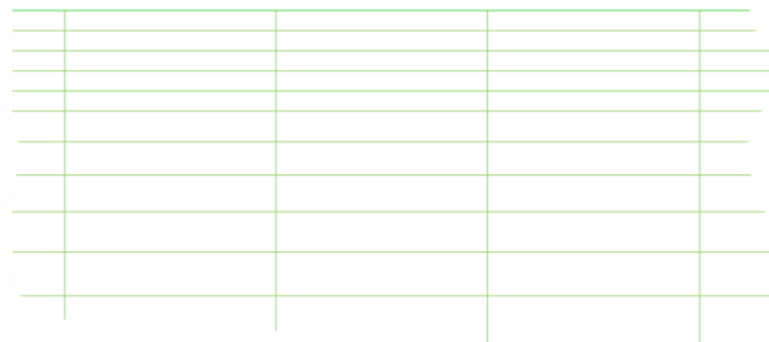
Figure 4.7 - Poorly designed near-wall mesh.

Figure 4.7 shows a poorly designed mesh near the wall. The cells are too stretched and do not have small enough length near the wall to have a good perception of the y+ values.

A good indicator on how coarse or fine a mesh is for a particular flow pattern is the y+ value. y+ is a non-dimensional distance. It is important in turbulence modeling to determine the proper size of the cells near domain walls. y+ is a ratio between turbulent and laminar influences in a cell, if y+ is big then the cell is turbulent, if it is small, the flow at the cell is laminar [122].

The importance in many cases of this concerns wall functions which assume that the laminar sub-layer is within the first cell, if Y+ is small then the cell is totally laminar and the next cell in has some laminar flow in it [123], the wall functions are not applied to this cell and you make bad modelling assumptions.
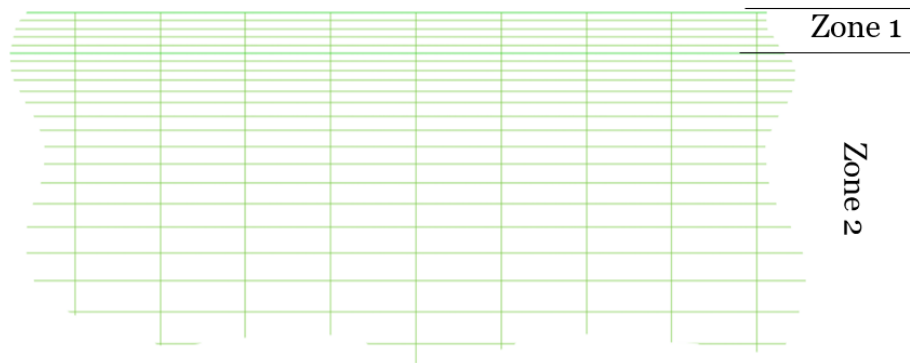
Figure 4.8 - Quality design near-wall mesh.

Figure 4.8 depicts a quality near-wall mesh design. Two different zones were created. A first zone with all the cells with, very small, same vertical length for a better calculation of the y+ parameter. The second zone has the same vertical length of the first one on its most near cell to the wall, after that, there is a small growth ratio that makes sure the cells grow smoothly for a better simulation convergency.

4.2.3 – Mesh Independence

The grid size is examined by creating two new different grid-size models (coarser and finer). Both models were simulated with the same conditions as the original model for two different motive-stream temperatures. The results using the finer grid size are considered to be the most reliable; however, it comes more computational time and memory.

The preferred simulation model takes the least computational time yet provides accurate results. Once identified, it was applied throughout the study. On this study, the grid size and number of iterations were carefully selected to give valid results.

Grid independence was studied in order to investigate the effect of the mesh size and design on the results. Thirty four were constructed and tested.

This study concluded that the number of finite volumes were not the only parameter to be considered on the mesh independence but also the design of the mesh as shown in Figure 4.7 and Figure 4.8.

On this study, a mesh is considered independent if the entrainment ratio results difference of the simulation (primary and secondary flow) on the original mesh is 1% or below the results of both the courser and the finer mesh. Table 4.2 and Table 4.3 show the chosen mesh simulation results on the three models for motive flow temperatures of 130°C and 140°C, respectively.

The original mesh (~150 000 finite volumes) was found to provide grid independent ejector performance indicators as shown in Table 4.2 and Table 4.3.

Table 4.2 - Mesh independence tests for a motive flow of 130°C.

	Mesh	Outlet [g/s]	Primary Inlet[g/s]	Secondary Inlet [g/s]	ER (%)
130°C	Original	-11.48	5.3043	6.1709	116.3366
	Courser	-11.46	5.3077	6.1544	115.9525
	Error (%)	0.1142	0.0629	0.2675	0.3302
	Finer	-11.46	5.3076	6.1516	115.9017
	Error (%)	0.1387	0.0613	0.3128	0.3738

Table 4.3 - Mesh independence tests for a motive flow of 140ºC.

	Mesh	Outlet [g/s]	Primary Inlet [g/s]	Secondary Inlet [g/s]	ER (%)
140ºC	Original	-13.66	7.1312	6.5290	91.5571
	Courser	-13.68	7.1518	6.5480	91.4348
	Error (%)	0.1234	0.4297	0.2956	0.1335
	Finer	-13.67	7.1317	6.5350	91.5808
	Error (%)	-0.0137	0.0071	0.0065	0.0259

Although the number of nodes on the mesh could be reduced to improve computing time and still maintaining the mesh independency, simulations with higher temperatures (e.g 180ºC motive flow) require higher cell density in some areas for a faster convergency, as well as the mesh being used for different geometries, influenced the over-densification of the mesh.

As the original mesh was tested and confirmed its independency, meshes with different geometries (different NXP, larger constant area section or different diffuser angle) would also keep the mesh independency if the number of nodes on the changed regions kept the same ratio of nodes per mm of the curve to be changed.

4.3 – CFD Analysis

The ejector geometries shown in Figure 4.3, Figure 4.4 and Figure 4.5 were applied in this study. A number of cases with different motive-stream temperatures were simulated. The model simulated several motive-stream temperatures summarized in Table 4.7. Table 4.6 summarizes the specified values on the inlets and outlet for each temperature in the CFD model. The mass flow rate of both the inlets and outlet is reported and plotted.

The only reasonable simplifying assumption made was considering the model to be axisymmetric. In a 2D axisymmetric the circumferential derivatives of flow variables (pressure and velocity) are zero. As the ejector's geometry is symmetric, a 2D axis-symmetric model was chosen.

The fluid flow was set as steady state. The solver pressure-based was selected because it can obtain comparable results with the density-based one, while it is much more stable and solution converges faster [40, 124]. Based on these previous studies, Table 4.4 values and parameters were selected on ANSYS Fluent.

Table 4.4 - Parameters selected for the model solver.

Type	Parameter Selected
Solver	
Model Type	Pressure-Based
2D Space	Two-dimensional axis-symmetric model
Time	Steady
Velocity formulation	Absolute
Operating Pressure (Pa)	101325
Gravity	No

Due to the fact that the flow inside the ejector was thought to be in a supersonic flow field, most of the time it is assumed to correspond to turbulent compressible flow [125]. For the wall it was applied the standard wall function, that is, the no-slip condition.

Based on Chapter 3 turbulence methods study, values were selected accordingly. The values and parameters are described in Table 4.5.

The parameters that are not mentioned on the tables above were set with the default values.

Table 4.5 - Parameters selected for the energy equation and turbulence model.

Type	Parameter Selected
Energy Equation	Yes
Turbulence Model	Realizable k-epsilon Model
Viscous Heating	Yes
Compressibility Effects	Yes

In order to solve the governing equations, proper boundary conditions must be set.

The Boundary Condition (BC) setup in FLUENT is illustrated in Table 4.6. Boundary conditions were obtained based on a property database (EES) file that related the hydraulic diameter of the inlets and the outlet, the outlet (condenser) temperature and the secondary stream flow temperature. Temperatures on the outlet and on the secondary inlet were provided and were directly applied as BCs. This is a reasonable option when the transport losses between the ejector outlet and the condenser are assumed to be negligible [110].

The turbulence length scale was calculated based on the hydraulic radius of both the inlets and outlet, while the turbulent intensity was selected based on previous researches [110].

Table 4.6 - Parameters selected for the boundary conditions.

Boundary Conditions	Parameter Selected
Primary Inlet	
Pressure, Temperature	See Table 4.7
Turbulence Intensity (%)	5
Turbulence Length Scale (m)	0.00174
Secondary Inlet	
Pressure (kPa)	5.356
Temperature (K)	34.11
Turbulence Intensity (%)	5
Turbulence Length Scale (m)	0.0099
Outlet	
Pressure (kPa)	9.105
Temperature (K)	337.15
Turbulence Intensity (%)	10
Turbulence Length Scale (m)	0.00475

Primary inlet temperatures were considered in a range that would be suitable for a TVC application. This would require a wide range of generator temperatures (120-180 ºC). In this work, 10ºC variation step was applied. The values of the primary inlet boundary conditions were set as the saturated properties of each operating state. Primary inlet pressures were set on a relative basis, and two pressure values were defined (Total Pressure and initial Supersonic Pressure) as seen in Table 4.7.

Table 4.7 - Parameters selected for the primary inlet.

Temperature (ºC)	Primary Inlet		
	T(K)	Total_P(kPa)	SuperSonic_P(kPa)
120	393.15	42.1	40.0
130	403.15	97.16	90.0
140	413.15	168.7	160.0
150	423.15	259.9	250.0
160	433.15	374.4	370.0
170	443.15	516.3	510.0
180	453.15	690.1	690.0

As seen in Table 4.8, the simulations were carried out using water-vapor as the fluid and the flow is governed by an ideal gas compressible steady-state form of the conservation equation. Water-vapor was assumed to be an ideal gas because the steam ejector was operating at low absolute pressure inside the mixing chamber. Other studies proved to be an acceptable assumption [124].

Table 4.8 - Parameters selected for fluid characterization.

Type	Parameter Selected
Fluid	
Fluent Fluid Material	Water-Vapor (H_2O)
Density	Ideal-Gas
Specific Heat (Cp)	Constant – 1860 j/kg-k
Thermal Conductivity	Constant – 0.0261
Viscosity	Power-law

72

For accuracy QUICK method was used for pressure, momentum and the turbulence viscosity discretization, while second order upwind method was used for turbulence kinetic energy and turbulence dissipation rate discretization. The discretization system was solved by using the coupled solver, as seen in Table 4.9.

Table 4.9 - Discretization parameters selected on Fluent.

Type	Parameter Selected
Discretization Technique	Finite Volumes
Discretization Scheme	Coupled
Gradient	Least Squares Cell Based
Pressure	Second Order
Density	QUICK
Momentum	QUICK
Turbulence kinetic Energy	Second Order Upwind
Turbulence Dissipation Rate	Second Order Upwind
Energy	QUICK

For each simulations, the solution was obtained in only one step, i.e. keeping the simulation running with the same discretization parameters from beginning to end, justifying the choice for the realizable k-ε model. Final convergence was obtained in every simulation. Iterations were performed until the following criteria were satisfied. The relative residuals for all flow variables were ≤ 10E-5, the mass fluxes across each face in the calculation domain were stable (minimum of 500 iterations with the same value) and the mass flow rate error was under 10E-6.

The evaluation of the mass flow rate entering the primary nozzle (primary mass flow rate), leaving the evaporator to the mixing chamber (secondary mass flow rate) and leaving the ejector (outlet mass flow rate) were introduced as external reports to calculate the entrainment ratio and the mass flow rate error.

5. Results and Discussion

The results are presented and conclusions are drawn for all necessary and interesting cases.

On this section, the L represents the variation of the NXP, taking the zero value as reference from the original NXP for the first geometry. A negative L means that the NXP is moved upstream and a positive one means that the nozzle was moved downstream. For a better understanding of how the NXP can affect the entrainment ratio, a new kind of plots were made. A better explanation about how the plots were made and how to read them is given at Appendix A.2.

5.1 – Adjusting only the NXP

Adjusting the NXP through different motive flow temperatures lets the flow develop with ideal size of the jet effective area.

5.1.1 – Motive Flow of 120ºC

The simulation results for motive flow temperature of 120ºC are shown in Figure 5.1. The ER, is plotted with the value of L. It can be observed that the ideal NXP for that case is 40 millimeters downwind of the original NXP with a maximum E.R of 43.87%.
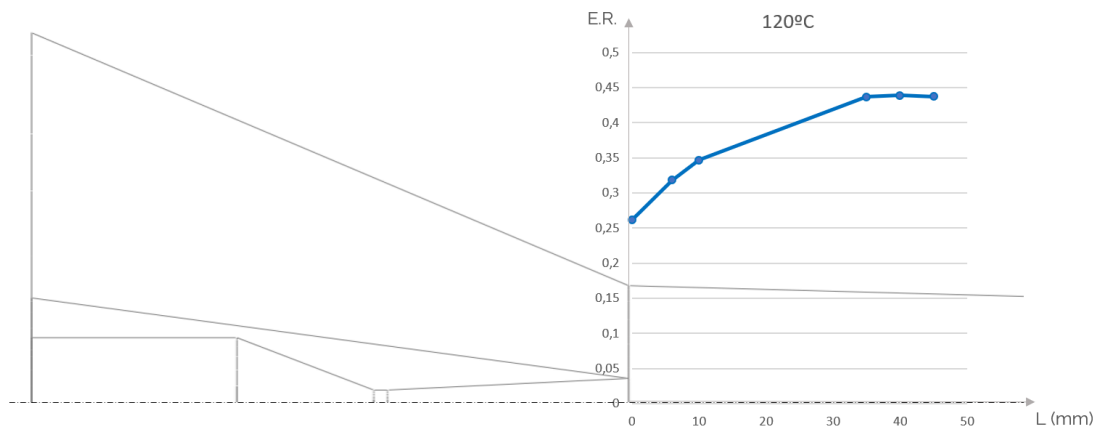
Figure 5.1 - Ejector Performance with different NXP for 120ºC.

However, the ER is very low compared to expected results, i.e. the ejector was designed for a motive flow temperature of 120ºC, therefore with expected entrainment ratio above 1. At a motive flow temperature of 120ºC, the entrainment ratio should be at its maximum since the EES model calculated the original geometry based on that motive flow temperature.

This inconsistency with the expected results is due to the fact that the realizable k-ε model tends to underpredict the critical pressure value [110]. If the CFD model underpredicts the critical backpressure value (calculated at −92.2 kPa relative pressure), the entrainment ratio value will be much lower than the real value.

The phenomena is well explained with a critical backpressure-entrainment ratio plot. As shown in Figure 5.2, the critical backpressure predicted by Fluent is lower than

the one predicted by the EES script, therefore, the original simulation (with backpressure of 92.2 kPa), as the value for the outlet backpressure is constant on both ANSYS Fluent and EES, was misleading ANSYS Fluent to a much lower entrainment ratio.

On the other hand, bigger motive flow temperatures will not have the same problem since all the simulation were done at the same backpressure. As shown in Figure 2.14 of page 32, backpressure values, i.e. pressure value at the ejector's outlet, tend to increase with the increase of the temperature. Keeping the same value of backpressure for all simulations, being at the left side (with a smaller backpressure) of the critical point is always assured.
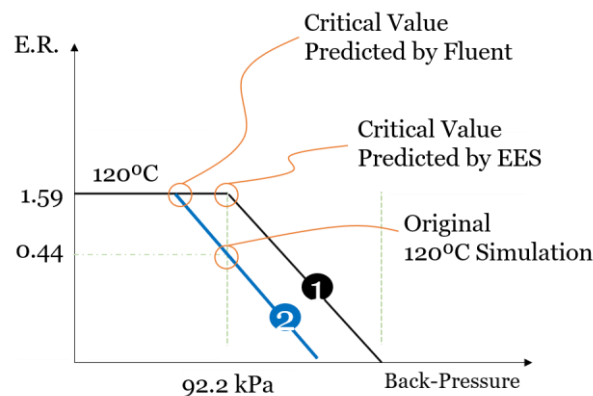
Figure 5.2 - Back-Pressure - E.R. plot comparison with two different critical Back-Pressure.

As a decrease of backpressure below the critical backpressure values will not affect the entrainment ratio values (since the motive pressure and entrained pressure keep constant), new simulations with reduction of the backpressure were done to confirm the motive flow temperature of 120⁰C case and to find the optimum NXP and entrainment ratio. The results are presented in Figure 5.3

Figure 5.3 compares the entrainment ratio on both backpressure cases. With a smaller backpressure, the entrainment ratio increased significantly, corroborating the theory presented above.
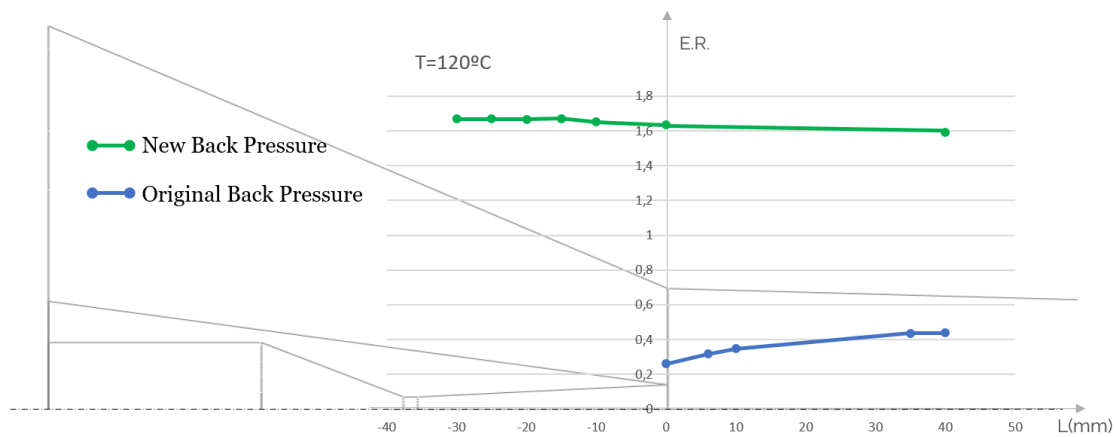
Figure 5.3 - Ejector Performance with different NXP and back Pressures for 120ºC.

Moreover, the optimum NXP moved from L=40 (ER = 43.87%) with the original backpressure to L=-25 (ER = 167%) with the new backpressure. The reason for this up-winding of the ideal NXP for the new backpressure lays with the fact that with smaller backpressure the flow exiting the nozzle becomes under-expanded and therefore the effective area of each flow will vary. The effective area, as explained in page 26, is the main responsible for a bigger or smaller entrainment ratio.

Thus, as the motive flow properties exiting the nozzle is independent of the NXP, moving the NXP upstream will shorten the length of the jet core and the wall of the constant pressure-section.
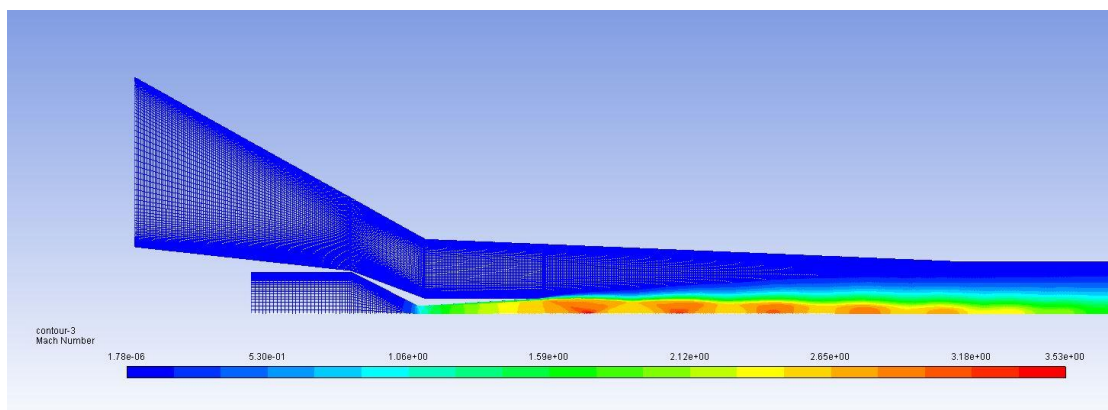
Figure 5.4 - Mach-Number pathlines of 120ºC with original backpressure; L=40.

As seen in Figure 5.4, on a single chocking flow, because of its low velocity and low pressure (only the primary flow reached sonic conditions), it is beneficial until reaching the optimum position (in this case, L=40 mm).

However, in Figure 5.5, the primary flow is expanding and entraining the secondary one until both flows reach the sonic speed. Moving the nozzle upwind will give the flow more space to entrain the secondary flow and not chocking it, therefore keeping an optimum effective area on entrainment.
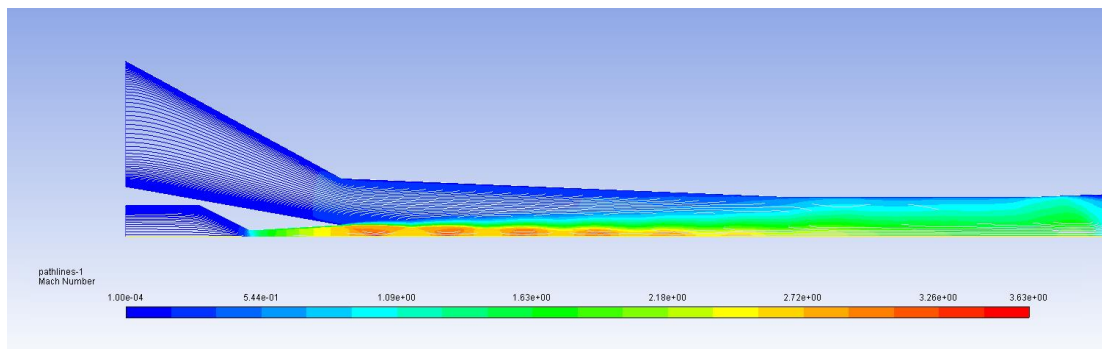
Figure 5.5 - Mach-Number pathlines of 120ºC with new back pressure; L=-25.

5.1.2 – Motive Flow of 130ºC

The simulation results for motive flow temperature of 130ºC are shown in Figure 5.6. The entrainment ratio, ER, is plotted with the value of L. It can be observed that the ideal NXP for that case is 25 millimeters upwind of the original NXP, with a maximum ER of 119.59%. This phenomenon is consistent with the expected results.
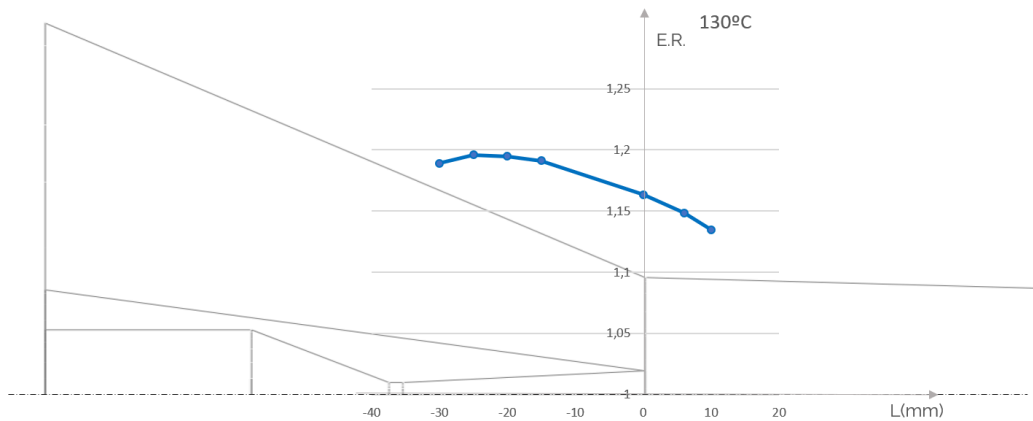
Figure 5.6 - Ejector Performance with different NXP for 130ºC.

As the flow exiting the nozzle is under-expanded, it is expected that the optimum NXP is located upstream of the original NXP. The results confirm it. Thus, moving the NXP upstream leads to a bigger distance of the jet-core and the wall, letting more secondary flow to be entrained as shown in Figure 5.8.

Moreover, comparing Figure 5.7 and Figure 5.8, it is possible to see a bigger fluctuation of the jet bellow with L=0 compared to a NXP of L=-25. This can be related with the effectiveness of the relation between the jet-core and the effective-area.

Figure 5.7 - Mach-Number Color-Map of 130ºC with L=0.

Again, the effective area has an optimum point, and having the NXP moving downstream more than 25 millimeters will affect the entrainment ratio as shown in Figure 5.6. This may be because after the optimum point, the flow do not have the velocity nor the pressure needed to entrain the secondary flow with bigger distances from the jet-core to the wall as well as the 25 millimeter upstream does.
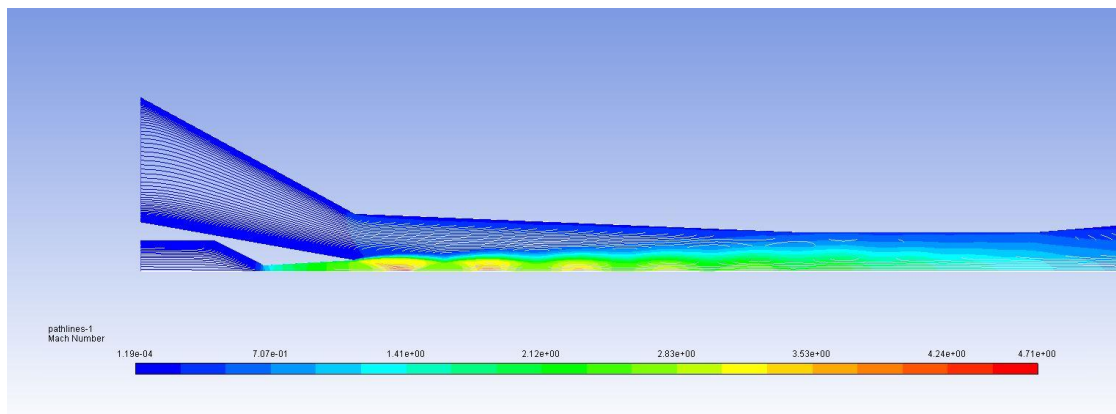
Figure 5.8 - Mach-Number Color-Map of 130ºC with L=-25.

5.1.3 – Motive Flow of 140ºC

The simulation results for motive flow temperature of 140ºC are shown in Figure 5.9. The entrainment ratio, ER, is plotted with the value of L. It can be observed that the ideal NXP for that case is 15 millimeters upwind of the original NXP, with a maximum E.R. of 94.55%. This phenomenon is consistent with the expected results.
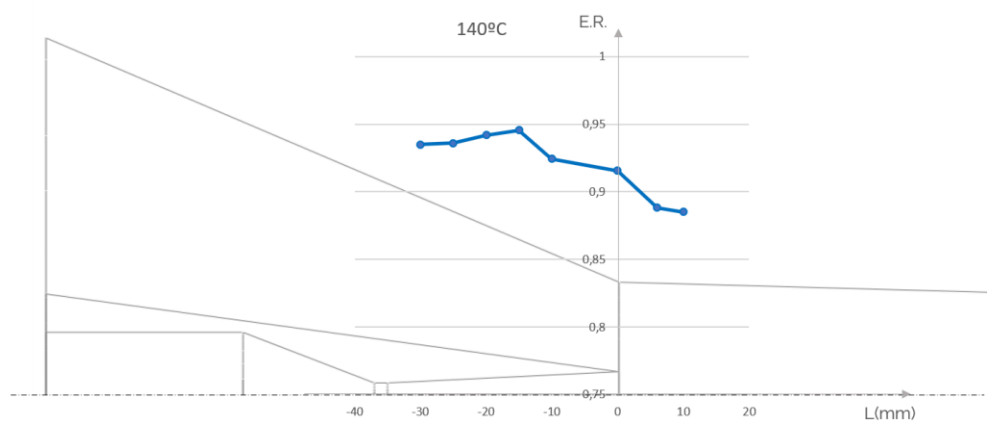
Figure 5.9 - Ejector Performance with different NXP for 140ºC.

Figure 5.10 and Figure 5.11 gives a clear image of why moving the NXP upstream improves the entrainment ratio. While on Figure 5.10 (L=0) the effective area of mixing gets narrowed until reaching a constrained flow on the constant area section, moving the NXP downstream, as in Figure 5.11 (L=-15), gives more space to the effective area, responsible for a bigger mixing between the two streams.
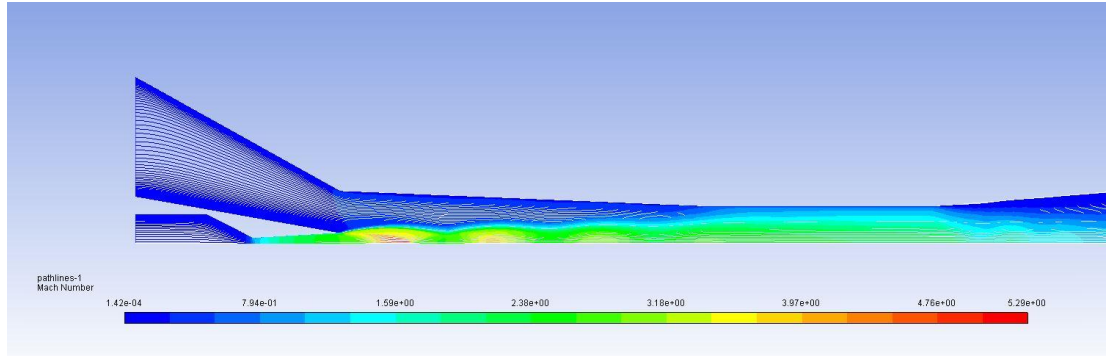
Figure 5.10 - Mach-Number pathlines of 140ºC with L=0.

When the pressure is increased, a smaller effective area is available. Therefore, less amount of the secondary flow is drawn to the mixing chamber while also increasing the primary flow rate.

This is the main reason to why there should be a down winding of the NXP in temperatures to which the flow exits the nozzle under-expanded.
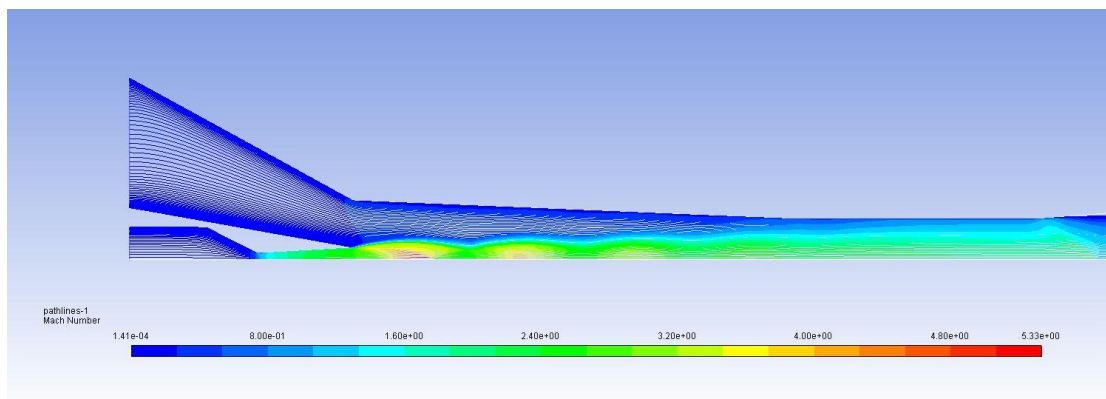
Figure 5.11 - Mach-Number pathlines of 140ºC with L=-15.

5.1.4 – Motive Flow of 150ºC

The simulation results for motive flow temperature of 150ºC are shown in Figure 5.12. The entrainment ratio, ER, is plotted with the value of L. It can be observed that the ideal NXP for that case is 30 millimeters upwind of the original NXP, with a maximum ER of 77.04%. This phenomena is consistent with the expected results.
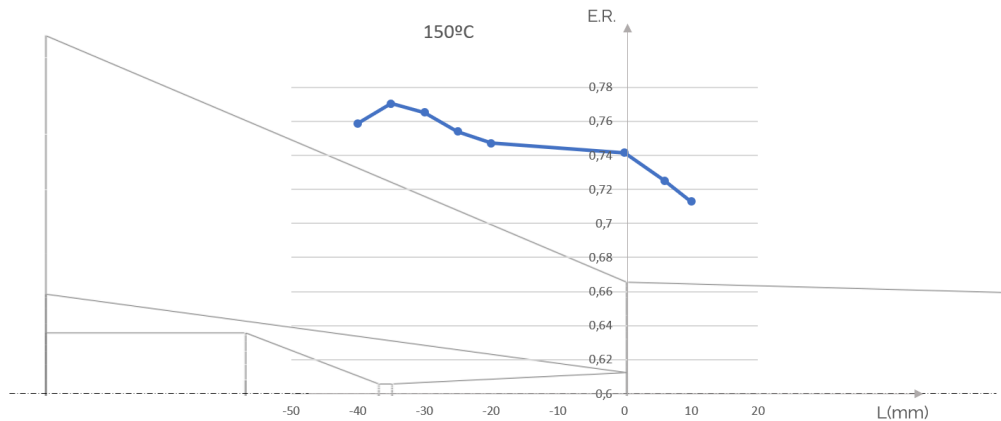
Figure 5.12 - Ejector Performance with different NXP for 150ºC.

With the motive flow temperature of 150ºC the improvement of entrainment ratio with the up-winding of the NXP happens because the effective area of mixing gets narrowed until reaching a constrained flow on the constant area section, moving the NXP upstream, as in Figure 5.14 (L=-35) in comparison with Figure 5.13 (L=0), gives more space to the effective area, responsible for a bigger mixing between the two streams.
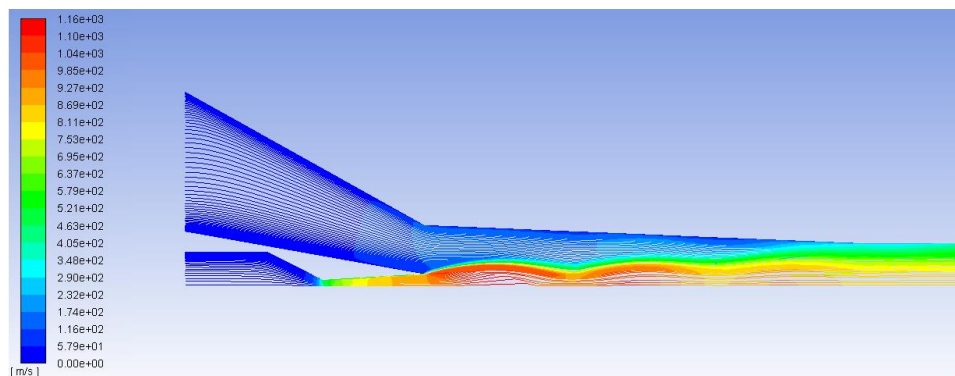
Figure 5.13 - Mach-Number pathlines of 150ºC with L=-0.
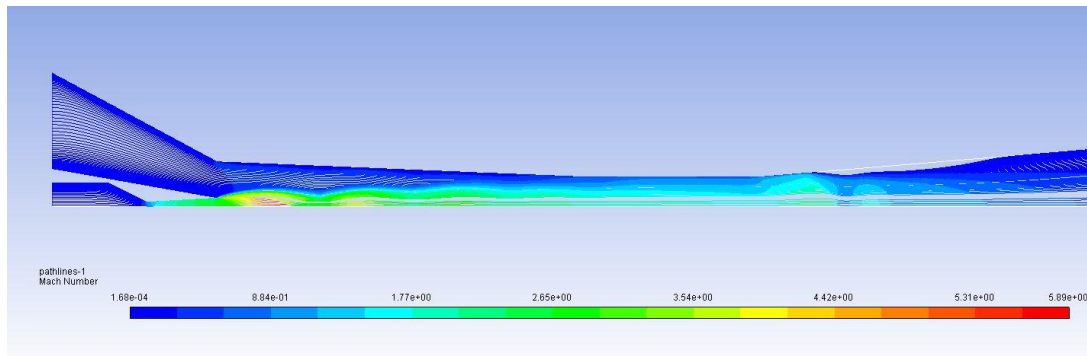
Figure 5.14 - Mach-Number pathlines of 150ºC with L=-35.

However, a new phenomenon appears. A recirculation zone is created at the beginning of the diffuser section. Taking a look at the NXP of 20 millimeters upwind (Figure 5.15) is possible to understand that even though it may have a more optimized effective area section and also a bigger maximum Mach-number compared with a NXP of 35 millimeters downwind, the entrainment ratio is bigger on the second case.
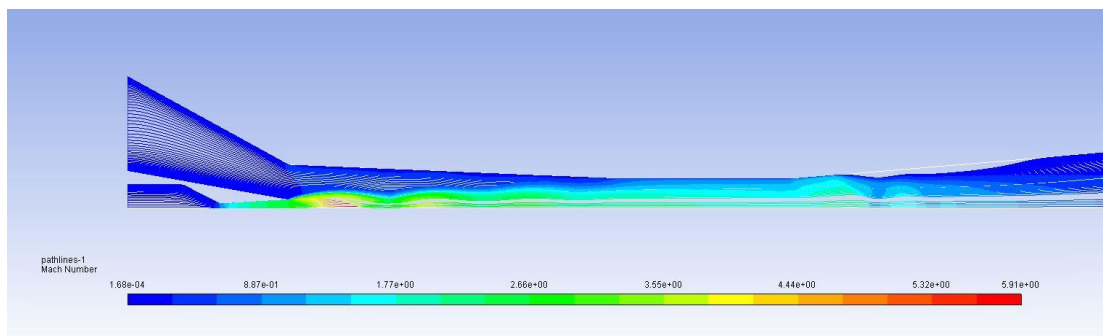
Figure 5.15 - Mach-Number pathlines of 150ºC with L=-20.

Figure 5.16 and Figure 5.17, L=-20 and L=-35 respectively, prove that at the motive flow temperatures of 150ºC the recirculation starts to affect the entrainment ratio. For L=-35 case, the recirculation is 11.13% smaller compared with the L=-20 case. As the flow on the diffuser is already sub-sonic, this has an impact on the flow upstream, thus, the entrainment ratio.
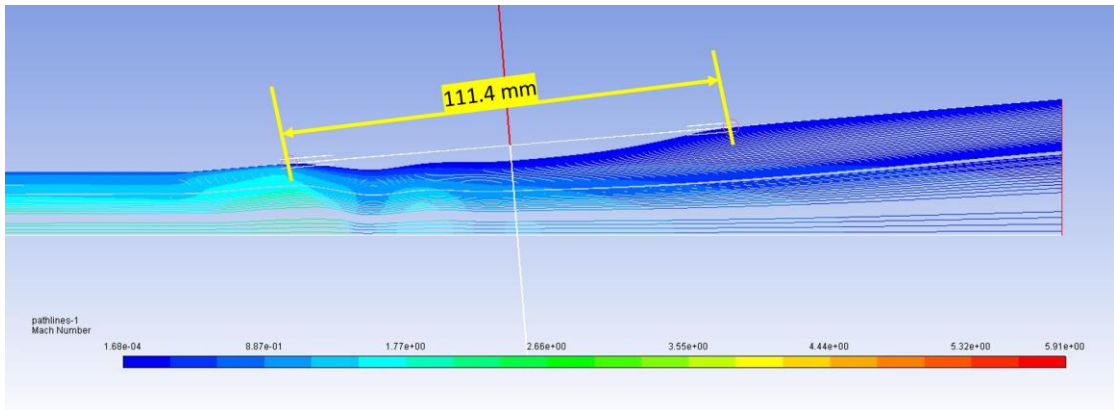
Figure 5.16 - Diffuser focused Mach-Number pathlines of 150ᵒC with L=-20.
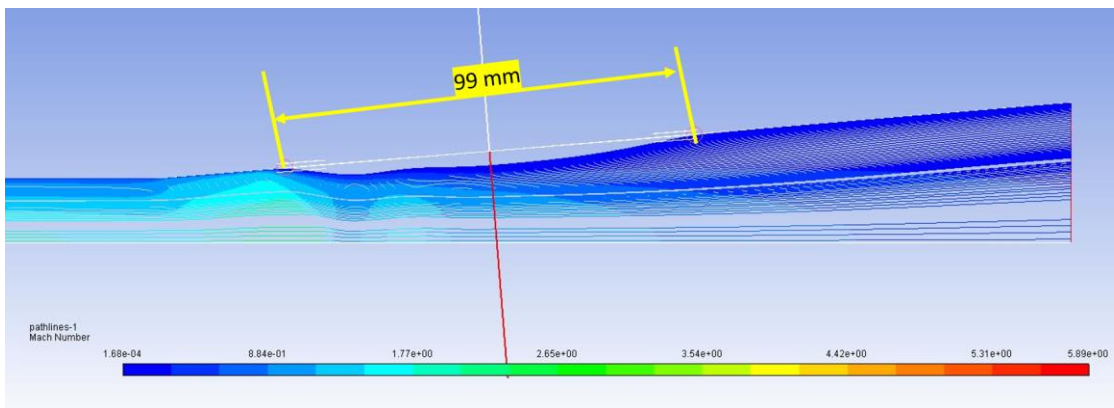
Figure 5.17 - Diffuser focused Mach-Number pathlines of 150ᵒC with L=-35.

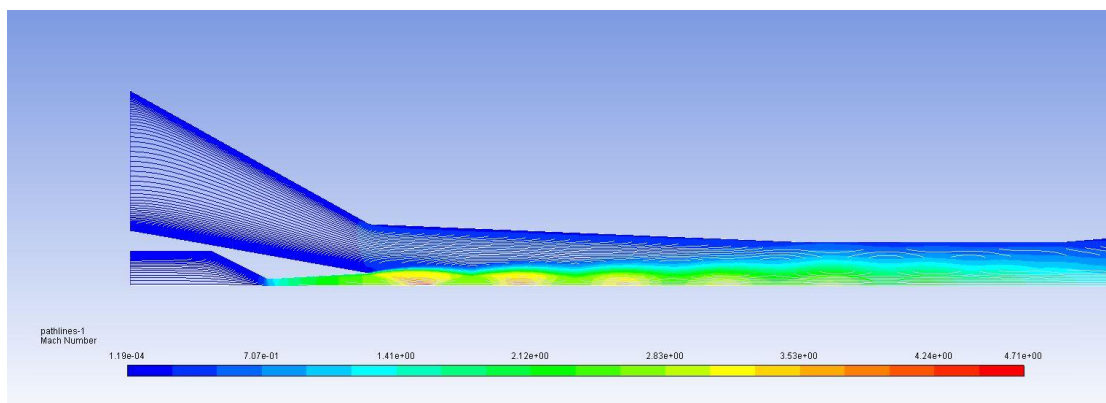## 5.1.5 – Motive Flow of 160ºC, 170ºC and 180ºC

The simulation results for motive flow temperature of 160ºC, 170ºC and 180ºC are shown in Figure 5.18. The entrainment ratio, ER, is plotted with the value of L. It can be observed that the ideal NXP for these cases are 20 millimeters upwind of the original NXP, with maximum ER of 65%, 30 millimeters upwind with maximum ER of 51% and 30 millimeters upwind with maximum ER of 38% for the motive flow temperature of 160ºC, 170ºC and 180ºC, respectively. This phenomenon is consistent with the expected results.
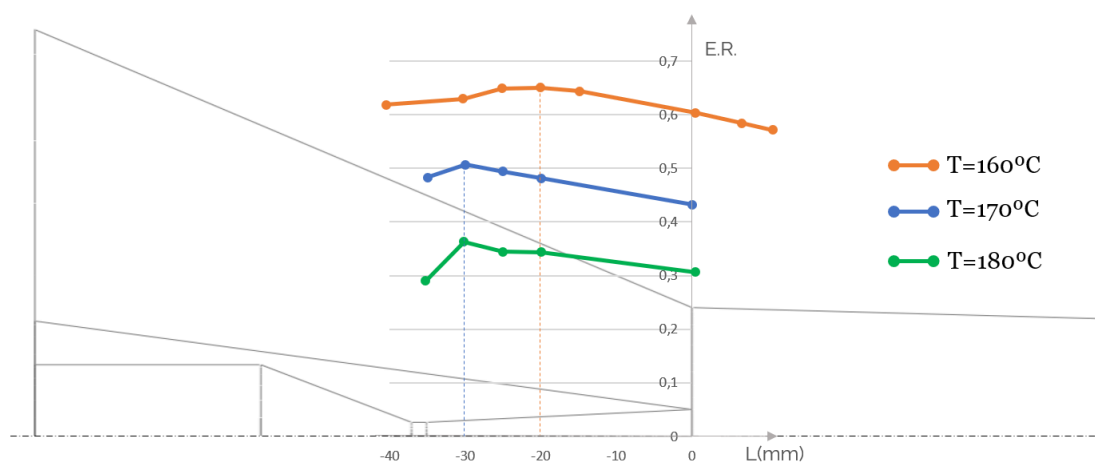
Figure 5.18 - Ejector Performance with different NXP for 160ºC, 170ºC and 180ºC.

The reason for the up-winding of the NXP is the same as explained previously when simulated the motive flow of 150ºC and are shown in page 81.

At these motive flow temperatures, recirculation continue to happen and is getting bigger with the increase of the temperature.

Table 5.1 - Mass flow rate comparison on the optimum geometry for motive flow of 170ºC and 180ºC.

T(ºC)	Outlet MFR [g/s]	Primary Inlet M.F.R. [g/s]	Secondary Inlet M.F.R. [g/s]	ER (%)
170	-23.8077	15.7550	7.9848	50.6808
180	-27.4997	19.9694	7.5926	38.0214

The Mass Flow Rate (MFR) which the optimum NXP geometry for a motive flow temperature of 170ºC and 180ºC happens are described on Table 5.1. Even though a motive flow of 180ºC comes inherently with higher speed compared with a 170ºC motive flow stream, the 180ºC case will entrain less secondary flow.

5.1.6 – Results Overview

Table 5.2 gives an overview of all forty-four simulations done for the first geometry. The results are colored based on a colormap. Closer colors mean that the results are closer. It is possible to see that the entrainment ratio changes are higher when changing the motive flow temperature than when changing the NXP.

Table 5.2 - Entrainment ratio results of the simulations on the first geometry.

NXP	120	130	140	150	160	170	180
40	163.4%						
10		113.5%	88.5%	71.3%	57.8%		
6		114.9%	88.8%	72.5%	59.0%		
0	163.4%	116.3%	91.6%	74.2%	60.9%	43.2%	32.7%
-10	165.1%		92.4%				
-15	167.1%	119.1%	94.5%		64.6%		
-20	166.6%	119.5%	94.2%	74.7%	65.3%	48.2%	36.2%
-25	166.8%	119.6%	93.6%	75.4%	65.2%	49.4%	36.2%
-30	166.8%	118.9%	93.5%	76.5%	63.3%	50.7%	38.0%
-35				77.0%		48.3%	31.1%
-40				75.9%	62.3%		
Best	167.1%	119.6%	94.5%	77.0%	65.3%	50.7%	38.0%
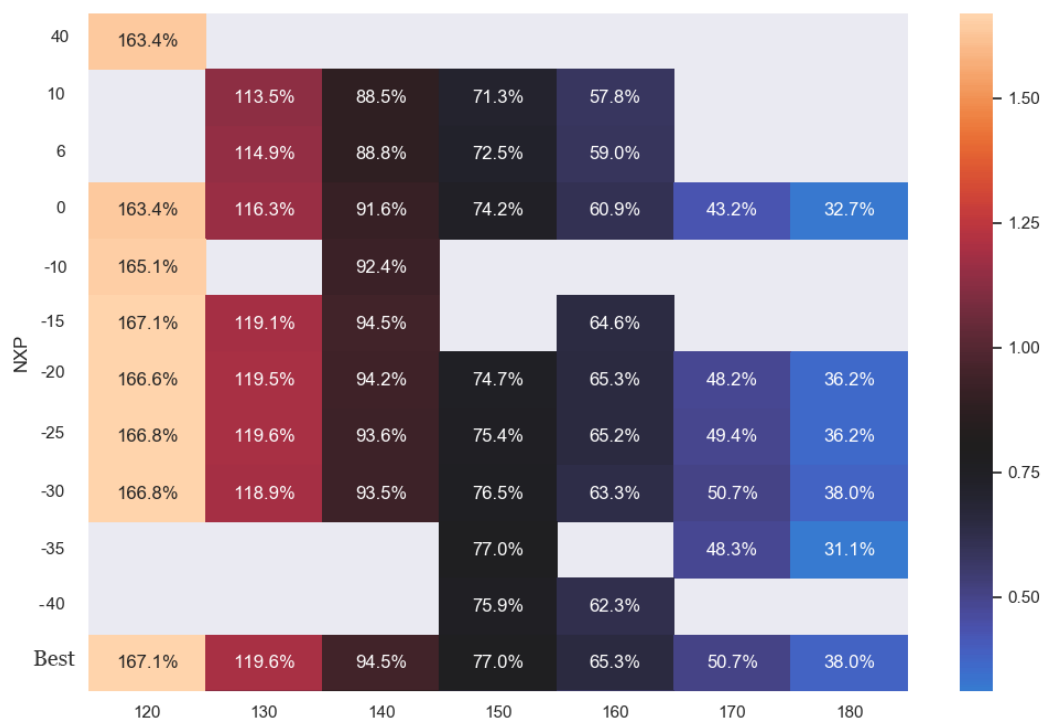
Table 5.2 shows a noticeable a decrease tendency of the ER values with the motive flow temperature increase. Moreover, the results showed that every flow simulated exiting the nozzle were under-expanded, thus the optimum NXP was located upstream from the original NXP as expected. The highest values of entrainment ratio happened for a motive flow temperature of 120ºC, as expected, since the ejector was designed to perform at this temperature.

5.2 – Adjusting the NXP while increased the constant area section length

After simulating a first geometry and finding the optimum NXP for every temperature it was found that recirculation zones can have an important role on the entrainment ratio at high temperatures (150-180ºC). A possible solution is to increase the constant area section to prevent the recirculation appearance on the diffuser since the flow on previous simulations reached the diffuser on supersonic state, thus not taking full advantage of the diffuser. This section describes the study that was made and its results.

After a careful analysis for every motive flow temperature on the original geometry, and since the flow behaves similarly for each motive flow temperature, only motive flow temperatures in which some non-identical phenomenon compared with the first geometry happen will be studied on detail for the second geometry.

5.2.1 – Motive Flow of 130ºC and the shock wave

The lowest motive flow temperature to be tested was 130ºC. Since the increase of the constant area section was made to tackle recirculation problem on the diffuser section, there was no need to test a case where the flow conditions were so far from the ones which recirculation zones are created.

The simulations on the second geometry, at a motive flow temperature of 130ºC, gave interesting and unexpected results. Unlike the previous simulations for the same temperature, the optimum NXP is located downwind from the original NXP at L=20 (see Figure 5.19).
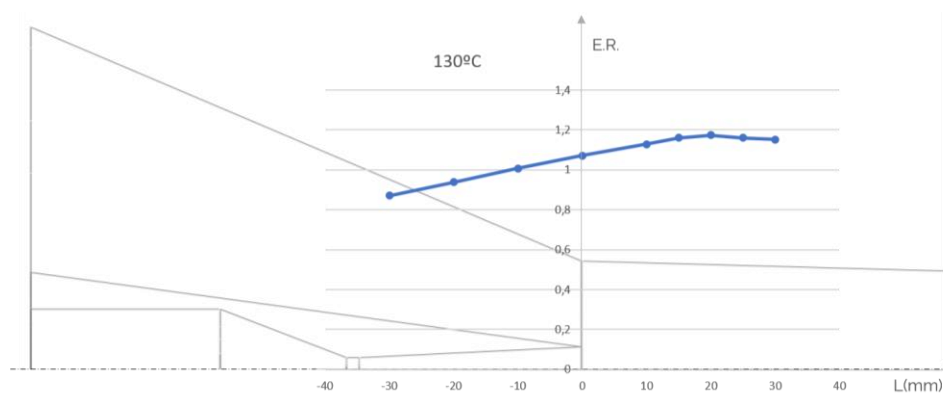
Figure 5.19 - Ejector Performance with different NXP for 130ºC.

The reason for such discrepancy is due to the location of the shock wave. Figure 5.20 and Figure 5.21 show that at a L=-20 case the shock waves, at sonic state, dissipates further from the diffuser compared to a L=20 case. These images show that for a motive flow temperature of 130ºC, the flow is at sub-critical mode in the second geometry. A decrease of backpressure could turn the flow double-chocked again.
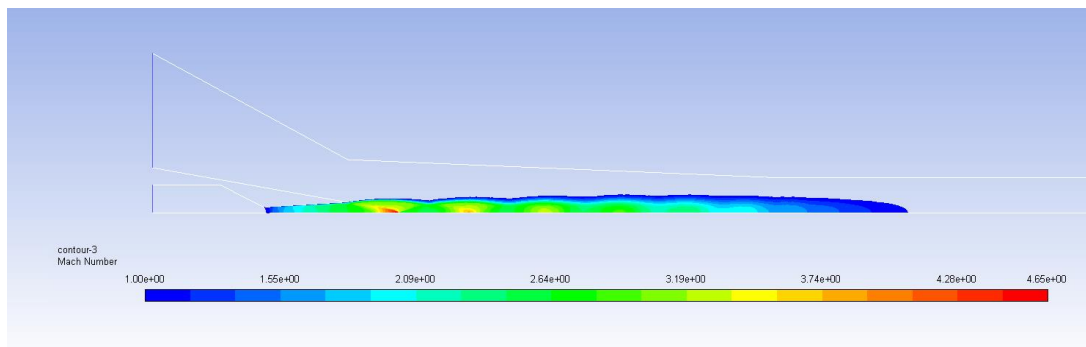
Figure 5.20 - Color-map of the supersonic areas on the diffuser section at a motive flow of 130ºC with L=-20.

Figure 5.21 shows that increasing the constant area section length, the shock wave is held on the constant area section, making the flow downwind subsonic and letting the diffuser work the way it was designed to.

As the flow operates under a sub-critical mode, the shock wave being moved further away from the diffuser means that the flow is approaching a critical, and desired, mode. Moreover, this leads to a better pressure recovery from the second case.
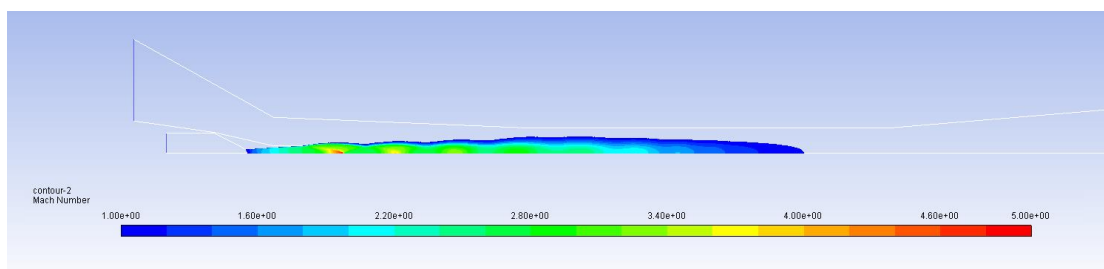
Figure 5.21 - Color-map of the supersonic areas on the diffuser section at a motive flow of 130ºC with L=20.

5.2.2 – Shock-Wave on higher temperatures

Figure 5.22 shows a color-map where the flow reaches supersonic for a motive flow temperature of 140ºC. It is possible to see that the flow reaches subsonic state already at the diffuser, not using the full potential of the diffuser.
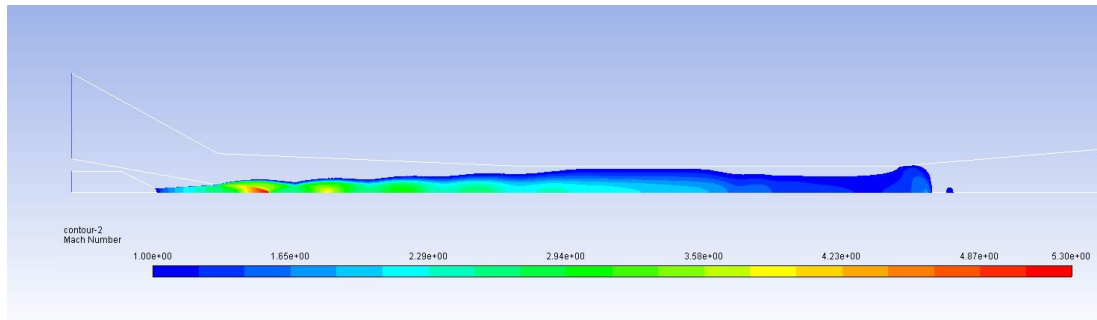
Figure 5.22 - Color-map of the supersonic areas on the diffuser section at a motive flow of 140ºC with L=-20.

At higher motive flow temperatures, the flow gets chocked in the constant area section or even before entering it. This way the flow does not allow the secondary flow to properly entrain the mixture chamber.

Although at a motive flow temperature of 130ºC the shock wave moved to the constant area section, increasing the constant area section length did not alter the sonic state of the flow reaching the diffuser for every temperature.

5.2.2 – Recirculation on the diffuser section

Increasing the constant area section length could be a solution for the recirculation problem on the diffuser. If the shock-wave occurred inside the constant area section or at the worst case scenario upstream from where it occurred in geometry 1, the diffuser could have been working close to optimum conditions (always subsonic), thus reducing the flow velocity losses and preventing problems of detachment, which lead to recirculation.

Table 5.4 compares the recirculation lengths of the first and third geometry. On this comparison, the optimum entrainment ratio is not given at the same L on each motive flow temperature. The recirculation were measured at the optimum NXP for each

motive flow temperature. The absence of a recirculation length value means that the recirculation left the outlet to the evaporator.

Table 5.3 - Recirculation length comparison between the original geometry and geometry 2.

Temperature	First Geometry (mm)	Third Geometry (mm)
180 ºC	-	-
170 ºC	-	-
160 ºC	177.11	187.32
150 ºC	98.05	105.71
140 ºC	0	16.88

Table 5.6 is a clear indicator that the increase of the constant area section length did not have the expected results. Every motive flow temperature had its recirculation values increased. The recirculation even started to appear at motive flow temperature of 140ºC.

5.2.3 – Results Overview

The results from the secondary geometry were very similar to the original one, two specific cases were presented, T=130ºC and T=140ºC, to show the only significant change on the results and an important comparison case, respectively.

Table 5.4 gives an overview of all thirty-five simulations done for the second geometry. The results are colored based on a colormap. Closer colors mean that the results are closer. It is possible to see that the change on the entrainment ratio is higher when changing the motive flow temperature than when changing the NXP.

Table 5.4 - Entrainment ratio results of all the simulations on the second geometry.

NXP	130	140	150	160	170	180
30	115.1%					
25	116.1%					
20	117.3%					
10	116.0%					
15	112.9%					
0	107.1%	89.7%	74.2%	60.9%	42.5%	32.1%
-5			75.9%			
-10	100.6%	92.4%	75.4%	63.3%		
-15		93.9%	74.7%	64.6%		
-20	93.8%	94.2%	74.7%	65.2%	47.6%	35.5%
-25		93.8%		57.2%	49.1%	37.6%
-30	87.0%	93.5%	73.7%	55.4%	43.6%	37.0%
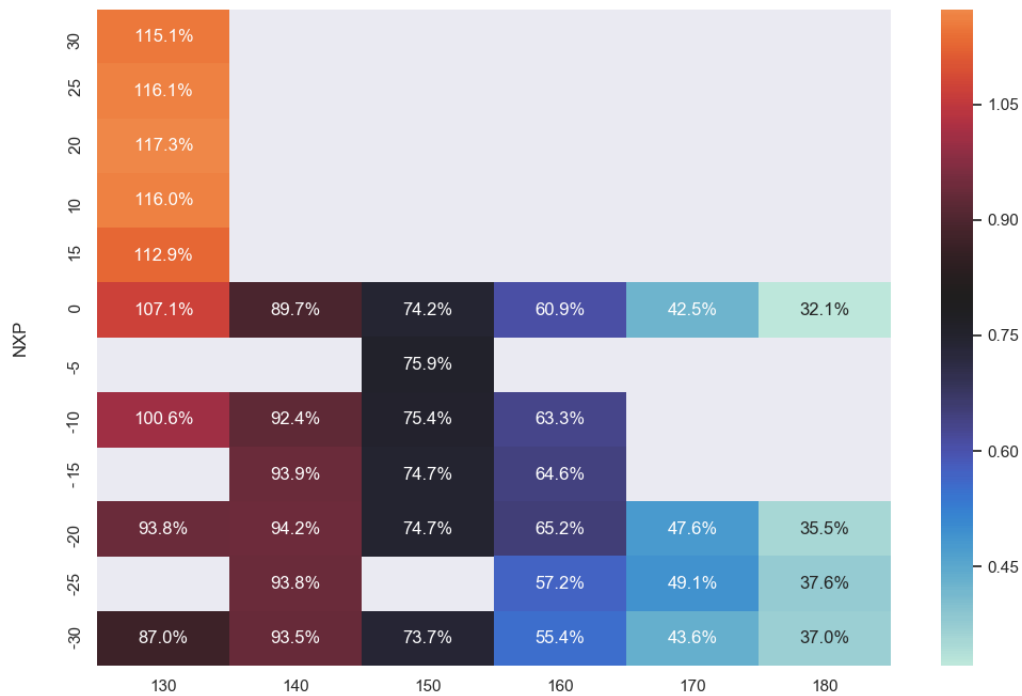
Table 5.4 shows that geometry 3 had the same behaviour as geometry 1 (see Table 5.2 and its conclusions), as expected.

5.2.4 – General Comparison of Results with Geometry 1

Table 5.5 compares the results of the simulations on the first two geometries. It is easy to conclude that the first geometry has always better entrainment ratio. Sometimes the differences get up to 3%.

The reason for the worse results is due to total pressure losses that happens at the walls because of shear stress and the recirculation still appear at the diffuser walls. The results meet the conclusions made by previous studies [47] that specify the maximum constant area length being seven times the constant area diameter.

The purpose of the constant area section's length increase were not satisfied since the recirculation did not stop to occur.

Table 5.5 - Comparison of results between Geometry 1 and 2.

	130	140	150	160	170	180
Original Geom (%)	119.59	94.55	77.04	65.28	50.68	38.02
2nd Geom. (%)	117.31	94.20	75.85	65.25	49.12	37.60
Best (%)	119.59	94.55	77.04	65.28	50.68	38.02
Difference (%)	2.28	0.34	1.18	0.03	1.56	0.42

5.3 – Adjusting the NXP while decreasing the diffuser angle

The third geometry reduces the diffuser angle to half. Decreasing the diffuser angle could prevent the appearance of recirculation zones on the diffuser since recirculation zones tend to appear on abrupt lines or on high angles.

This section describes the study that was made and its results.

After a careful analysis for every motive flow temperature on the original geometry, and since the flow behaves similarly between geometries for each motive flow temperature, only motive flow temperatures in which some non-identical phenomenon compared with the first geometry happen will be studied on detail for the second geometry.

5.3.1 – Recirculation comparison with geometry 1

The main reason for the geometry change was to reduce the recirculation at higher motive flow temperatures.

Comparing the results on the first and third geometry gives interesting and meaningful conclusions because on both cases, the optimum entrainment ratio is given at the same L on each motive flow temperature. The recirculation were measured at the optimum NXP for each motive flow temperature. The results are presented in Table 5.6.

Table 5.6 - Recirculation length comparison between the original geometry and geometry 3.

Temperature	First Geometry (mm)	Third Geometry (mm)
180 ºC	-	223.58
170 ºC	-	161.34
160 ºC	177.11	126.09
150 ºC	98.05	59.31
140 ºC	0	0

Table 5.6 is a clear indicator that decreasing the diffuser angle lead to a decrease of the recirculation length.

Although not having direct interference on the ER, recirculation was reduced, thus general efficiency was improved. Recirculating regions occur always attach to a wall due to pressure gradients which lead to irreversibility on the flow.

Moreover, the entropy increase (irreversibility) represent the total pressure loss, in the irreversible flow process. This is especially true for higher motive flow temperatures where the recirculation can even reach the evaporator.

5.3.2 – General Comparison of Results with Geometry 1

Table 5.7 gives a comparison between the first and third geometry results. The results are very similar to the first geometry results with the exception of the 130ºC and 120 ºC motive flow temperature.

Table 5.7 - Comparison of results between Geometry 1 and 3.

T(ºC)	120	130	140	150	160	170	180
Original Geom	167.1	119.6	94.6	77.0	65.3	50.7	38.0
2nd Geom.	170.1	122.4	94.4	77.0	65.3	50.8	37.7
Best	170.1	122.4	94.6	77.0	65.3	50.8	38.0
ER Difference (ER %)	3.01	2.82	0.11	0.00	0.03	0.11	0.28

The entrainment ratio was improved on motive flow temperatures of 120ºC and 130ºC. For higher temperatures the entrainment ratio improvement was not significant. Decreasing the diffuser angle alone, does not improve the entrainment ratio for any of the evaluated temperatures. Other optimization methods, such as changing the area ratio, should be used to tackle this issue.

With the results of Figure 5.8, geometry 3 should be chosen to be the ejector geometry. Improvements can be up to 3% on the entrainment ratio values. Moreover, the smaller recirculation length is another factor to opt for the third geometry.

5.3.3 – Motive Flow of 120ºC, 130ºC and 140ºC

Motive flow temperature of 120ºC and 130ºC had slightly better results in comparison with the first geometry, encouraging the change on the ejector design. However, for higher motive flow temperatures, the entrainment ratio results and ideal NXP were very similar to the first geometry, suggesting that this change on the geometry was not producing any meaningful results.

The reason behind such occurrence lays with the fact that on the first two cases, there is no supersonic flow chocking all of the diffuser's front diameter or even at the constant area section, whereas at higher temperatures, the supersonic flow chokes completely the flow at the entrance of the diffuser, causing malfunctions on the diffuser to the point that the diffuser do not work properly (see Figure 2.7 on page 22 for a better understanding on supersonic flow on a diffuser). A solution to this problem should be a spindle to control the area ratio.
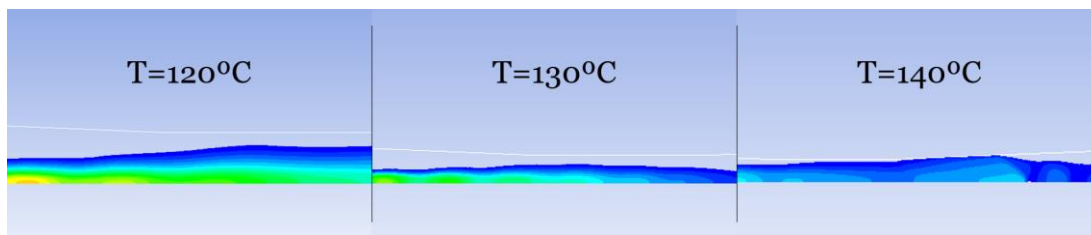
Figure 5.23 - Comparison of supersonic flows at the diffuser entrance.

5.3.4 – Results Overview

Table 5.8 gives an overview of all forty-four simulations done for the first geometry. The best entrainment ratio results were given at a motive flow temperature of 130°C in which the optimum NXP is located at L=-25. The results are colored based on a colormap. Closer colors means that the results are closer. It is possible to see that the change on the entrainment ratio is higher when changing the motive flow temperature than when changing the NXP.

Table 5.8 - Entrainment ratio results of all the simulations on the third geometry.

NXP	120	130	140	150	160	170	180
40	161.7%						
0	166.6%	119.6%	91.3%	74.1%	60.8%	43.2%	32.7%
-10	168.4%	121.2%	92.4%		63.3%		
-15	169.7%	121.6%	94.4%	74.7%	64.6%	48.3%	35.9%
-20	169.7%	122.4%	94.2%	74.7%	65.3%	48.3%	36.0%
-25	170.1%	121.9%	93.8%	75.4%	65.1%	49.6%	36.1%
-30	169.8%	118.9%	93.7%	76.5%	63.4%	50.8%	37.7%
-35				77.0%		48.2%	31.0%
-40				75.8%			
Best	170.1%	122.4%	94.4%	77.0%	65.3%	50.8%	37.7%
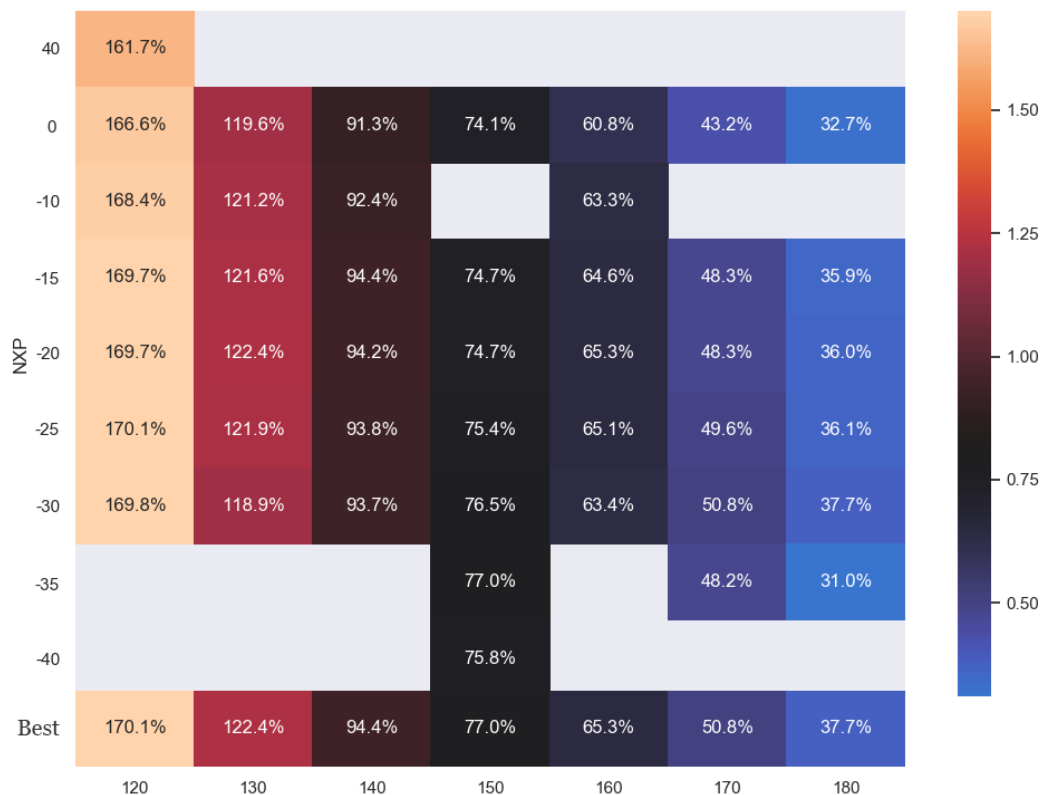
Table 5.8 shows again the same tendency presented with Table 5.2 and Table 5.4. Therefore, the same conclusions presented for the first geometry is also applied for the third geometry.

Table 5.8 results are plotted showing the ideal NXP for each temperature. In Figure 5.24 two ideal paths which indicate two expected tendencies are created. The first path represents a downstream of the ideal NXP with the increase of temperature and the

second path delineate a stable NXP position around L=-25. It is noticeable a slight tendency of the optimum NXP to go downwind with the increase of the motive flow temperature. This is an expected result and it is justified because with the temperature increase, the flow exiting the nozzle will increase the degree of under-expansion, thus shortening the effective area of entrainment.

Hence, the relationship between the NXP and the effective area is critical to understand how to optimize the ejector geometry.
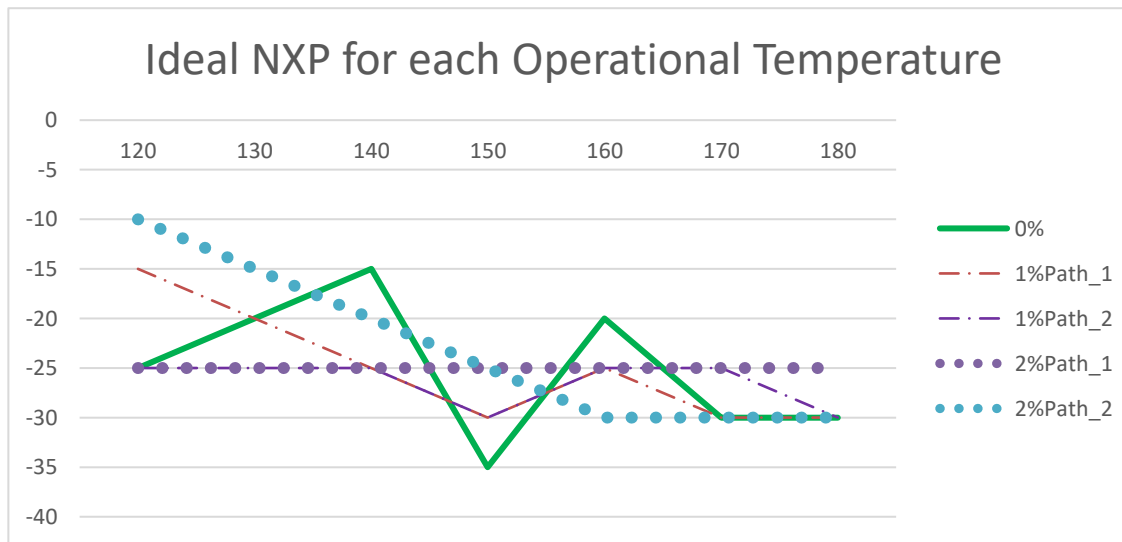
Figure 5.24 - Optimum NXP for each motive flow temperature.

However, the plot results (Figure 5.24 0% line) are not totally consistent with the expected results. The expected results would be a more straightforward, peak-less, descending line.

As CFD simulations have an inherent uncertainty associated with, 1 and 2% error margin from the best entrainment ratio results is an accurate approximation of the results.

Two paths were drawn for each error margin. 1%Path_1, red dash followed by a point, which represents a descending line with still a peak at motive flow temperature of 150ºC and 160ºC and 1%Path_2, blue dash followed by a point, represents a trying to be more stable line near the L=-25 NXP. The two percent margin paths are represented by dots and follow the same tendency to follow a certain path as in the previous 1% paths.

It is noticeable that the results are closer to the expected behaviour. There is still a down-winding trend of the NXP for higher temperatures for the 1% error margin, which are dissipated at a 2% error margin.

Table 5.9 results permit to conclude that having a variable geometry ejector is important. The improvements can go up to 7.58% when compared with an original L=0 value.

Table 5.9 - E.R. improvement with the movable NXP for each temperature.

	120°C	130°C	140°C	150°C	160°C	170°C	180°C
L=0 (%)	166.64	119.60	91.31	74.10	60.82	43.21	32.68
Optimum L (%)	169.74	122.41	94.44	77.04	65.25	50.79	37.74
Improvement (ER %)	3.09	2.81	3.13	2.94	4.44	7.58	5.06

However, with a more careful statistical analysis, it is possible to see that a movable NXP is not a necessity for the system.

As seen in equation 5.1, the statistical analysis consisted in creating an array called ER variation (ΔER^* equation 5.1), dependent on the NXP, which measured the difference of the entrainment ratio for each temperature in every simulated NXP with the best entrainment ratio for every temperature.

$$\Delta ER^* (NXP) = ER_{Optimum\_NXP} - ER_{NXP,T} \qquad \textbf{5.1}$$

To choose the best NXP, the major parameter to be analysed was the Mean parameter, which measured the accuracy of the approximation to the ideal NXP values. The other import parameter to be considered was the standard deviation (Std in Table 5.10), which measured the precision.

Table 5.10 was made with data-science tools in python (see Appendix A.3). A matrix was created comparing each NXP and entrainment values with the best NXP and entrainment ratio for each temperature.

A movable nozzle can be a great tool to fit every condition, however, moving the nozzle brings some energy consumption that should not be wasted if a compromise solution will not affect to much the entrainment ratio. Table 5.10 shows that for a NXP with L=-25, the mean variation from the best entrainment ratio for each temperature is below 1%. In fact, L=-25 had the second best result on Std, which means a great precision on the approximation. This NXP should be considered as the ejector nozzle position.

Table 5.10 - Statistical study of the best overall NXP (In ER%).

NXP L	Mean	Std	Min	Max	25%	50%	75%
-25	0.83	0.67	0	1.63	0.33	0.69	1.42
-30	0.98	1.29	0	3.51	0.13	0.51	1.28
-20	1.03	1.11	0	2.49	0.12	0.43	2.03
-15	1.22	1.01	0	2.51	0.51	0.78	2.10
-10	1.72	0.34	1.25	2.01	1.58	1.81	1.94
0	4.20	1.71	2.80	7.58	3.03	3.46	4.75

Figure 5.25 shows how the optimum entrainment ratio changes for each motive flow temperature. The entrainment ratio tends to increase from the over-expanded case until reaching a maximum value when the flow is ideally expanded. With the increase of the motive flow temperature, the flow turns under-expanded and the entrainment ratio tend to decrease. The simulation results are in accordance with the expected results. A comparison between three cases of different optimum entrainment ratio per temperature case can be seen (the red line being for the new backpressure applied to the motive flow temperature of 120ºC, the blue dots with the original backpressure value and the green line being the entrainment ratio for NXP L=-25 mm).
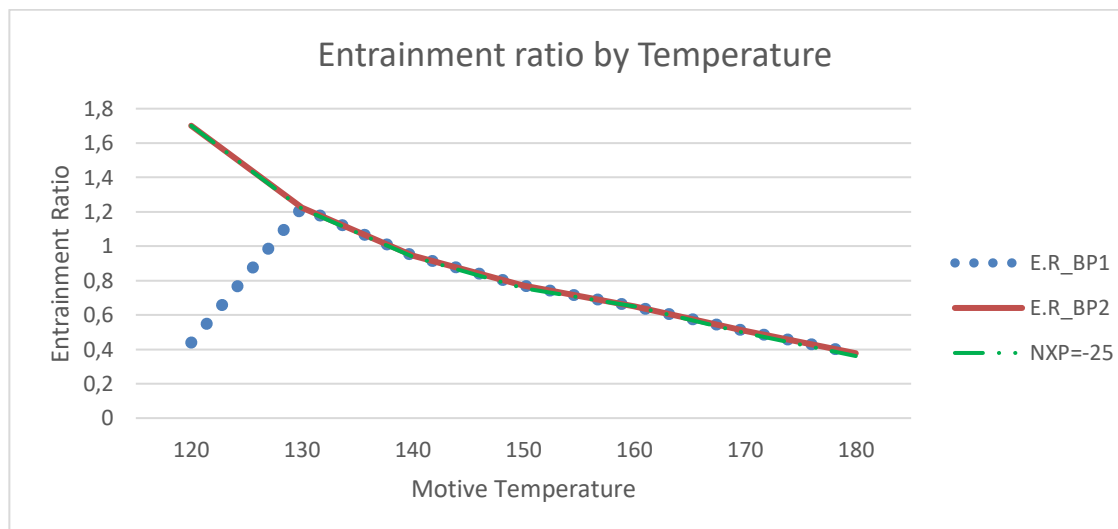
Figure 5.25 - Optimum entrainment ratio per motive flow temperature

Figure 5.25 confirms that a NXP of L=-25 should be chosen, the differences for the optimum entrainment ratio cases are minimum.

6. Conclusions and Future Work

6.1 – Conclusions and Ejector Final Design

Current and future water challenges will require sustainable solutions for the use of the planet's water resources. Solar desalination can be one these solutions. MED-TVC desalination requires low-energy compared with other desalination methods. The most important part of a MED-TVC installation efficiency and performance is the ejector. Ejectors permit to attain high performance at design conditions; however, efficiency drops significantly and operation failure tends to occur when operating at off-design conditions. A solution is to use a variable geometry ejector, i.e. geometry adapts to operation conditions. The effect of having a movable nozzle was studied, being the main focus of this project. Furthermore, combinations on having a movable nozzle while increasing the length of the constant area section and moving the nozzle while decreasing the diffuser angle were also simulated.

Numerical models have proven to be the most reliable tools to simulate fluids inside ejectors. A robust CFD model was created using steady-state flow and axis-symmetric conditions. Second-Order Upwind Scheme and QUICK Scheme were chosen as the upwind schemes since they are the most accurate schemes to use. Coupled methods were used as the Pressure-Velocity coupling algorithms since the steam ejector flow is compressible. RANS was the chosen turbulence model as it is computationally less expensive and simulate all the turbulence spectrum. The simulations were done with the Realizable k-ε turbulence model.

Mesh design had a big influence on this work. ICEM-CFD software was used to create the meshes. Three different mesh geometries were modeled and tested its independency. On this study's mesh independence calculation, it was concluded that the number of finite volumes were not the only parameter to be considered on the mesh independence but also the design of the mesh. Thirty-four different meshes, with proportional number of nodes to follow the original mesh independence study, were designed to simulate every NXP for all four different geometries. Boundary conditions were set.

The effects of various operating conditions and design parameters on the ejector performance have been evaluated by using CFD methods. The different geometry models were evaluated based on the entrainment ratio indicator. Apart from the entrainment ratio on each simulation, CFD visual results have a significant importance on this study because it reveals detailed flow behaviour inside the ejector, thus a better understanding of the design parameters that should be modified.

A total of 140 simulations were carried out, and the main conclusion can be drawn:

For the first simulated geometry, at the original backpressure and motive flow temperature of 120ºC conditions, the flow exiting the nozzle was slightly over-expanded, the optimum NXP was had down winding its original location. The entrainment ratio was lower than expected considering that this motive flow temperature was the one optimized in previous studies. This study proved the underpredicting nature of the critical back pressure value by the CFD. The critical backpressure predicted by Fluent is lower than the one predicted by the EES script, therefore, the original simulation, with higher backpressure value than the CFD critical back pressure, was misleading ANSYS Fluent to a much lower entrainment ratio. As a decrease of backpressure below the critical backpressure values do not affect the entrainment ratio values, new simulations with reduction of the backpressure were done to find the optimum NXP and entrainment ratio values for a motive flow of 120ºC.

From a motive flow of 130ºC, the flow exiting the nozzle will be under-expanded and the optimum NXP for these cases are located upwind from the original NXP. When the pressure is increased, a smaller effective area is available. Therefore, less amount of the secondary flow is drawn to the mixing chamber while also increasing the primary flow rate. At motive flow temperatures of 150ºC, a recirculation zone starts to appear at the diffuser section. This zone will only get bigger with the increase of the motive flow temperature. The entrainment ratio tends to decrease with the increase of the motive flow temperature (120ºC – 180ºC) and its changes are higher when changing the motive flow temperature compared to a NXP change.

The effective area is the main responsible for a bigger or smaller entrainment ratio. As the motive flow properties exiting the nozzle is independent of the NXP, moving the NXP upstream will shorten the length of the jet core and the wall of the constant pressure-section. Moreover, there is a tendency of the optimum NXP to go upstream with the increase of the motive flow temperature. For each given working conditions, there is an optimum NXP where the ejector works at the highest entrainment ratio. Usually there is a 10-millimeter margin where the entrainment ratio do not varies more than 1% compared to the optimum NXP entrainment ratio.

Increasing the constant area section length outcome in the shock wave movement inside the constant area section, thus preventing the occurrence of recirculation zones on the ejector. For a motive flow temperature of 130ºC and the optimum NXP position, the shock wave moved successfully inside the constant area section. For higher temperatures, even though the shock wave was moved upstream as wanted, it did not reach the constant area section. Recirculation got bigger on every motive flow temperature and even started to appear at lower temperatures (140ºC). With the increase of the constant area section came an increase of the total pressure losses that happens at the walls because of shear stress. Moreover, there was a general entrainment ratio decrease of 2%. Moving the shock-wave closer to the constant area section did not overlap these losses. Therefore, having increased the constant area section length did not bring any benefits and this geometry should not be implemented.

A final study was done simulating a geometry with half of the original diffuser angle. The highest entrainment ratio values were simulated at motive flow temperatures of 120ºC. Recirculation was reduced and while does not influence the entrainment ratio on the higher temperatures, reducing the recirculation zones brings general efficiency improvements. The original geometry and the third one had the optimum ER value for the same L on each temperature. Motive flow temperature of 120ºC and 130ºC had their entrainment rate values improved compared with the original geometry. When the motive flow temperature was higher than 130ºC (140ºC - 180ºC), the entrainment ratio results were the same as the original geometry ones. On the first two temperature cases (120ºC and 130ºC), there is no supersonic flow chocking all the beginning of the ejector or even at the constant area section, whereas at higher temperatures, the supersonic flow chokes completely the flow at the entrance of the diffuser, causing malfunctions on the diffuser to the point that it do not work properly. The entrainment ratio tends to decrease with the increase of the motive flow temperature (120ºC – 180ºC) and its changes are higher when changing the motive flow temperature compared to an NXP change, as

happened with the first geometry. Moreover, there is a tendency of the optimum NXP to go upstream with the increase of the motive flow temperature.

Although being able to give the ejector optimum performance at every motive flow temperature conditions, a movable NXP does not bring significant advantages to the system.. A statistical study was made using the 34 different NXP results. It was concluded that for the best geometry (geometry 3), an NXP with L=-25 is almost as good as having a movable nozzle. With the nozzle on this position, the difference between the best NXP entrainment ratio and the NXP at L=-25 never surpasses 1.6%. Thus, with all the NXP studied, the study concludes that a L=-25 NXP is even more beneficial compared with a movable NXP.

Only changing the constant area section or the diffuser angle did not improve significantly the entrainment ratio for all ranges of temperatures. A range of temperatures so wide as this project used would require other methods (i.e. a spindle to change the area ratio), or more likely a combination of the methods studied on this work and new ones.

6.2 – Future Work

The main breakthrough of this work was indeed doing the optimization of so many parameters for such a wide range of motive flow temperatures. Few previous works had done with such a temperature range.

On what a deeper analysis of what was done in this work concerns, it will be interesting to compare a real physical ejector with the critical backpressure values of the CFD and from the previously calculated EES. Also, testing a different turbulence model (e.g. RNG k-ε) can shorten the error associated with the CFD critical backpressure value.

This thesis was mainly focused on the use of a movable NXP to find the maximum entrainment ratio. There are other ways to increase the entrainment ratio with also having the versatility to adapt to such wide range of temperatures. Future work should concern a deeper analysis of particular mechanisms, new proposals to try different optimization methods, such as using a spindle at the nozzle entrance, therefore the area ratio can be changed to optimum values. A future work should be concentrated on finding the optimum values for the spindle, which in theory can results in even higher entrainment ratio improvements compared with moving the NXP. Since the project aims to create a robust and versatile solar desalination device, the temperature ranges have to be this wide to guarantee an almost ideal operational conditions at a wide range of conditions. It was proven by this study that one specific change on the ejector design will not have the same effect for every motive flow temperature. Thus, the new works that will be done testing new design parameters should be complemented with this work in order to create stronger design parameters for every temperature condition.

This work produced easily more than two hundred simulations and over 90 meshes were done. With such an amount of data produced by one work it is easy to predict that CIENER can produce one of the most significant amount of ejector's simulation and meshes data, important for the future. With the rise of artificial intelligence powered by machine learning techniques, it will be positive and forward-looking to CIENER to keep storing all the data from the simulations for a future work creating ANSYS Fluent sub-programs to get ejector simulation much easier convergency (the program will interpret how the previous simulations converged and which convergency parameters should it use at every time) and better meshes (the program will learn from the mistakes made doing worse designed meshes as well as well-designed meshes, creating perfect designed meshes in fraction of the time and for every conditions).

Appendix

A.1 – Mesh optimization flowchart
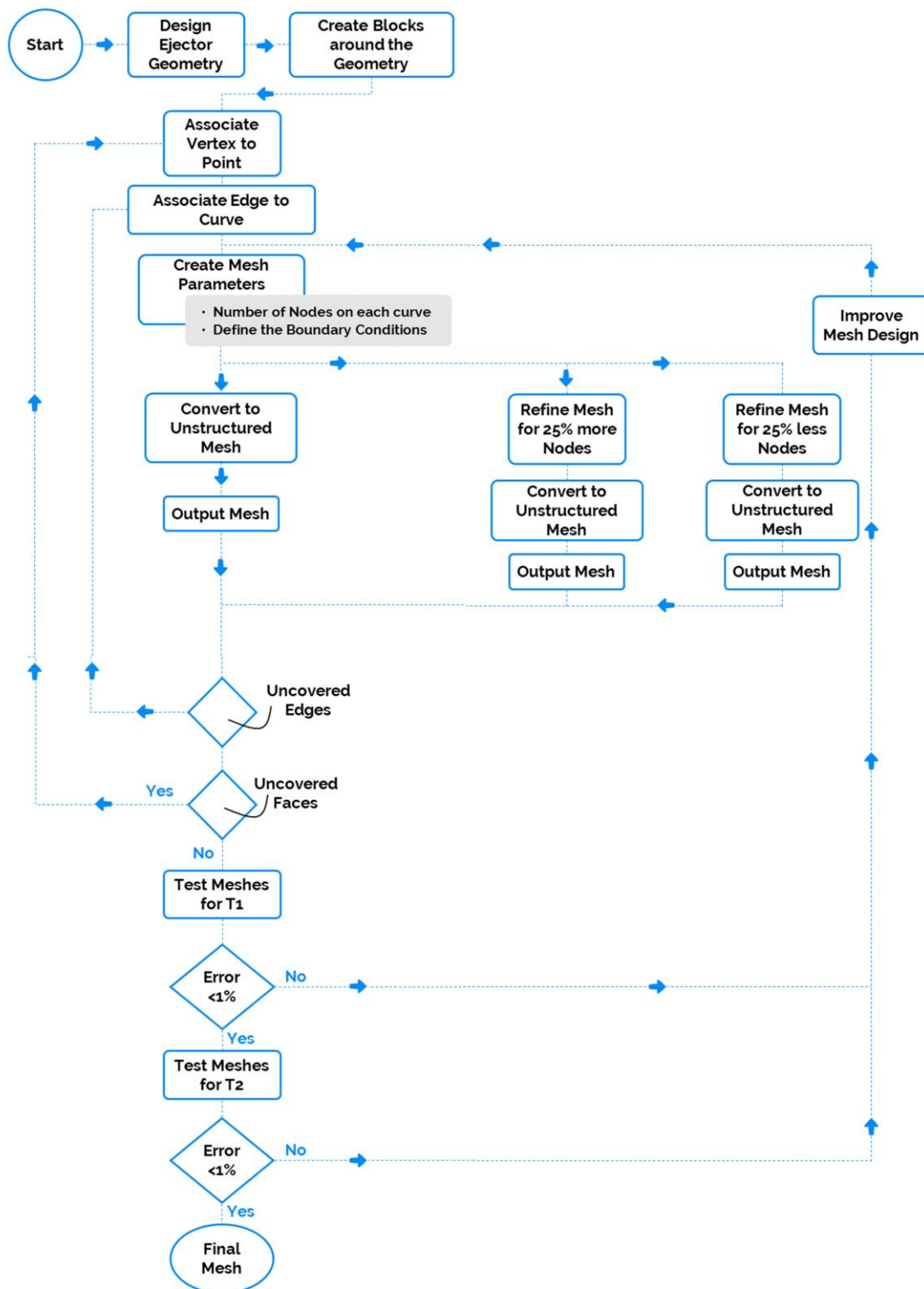
Figure A.0.1 - Mesh optimization flowchart

A.2 – Entrainment ratio and L plot analysis

Figure A.0.2 describes the coordinate system of the entrainment ratio and L plots. The entrainment ratio is the y coordinate and the L is the x coordinate.
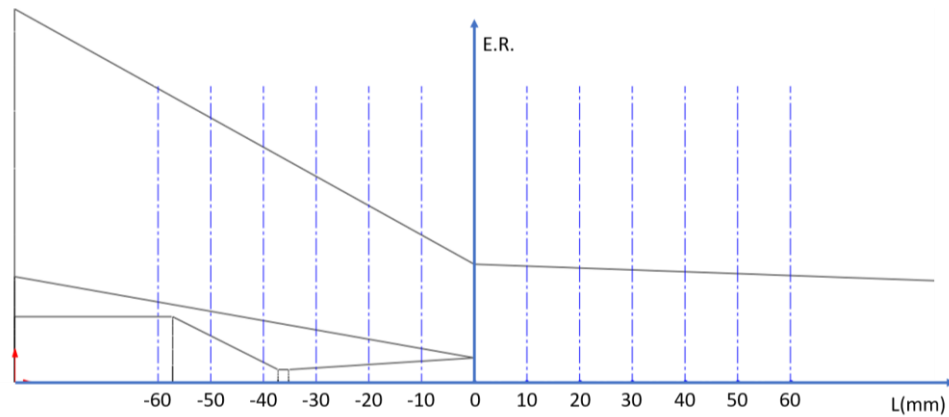
Figure A.0.2 - Coordinate system of the plot

For a 120ºC case, where the best entrainment ratio is located at L=40 (see Figure A.0.3), the NXP would move 40 millimeters downwind. Each dot on the blue line marks a simulation made for a specific L.
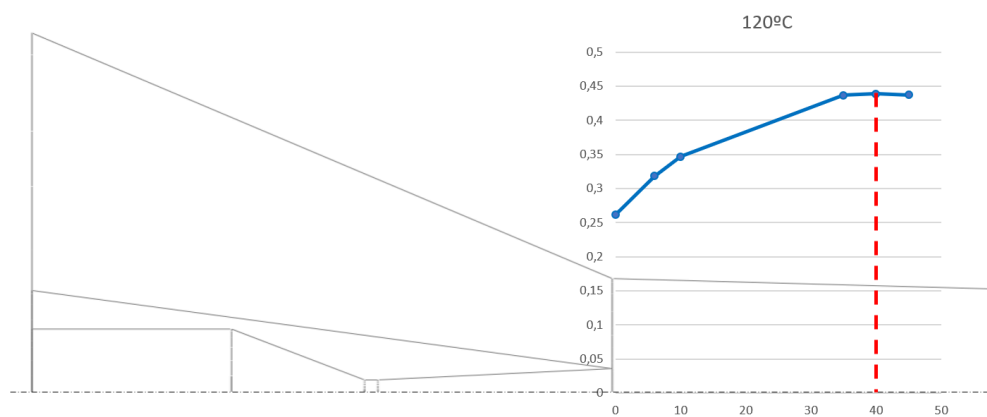
Figure A.0.3 - 120ºC motive temperature example

Following the example on Figure A.0.3, the final geometry of the ejector would similar to the drawing presented on Figure A.0.4.
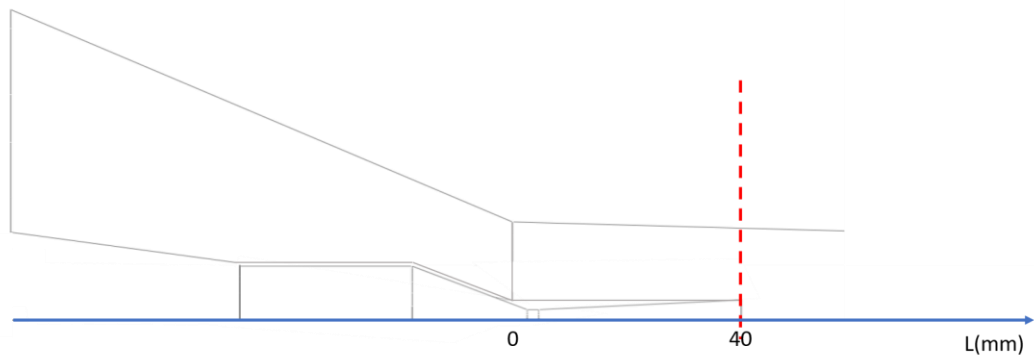
Figure A.0.4 - Ejector when L=40

A.3 – Python script to automate the mesh creation process

```python
import numpy as np
import os


def changing_lines(n, cnt, old_Line, point_1,point_2,point_3,point_4):

    new_path()

    n_float = f'{n}'

    new_line = {}
    interp_1 = interpolacao(point_1, point_3, n)
    interp_1_num = interp_1['y']
    interp_1_float = f'{interp_1_num}'

    interp_2 = interpolacao(point_2, point_4, n)
    interp_2_num = interp_2['y']
    interp_2_float = f'{interp_2_num}'

    new_line[3] = Line[3].split('AQUI')[0] + n_float +
Line[3].split('AQUI')[1]
    new_line[3] = new_line[3].split('INTERP')[0] + interp_1_float +
new_line[3].split('INTERP')[1]

    new_line[6] = Line[6].split('AQUI')[0] + n_float +
Line[6].split('AQUI')[1]
    new_line[6] = new_line[6].split('INTERP')[0] + interp_2_float +
new_line[6].split('INTERP')[1]

    new_line[218] = Line[218].split('AQUI')[0] + n_float +
Line[218].split('AQUI')[1]
    new_line[219] = Line[219].split('AQUI')[0] + n_float +
Line[219].split('AQUI')[1]
    new_line[220] = Line[220].split('AQUI')[0] + n_float +
Line[220].split('AQUI')[1]
    new_line[221] = Line[221].split('AQUI')[0] + n_float +
Line[221].split('AQUI')[1]
    new_line[66] = Line[66].split('AQUI')[0] + n_float +
Line[66].split('AQUI')[1]
    new_line[65] = Line[65].split('AQUI')[0] + n_float +
Line[65].split('AQUI')[1]

    doc_lines = {}
    txt_corrido = ''

    for i in range(1, cnt):

        try:

            doc_lines[i] = new_line[i]
            txt_corrido = txt_corrido + '\n' + doc_lines[i]

        except:

            doc_lines[i] = old_Line[i]
            txt_corrido = txt_corrido + '\n' + doc_lines[i]
```

```python
    n_for = n_float.split('-')[1]

    txt_f = open(f'C:\\Users\\Diogo
Sá\\Desktop\\NEWNEWNEW\\MESH\\scripted\\minus{n_for}.rpl',"w+")
    txt_f.write(txt_corrido)
    txt_f.close

    return txt_corrido


def interpolacao(point_1, point_2, new):

    a = np.array([[point_1['x'],1], [point_2['x'],1]])
    b = np.array([point_1['y'], point_2['y']])

    curve = np.linalg.solve(a , b)

    new_y = curve[0]*new + curve[1]

    new_pos = {'x': new, 'y': new_y}

    return new_pos


def new_path():

    newpath = f'C:\\Users\\Diogo
Sá\\Desktop\\NEWNEWNEW\\MESH\\scripted'

    if not os.path.exists(newpath):

        os.makedirs(newpath)


def main():

    origin_filepath = f'C:\\Users\\Diogo
Sá\\Desktop\\NEWNEWNEW\\MESH\\mesh_150mil_yeah.rpl'
    Line = {}

    try:

        with open(origin_filepath) as fp:

            line = fp.readline()
            cnt = 1

            while line:

                Line[cnt] = line.strip()

                line = fp.readline()

                cnt += 1

    finally:

        fp.close()

    point_1 = {'x': 0, 'y': 22.3, 'z':0}
    point_2 = {'x': 0, 'y': 22.15, 'z':0}
```

```python
    point_3 = {'x': 158.3, 'y': 15.7, 'z':0}
    point_4 = {'x': 158.3, 'y': 15.55, 'z':0}

    for i in range(-50, 0, 5):

        changing_lines(i, cnt, Line, point_1, point_2, point_3,
point_4)


if __name__ == "__main__":

    main()
```

A.4 – Python Data-Science script to study the best NXP position

```python
import matplotlib.pyplot as plt
import pandas as pd
import numpy as np; np.random.seed(0)
import seaborn as sns; sns.set()
from mpl_toolkits.mplot3d import Axes3D


csv_reader_1 = open(f'C:\\Users\\Diogo
Sá\\Desktop\\NEWNEWNEW\\matplotlib\\diff.csv', 'rb')
csv_read_1 = pd.read_csv(csv_reader_1, encoding='latin1', sep = ';')
csv_reader_1.close()

def plotting(csv_read_1):

    csv_plot = csv_read_1
    sns.palplot(sns.color_palette("Paired"))

    print('\n'*2)

    index_values = csv_plot.loc[:,'NXP']


    csv_plot.set_index('NXP', inplace=True, drop=True)

    print(index_values)

    x = sns.heatmap(csv_read_1, annot=True, center=0.8, fmt='.1%')

    plt.show()
# plotting(csv_read_1)

NXP = {}
mean = {}
std = {}
df_min = {}
df_max = {}
df_25 = {}
df_50 = {}
df_75 = {}

max_ER = {}
index_ER = {}
NXP_ER = {}
temp = {}

diff = {}

ER_max = csv_read_1
j = 0

for i in range(120, 190, 10):

    temp[i] = f'{i}'

    max_ER[i] = ER_max.loc[:, temp[i]].max()
```

```python
        index_ER[i] = ER_max.loc[ER_max[temp[i]].idxmax()].name
        NXP_ER[i] = ER_max.iloc[index_ER[i]].loc['NXP']

        temp[i] = i

        j += 1


    ER_df = pd.DataFrame({'Temperature': temp,
                          'ER': max_ER,
                          'NXP': NXP_ER})

print('\n')
print(ER_df)
print('\n')
print(csv_read_1)
print('\n')

ER_df = ER_df.T
ER_df = ER_df.iloc[1]

j = 0

for i in range(120, 190, 10):

    print(csv_read_1.iloc[0][f'{i}'])
    print(ER_df.iloc[j])

    csv_read_1.at[0, f'{i}'] = ER_df.iloc[j]

    j += 1

for i in range(1, 7):

    diff = csv_read_1.iloc[0] - csv_read_1.iloc[i]
    del diff['NXP']

    NXP[i] = csv_read_1.iloc[i]['NXP']
    mean[i] = diff.describe()['mean']
    std[i] = diff.describe()['std']
    df_min[i] = diff.describe()['min']
    df_max[i] = diff.describe()['max']
    df_25[i] = diff.describe()['25%']
    df_50[i] = diff.describe()['50%']
    df_75[i] = diff.describe()['75%']

df = pd.DataFrame({'NXP': NXP,
                   'Mean': mean,
                   'Std': std,
                   'Min': df_min,
                   'Max': df_max,
                   '25%': df_25,
                   '50%': df_50,
                   '75%': df_75})

df = df.dropna()

print('\n'*5)
```

```python
print('\n'*5)
# print(diff)

mean_50 = df.loc[:, 'Mean'] - df.loc[:, '50%']

print(mean_50)

del(df['25%'])
del(df['75%'])

df['50%-Mean'] = pd.Series(mean_50, index=df.index)

# print(df.sort_values(by='50%-Mean', ascending=True))
print(df.sort_values(by='Mean', ascending=True))
```

References

1.   New Climate Economy, *Unlocking the Inclusive Growth Story of the 21st Century: Accelerating Climate Action In Urgent Times*. New Climate Economy, Washington, DC, http://www. newclimateeconomy. report, 2018. **122**.
2.   A. M. K. El-Ghonemy, *Water desalination systems Powered by Renewable energy sources, a Review*. Renewable and Sustainable Energy Reviews, 2012. **16**(3): p. 1537-1556.
3.   Vazken Andréassian, *'Day Zero': From Cape Town to São Paulo, large cities are facing water shortages*, in *The Conversation*. 2018.
4.   M. J. Booysen, M. Visser, and R. Burger, *Temporal case study of household behavioural response to Cape Town's "Day Zero" using smart meter data*. Water Research, 2019. **149**: p. 414-420.
5.   Noreddine Ghaffour, Thomas M. Missimer, and Gary L. Amy, *Technical review and evaluation of the economics of water desalination: Current and future challenges for better water supply sustainability*. Desalination, 2013. **309**: p. 197-207.
6.   Raphael Semiat, *Energy Issues in Desalination Processes*. Environmental Science & Technology, 2008. **42**(22): p. 8193-8201.
7.   Zhenyu Li, Afreen Siddiqi, Laura Diaz Anadon, and Venkatesh Narayanamurti, *Towards sustainability in water-energy nexus: Ocean energy for seawater desalination*. Renewable and Sustainable Energy Reviews, 2018. **82**: p. 3833-3847.
8.   Rapichan Phurisamban Heather Cooley, *The Cost of Alternative Water Supply and Efficiency Options in California* 2016
9.   International Water Association, *Desalination – Past, Present and Future*. 2016.
10. ADROIT MARKET RESEARCH, *Global Water Desalination Market and Its Related Technologies (Reverse Osmosis, Multi-stage Flash Distillation, Multi Effect Distillation, Hybrid, Electrodialysis), Its Source (Seawater, Brackish Water), Regional Trends and Forecast 2018 to 2025*. 2018.
11. Ventures Onsite, *MENA Desalination Market*. 2019.

12. Steven Griffiths, *A review and assessment of energy policy in the Middle East and North Africa region.* Energy Policy, 2017. **102**: p. 249-269.
13. The World Bank. *Global Solar Atlas.* 2016.
14. Soteris A. Kalogirou, *Seawater desalination using renewable energy sources.* Progress in Energy and Combustion Science, 2005. **31**(3): p. 242-281.
15. BP, *BP Energy Outlook.* 2019.
16. Mita Bhattacharya, Sudharshan Reddy Paramati, Ilhan Ozturk, and Sankar Bhattacharya, *The effect of renewable energy consumption on economic growth: Evidence from top 38 countries.* Applied Energy, 2016. **162**: p. 733-741.
17. Muhammad W. Shahzad, Muhammad Burhan, Li Ang, and Kim C. Ng, *1 - Adsorption desalination—Principles, process design, and its hybrids for future sustainable desalination*, in *Emerging Technologies for Sustainable Desalination Handbook*, V.G. Gude, Editor. 2018, Butterworth-Heinemann. p. 3-34.
18. ADROIT Market Research, *Global Water Desalination Market and Its Related Technologies, Trends and Forecast 2018 to 2025.* 2019.
19. Mahmoud Shatat, Mark Worall, and Saffa Riffat, *Opportunities for solar water desalination worldwide: Review.* Sustainable Cities and Society, 2013. **9**: p. 67-80.
20. G.K.C. Ding, Ghosh, S., *Sustainable Water Management-A Strategy for Maintaining Future Water Resources.* Encyclopedia of Sustainable Technologies, 2017.
21. Ihsan Ullah and Mohammad G. Rasul, *Recent Developments in Solar Thermal Desalination Technologies: A Review.* Energies, 2018. **12**(1): p. 119.
22. The World Bank, *Renewable Energy Desalination - An Emerging Solution to Close the Water Gap in the Middle East and North Africa.* 2012.
23. *Al Khafji Solar Saline Water Reverse Osmosis (Solar SWRO) Desalination Plant*, in *Water Technology*. 2017.
24. KATHRYN S. BODEN AND CHINMAYEE V. SUBBAN, *A ROAD MAP FOR SMALL-SCALE DESALINATION.* OXFAM RESEARCH REPORT, 2018.
25. Simon Atkinson, *Applying Flex EDR to produced water improves EOR economics.* Membrane Technology, 2018. **2018**(6): p. 9.
26. K. Wangnick, *Global Overview of Water Desalination Technology and the Perspectives*, in *International Conference Spanish Hydrological Plan and Sustainable Management*. 2003: Zaragoza, Spain.
27. Francisco Diogo Abreu Santos Moniz Azevedo, *Renewable Energy Powered Desalination Systems: Technologies and Market Analysis.* 2014, UNIVERSIDADE DE LISBOA.
28. Abdulkarim Mayere, *Solar powered desalination.* 2011, University of Nottingham.
29. Global Water Intelligence (GWI/IDA DesalData), *Market profile and desalination markets.* 2009–2012.
30. Roberto Borsani and Silvio Rebagliati, *Fundamentals and costing of MSF desalination plants and comparison with other technologies.* Desalination, 2005. **182**(1): p. 29-37.
31. M. Al-Shammiri and M. Safar, *Multi-effect distillation plants: state of the art.* Desalination, 1999. **126**(1): p. 45-59.
32. M. A. Sharaf, A. S. Nafey, and Lourdes García-Rodríguez, *Thermo-economic analysis of solar thermal power cycles assisted MED-VC (multi effect distillation-vapor compression) desalination processes.* Energy, 2011. **36**(5): p. 2753-2764.
33. Bartolomé Ortega-Delgado, Lourdes García-Rodríguez, and Diego-César Alarcón-Padilla, *Thermoeconomic comparison of integrating seawater desalination processes in a concentrating solar power plant of 5 MWe.* Desalination, 2016. **392**: p. 102-117.
34. Gemma Raluy, Luis Serra, and Javier Uche, *Life cycle assessment of MSF, MED and RO desalination technologies.* Energy, 2006. **31**(13): p. 2361-2372.
35. R. Senthil Kumar, Kumaraswamy Sivasailam, and A. Mani, *Experimental investigations on a two-phase jet pump used in desalination systems.* Vol. 204. 2007. 437-447.
36. Dmitriy Likhachev and Feng-Chen Li, *Large-scale water desalination methods: A review and new perspectives.* Vol. 51. 2013. 2836-2849.
37. Mohamed Sharaf Eldean, Ahmed Nafey, and Lourdes García-Rodríguez, *Exergy and thermo-economic analyses of a combined solar organic cycle with multi effect distillation (MED) desalination process.* Vol. 272. 2011. 135-147.

38.   A. Ophir and J. Weinberg, *Multi-Effect Distillation – A Solution to Water Problem in the middle east*, ed. McGraw-Hill. 1997.

39.   H. M. Ettouney, H. T. El-Dessouky, and Imad Alatiqi, *Understand thermal desalination*. Vol. 95. 1999. 43-54.

40.   A. S. Hanafi, G. M. Mostafa, A. Waheed, and A. Fathy, *1-D Mathematical Modeling and CFD Investigation on Supersonic Steam Ejector in MED-TVC*. Energy Procedia, 2015. **75**: p. 3239-3252.

41.   Irfan Wazeer and Ibrahim Al-Mutaz, *Current status and future directions of MED-TVC desalination technology*. Vol. 55. 2014.

42.   Nuri Eshoul, Abdulrahman Almutairi, Rasaq Lamidi, Hamad Alhajeri, and Abdulrahman Alenezi, *Energetic, Exergetic, and Economic Analysis of MED-TVC Water Desalination Plant with and without Preheating*. Vol. 10. 2018. 305.

43.   O. A. Hamed, A. M. Zamamiri, S. Aly, and N. Lior, *Thermal performance and exergy analysis of a thermal vapor compression desalination system*. Energy Conversion and Management, 1996. **37**(4): p. 379-387.

44.   F. N. Alasfour, M. A. Darwish, and A. O. Bin Amer, *Thermal analysis of ME—TVC+MEE desalination systems*. Desalination, 2005. **174**(1): p. 39-61.

45.   Najem M. Al-Najem, M. A. Darwish, and F. A. Youssef, *Thermovapor compression desalters: energy and availability — Analysis of single- and multi-effect systems*. Desalination, 1997. **110**(3): p. 223-238.

46.   Giorgio Besagni, Riccardo Mereu, and Fabio Inzoli, *Ejector refrigeration: A comprehensive review*. Renewable and Sustainable Energy Reviews, 2016. **53**: p. 373-407.

47.   Refrigerating and Air-Conditioning Engineers American Society of Heating, *ASHRAE handbook*. 1983.

48.   S. K. Chou, P. R. Yang, and C. Yap, *Maximum mass flow ratio due to secondary flow choking in an ejector refrigeration system*. International Journal of Refrigeration, 2001. **24**(6): p. 486-499.

49.   Bourhan M. Tashtoush, Moh'd A. Al-Nimr, and Mohammad A. Khasawneh, *A comprehensive review of ejector design, performance, and applications*. Applied Energy, 2019. **240**: p. 138-172.

50.   MyoungKuk Ji, Tony Utomo, JuSik Woo, YongHun Lee, HyoMin Jeong, and HanShik Chung, *CFD investigation on the flow structure inside thermo vapor compressor*. Energy, 2010. **35**(6): p. 2694-2702.

51.   Szabolcs Varga, Armando C. Oliveira, and Bogdan Diaconu, *Influence of geometrical factors on steam ejector performance – A numerical assessment*. International Journal of Refrigeration, 2009. **32**(7): p. 1694-1701.

52.   R.B. Power, *Steam Jet Ejectors for the Process Industries*. 1994: McGraw-Hill.

53.   Yu Han, Xiaodong Wang, Hao Sun, Guangli Zhang, Lixin Guo, and Jiyuan Tu, *CFD simulation on the boundary layer separation in the steam ejector and its influence on the pumping performance*. Energy, 2019. **167**: p. 469-483.

54.   Cagri Metin, Okan Gök, Ayşe Uğurcan Atmaca, and Aytunç Erek, *Numerical investigation of the flow structures inside mixing section of the ejector*. Energy, 2019. **166**: p. 1216-1228.

55.   Dimitri Papamoschou and Anatol Roshko, *The compressible turbulent shear layer: an experimental study*. Journal of Fluid Mechanics, 1988. **197**: p. 453-477.

56.   Ali Hakkaki-Fard, Zine Aidoun, and Mohamed Ouzzane, *A computational methodology for ejector design and performance maximisation*. Energy Conversion and Management, 2015. **105**: p. 1291-1302.

57.   Y. Bartosiewicz, Zine Aidoun, P. Desevaux, and Yves Mercadier, *Numerical and experimental investigations on supersonic ejectors*. International Journal of Heat and Fluid Flow, 2005. **26**(1): p. 56-70.

58.   M. Antar, Killian McGovern, Ronan, Bulusu, Kartik, H. Lienhard, John, *One Dimensional Model Of An Optimum Ejector And Parametric Study Of Ejector Efficiency*. 2012.

59. CHAMPOUSSIN J C NAHDI E, HOSTACHE G, CHERON J. , *Optimal geometric parameters of a cooling ejector-compressor*. Int J Refrig (International Journal of Refrigeration) 1993.

60. Zuozhou Chen, Xu Jin, Akihiko Shimizu, Eiji Hihara, and Chaobin Dang, *Effects of the nozzle configuration on solar-powered variable geometry ejectors*. Solar Energy, 2017. **150**: p. 275-286.

61. T. Sriveerakul, S. Aphornratana, and K. Chunnanond, *Performance prediction of steam ejector using computational fluid dynamics: Part 2. Flow structure of a steam ejector influenced by operating pressures and geometries*. International Journal of Thermal Sciences, 2007. **46**(8): p. 823-833.

62. Hyomin Jeong, Tony Utomo, Myoungkuk Ji, Yonghun Lee, Gyeonghwan Lee, and Hanshik Chung, *CFD analysis of flow phenomena inside thermo vapor compressor influenced by operating conditions and converging duct angles*. Journal of Mechanical Science and Technology, 2009. **23**(9): p. 2366-2375.

63. Natthawut Ruangtrakoon, Tongchana Thongtip, Satha Aphornratana, and Thanarath Sriveerakul, *CFD simulation on the effect of primary nozzle geometries for a steam ejector in refrigeration cycle*. International Journal of Thermal Sciences, 2013. **63**: p. 133-145.

64. Yinhai Zhu, Wenjian Cai, Changyun Wen, and Yanzhong Li, *Numerical investigation of geometry parameters for design of high performance ejectors*. Applied Thermal Engineering, 2009. **29**(5): p. 898-905.

65. Chen Lin, Wenjian Cai, Yanzhong Li, Jia Yan, Yu Hu, and Karunagaran Giridharan, *Numerical investigation of geometry parameters for pressure recovery of an adjustable ejector in multi-evaporator refrigeration system*. Applied Thermal Engineering, 2013. **61**(2): p. 649-656.

66. Tony Utomo, Myongkuk Ji, Pilhwan Kim, Hyomin Jeong, and Hanshik Chung, *CFD Analysis on the Influence of Converging Duct Angle on the Steam Ejector Performance*. 2008.

67. WeiXiong Chen, DaoTong Chong, JunJie Yan, and JiPing Liu, *Numerical optimization on the geometrical factors of natural gas ejectors*. International Journal of Thermal Sciences, 2011. **50**(8): p. 1554-1561.

68. A. S. Ramesh and S. Joseph Sekhar, *Experimental and numerical investigations on the effect of suction chamber angle and nozzle exit position of a steam-jet ejector*. Energy, 2018. **164**: p. 1097-1113.

69. Szabolcs Varga, Armando C. Oliveira, Xiaoli Ma, Siddig A. Omer, Wei Zhang, and Saffa B. Riffat, *Experimental and numerical analysis of a variable area ratio steam ejector*. International Journal of Refrigeration, 2011. **34**(7): p. 1668-1675.

70. Kanjanapon Chunnanond and Satha Aphornratana, *An experimental investigation of a steam ejector refrigerator: the analysis of the pressure profile along the ejector*. Applied Thermal Engineering, 2004. **24**(2): p. 311-322.

71. Jiapeng Liu, Lei Wang, Lei Jia, and Xinli Wang, *The influence of the area ratio on ejector efficiencies in the MED-TVC desalination system*. Desalination, 2017. **413**: p. 168-175.

72. Yan Jia and Cai Wenjian, *Area ratio effects to the performance of air-cooled ejector refrigeration cycle with R134a refrigerant*. Energy Conversion and Management, 2012. **53**(1): p. 240-246.

73. DaoTong Chong, JunJie Yan, GeSheng Wu, and JiPing Liu, *Structural optimization and experimental investigation of supersonic ejectors for boosting low pressure natural gas*. Applied Thermal Engineering, 2009. **29**(14): p. 2799-2807.

74. Hongqiang Wu, Zhongliang Liu, Bing Han, and Yanxia Li, *Numerical investigation of the influences of mixing chamber geometries on steam ejector performance*. Desalination, 2014. **353**: p. 15-20.

75. Szabolcs Varga, Armando C. Oliveira, and Bogdan Diaconu, *Numerical assessment of steam ejector efficiencies using CFD*. International Journal of Refrigeration, 2009. **32**(6): p. 1203-1211.

76. Giorgio Besagni, *Ejectors on the cutting edge: The past, the present and the perspective*. Energy, 2019. **170**: p. 998-1003.

77. Paulo R. Pereira, Szabolcs Varga, João Soares, Armando C. Oliveira, António M. Lopes, Fernando G. de Almeida, and João F. Carneiro, *Experimental results with a variable geometry ejector using R600a as working fluid.* International Journal of Refrigeration, 2014. **46**: p. 77-85.

78. M. Dennis and K. Garzoli, *Use of variable geometry ejector with cold store to achieve high solar fraction for solar cooling.* International Journal of Refrigeration, 2011. **34**(7): p. 1626-1632.

79. Lei Wang, Jiapeng Liu, Tao Zou, Jingwei Du, and Fengze Jia, *Auto-tuning ejector for refrigeration system.* Energy, 2018. **161**: p. 536-543.

80. Fang Liu, *Review on Ejector Efficiencies in Various Ejector Systems.* 2014: Shanghai University of Electric Power, Shanghai, China.

81. A. Kayode Coker, *8 - EJECTORS AND MECHANICAL VACUUM SYSTEMS*, in *Ludwig's Applied Process Design for Chemical and Petrochemical Plants (Fourth Edition)*, A.K. Coker, Editor. 2007, Gulf Professional Publishing: Burlington. p. 525-573.

82. B. J. Huang, J. M. Chang, C. P. Wang, and V. A. Petrenko, *A 1-D analysis of ejector performance.* International Journal of Refrigeration, 1999. **22**(5): p. 354-364.

83. Da-Wen Sun and Ian Eames, *Recent developments in the design theories and applications of ejectors.* Vol. 68. 1995. 65-79.

84. Szabolcs Varga, Pedro S. Lebre, and Armando Oliveira, *Readdressing working fluid selection with a view to designing a variable geometry ejector*. Vol. 10. 2013.

85. Chaqing Liao, *GAS EJECTOR MODELING FOR DESIGN AND ANALYSIS*, in *Nuclear Engineering*. 2008, Texas A&M University.

86. F. Habashi, *Computational Fluid Dynamics Techniques.* 1995: Taylor & Francis.

87. S. B. Riffat and P. Everitt, *Experimental and CFD modelling of an ejector system for vehicle air conditioning.* Vol. 72. 1999. 41-47.

88. CFD Online, *Meshing.* 2012.

89. C.A.J. Fletcher, *Computational Techniques for Fluid Dynamics 1: Fundamental and General Techniques.* 2013: Springer Berlin Heidelberg.

90. Jiyuan Tu, Guan-Heng Yeoh, and Chaoqun Liu, *Chapter 5 - CFD Techniques: The Basics*, in *Computational Fluid Dynamics (Third Edition)*, J. Tu, G.-H. Yeoh, and C. Liu, Editors. 2018, Butterworth-Heinemann. p. 155-210.

91. Sanderson Gonzaga de Oliveira and Alexandre Abreu, *The use of the reverse Cuthill-McKee method with an alternative pseudo-peripheral vertice finder for profile optimization.* 2018.

92. Júnior Assis Barreto Bernardes and Sanderson L. Gonzaga de Oliveira, *A Systematic Review of Heuristics for Profile Reduction of Symmetric Matrices.* Procedia Computer Science, 2015. **51**: p. 221-230.

93. Marja Rapo. *Reordering nodes with the Reverse Cuthill-McKee algorithm.* 2017.

94. *ANSYS FLUENT Theory Guide.* 2011.

95. Timothy J. Barth and Dennis C. Jespersen, *The Design and Application of Upwind Schemes on Unstructured Meshes.* Vol. 0366. 1989.

96. B.P. Leonard, *ULTRA-SHARP Nonoscillatory Convection Schemes for High-speed Steady Multidimensional Flow.* 1990.

97. *FLUENT User's Guide, chapter 10 : Modeling Turbulence.* 2001.

98. Haidong Wang, Hui Wang, Feng Gao, Pengzhi Zhou, and Zhiqiang Zhai, *Literature review on pressure–velocity decoupling algorithms applied to built-environment CFD simulation.* Building and Environment, 2018. **143**: p. 671-678.

99. Robert Nichols, *Turbulence Models and Their Application to Complex Flows.* 2010.

100. Tuncer Cebeci, *1 - Introduction*, in *Analysis of Turbulent Flows*, T. Cebeci, Editor. 2004, Elsevier: Oxford. p. 1-30.

101. A. M. El-Belasy, M. B. Saad, and Y. I. Hafez, *2-D Hydrodynamic Model for Predicting Eddy Fields*, in *Proceedings from the International Conference on Advances in Engineering and Technology*, J.A. Mwakali and G. Taban-Wani, Editors. 2006, Elsevier Science Ltd: Oxford. p. 504-513.

102. Michael P. Païdoussis, *Chapter 2 - Cylinders in Axial Flow I*, in *Fluid-Structure Interactions (Second Edition)*, M.P. Païdoussis, Editor. 2016, Academic Press: Oxford. p. 143-302.

103. Ideen Sadrehaghighi, *Turbulence Modeling - A Review*. 2019.
104. D.C. Wilcox, *Turbulence Modeling for CFD*. 1994: DCW Industries, Incorporated.
105. Sandeep Bomminayuni, Thorsten Stoesser, and Nils Reidar Boe Olsen, *Evaluation of Low Reynolds Number Turbulence Models for an Open-Channel Flow over a Rough Bed Using LES Data*. Vol. 139. 2013. 664-668.
106. CFD Online. *Favre averaging*. 2013.
107. João Soares, *Efeito da dinâmica da ejecção de vórtice sobre a eficiência de desinfecção por ultravioleta em ETAR* in *Faculdade de Engenharia da universidade do Porto*. 2011.
108. Osborne Reynolds, *On the Dynamical Theory of Incompressible Viscous Fluids and the Determination of the Criterion*. Philosophical Transactions of the Royal Society of London. A, 1895. **Volume 186, pp. 123-164**.
109. Inc. ANSYS, *Modeling Turbulent Flows - Introductory FLUENT Training*. 2006: University of Southampton.
110. Szabolcs Varga, João Soares, Rafael Lima, and Armando Oliveira, *On the selection of a turbulence model for the simulation of steam ejectors using CFD*. Vol. 12. 2017.
111. Jia Yan, Wenjian Cai, and Yanzhong Li, *Geometry parameters effect for air-cooled ejector cooling systems with R134a refrigerant*. Vol. 46. 2012. 155–163.
112. K. Pianthong, W. Seehanam, M. Behnia, T. Sriveerakul, and S. Aphornratana, *Investigation and improvement of ejector refrigeration system using computational fluid dynamics technique*. Energy Conversion and Management, 2007. **48**(9): p. 2556-2564.
113. V. Yakhot, S. A. Orszag, Siva Thangam, T. Gatski, and C. G. Speziale, *Development of Turbulence Models for Shear Flows by a Double Expansion technique*. Vol. 4. 1992.
114. Sang Dug Kim, Chang Oh Kwon, and Dong Joo Song, *Comparison of turbulence models in shock-wave/boundary-layer interaction*. KSME International Journal, 2004. **18**(1): p. 153-166.
115. Tsan-Hsing Shih, William W. Liou, Aamir Shabbir, Zhigang Yang, and Jiang Zhu, *A new k-ϵ eddy viscosity model for high reynolds number turbulent flows*. Computers & Fluids, 1995. **24**(3): p. 227-238.
116. W. C. Reynolds, *Fundamentals of Turbulence for Turbulence Modeling and Simulation*. Report No. 755, Lecture Notes for Von Karman Institute, 1987.
117. Cornell University, *FLUENT Learning Modules*. 2018.
118. Inc. ANSYS, *ANSYS ICEM CFD User Manual*. 2012.
119. P.J. and George Frey, P.L., *Mesh generation: application to finite elements*. 2008.
120. Piotr Cyklis and Przemysław Młynarczyk, *The Influence of the Spatial Discretization Methods on the Nozzle Impulse Flow Simulation Results*. Procedia Engineering, 2016. **157**: p. 396-403.
121. André Francisco de Miranda Felício, *Modelação e dimensionamento de um sistema de dessalinização solar de pequena escala*. 2018, Faculdade de Engenharia da Universidade do Porto.
122. H. Schlichting, *Boundary-layer theory*. 1979: McGraw-Hill.
123. Theodore von Karman, *Turbulence and Skin Friction*. J. of the Aeronautical Sciences, 1934.
124. Nguyen Van Vu and Jan Kracik, *CFD simulation of ejector: is it worth to use real gas models?* EPJ Web Conf., 2018. **180**: p. 02075.
125. Kanjanapon Chunnanond and Satha Aphornratana, *Ejectors: Applications in refrigeration technology*. Vol. 8. 2004. 129-155.